DEVELOPMENT OF AN ACTIVE/ADAPTIVE LASER SCANNING MICROSCOPE

by

Christian Chunzi Archer-Zhang

A dissertation submitted in partial fulfillment
of the requirements for the degree

of

Doctor of Philosophy

in

Electrical Engineering

MONTANA STATE UNIVERSITY
Bozeman, Montana

November 2018

DEDICATION

To my adviser for his help, patience and guidance in life.

To my father who made me fall in love with medical science and technology.

To my mother who encouraged, motivated and supported me when I needed it most.

To my grandpa who gave me my sense of identity.

To my long-term friend Anya for her unconditional love.

To the beautiful people of Montana for their kindness, friendship and brotherly love.

ACKNOWLEDGEMENTS

I would like to thank my adviser, Dr. David L Dickensheets, for mentoring and supporting me in my Ph.D study and related research and for his patience, motivation, and immense knowledge. I would like to thank Dr. Wataru Nakagawa, Dr. Joseph Shaw and Dr. Charles Kankelborg for their teaching, insightful comments and encouragement.

I would like to express my gratitude to Dr. Kevin Repasky, Dr. Steve Shaw, and Dr. James Becker who helped me build a solid foundation that allows me to conduct the research for my Ph.D study.

I thank Dr. Robert Maher who brought me into the ECE program and for all the help he provided me along the way.

Also, I thank my friends here at Montana State University who provided me a friendly and productive environment for my study.

Last but not least, I would like to thank my colleagues, Ryan Downey, Warren Foster, Chris Arrasmith, Mohammed Moghimi, Tianbo Liu, Ethan Keeler and Martin Tauc for all their help and input in this research project.

TABLE OF CONTENTS

1. INTRODUCTION 1

Motivation.....1

Overview of This Project.....4

2. CONCEPTS AND THEORY 7

Two-photon Excitation Fluorescence Microscopy 7

Adaptive Optics in Laser Scanning Microscopy 14

Focus Control in Laser Scanning Microscopy.....19

System Implementation of Adaptive Optics for Microscopy 23

3. SELECTION OF ADAPTIVE OPTICAL COMPONENTS.....25

Mathematical Modeling for Tweeter DM.....25

Simulations with Zemax 31

4. SHAPE TRAINING ON BMC DM AND REVIBRO DM.....41

Defocus, Primary Spherical and Secondary Spherical

Training on Revibro DM 43

Off-axis Aberration Trainings on BMC DM 47

Combination of Multiple Zernike Shapes of Desired Amplitude.....50

5. DYNAMIC TESTING OF MEMS DM 53

Sinusoidal Steady State Response 54

Zernike Modal Step Response 58

6. ACTIVE/ADAPTIVE MICROSCOPE CONSTRUCTION 67

TABLE OF CONTENTS CONTINUED

Schematic of the Active/Adaptive Laser Scanning Microscope.....67
Solidworks Modeling.....68
7. SCANNERS AND MEMS DM CONTROL AND
IMAGING SOFTWARE DEVELOPMENT.....71
Software/Hardware Interface.....71
Synchronization.....74
8. ACTIVE SCANNING WITH DYNAMIC ABERRATION CORRECTION..80
Sensorless Aberration Measurement and Correction.....80
Image-based Wavefront Sensorless Adaptive Optics
Modal Optimization Algorithm Imaging with.....83
Imaging with Biological Samples.....106
9. DISCUSSION AND CONCLUSION.....111
Summary of this Research.....111
Limitations Encountered.....113
Single Point Calibration.....117
Suggestions for Future Work.....120
REFERENCES.....123
APPENDICES.....130
APPENDIX A: The Detailed Design Notes on the Optical System.....131
APPENDIX B: The Constructed Active/Adaptive
Microscope in Detail.....145

LIST OF TABLES

Table Page

1. Key parameters for comparing axial resolution between confocal microscopy and Two-photon excitation fluorescence microscopy using an Alexa Fluor 488 fluorochrome 11

2. The dominant aberrations over a 500 μm field of view and full 80μm focus range, from our Zemax model. The numbering of the Zernike terms follows the ANSI Standard $Z_{n,m}$ indexing scheme for radial order n and azimuthal frequency m 40

3. The binary count for defocus and spherical aberration characterization 45

4. Summary of the rise time for the BMC Multi-DM 61

5. The time needed for the BMC MEMS DM to settle below 36nm of RMS error to achieve diffraction limited imaging 62

6. Summary of dynamic performance for defocus on Revibro MEMS DM 65

7. Summary on dynamic performance for primary spherical aberration on Revibro MEMS DM 66

8. The Zernike coefficients for the correction wavefront map 93

9. The measured Zernike spectrum for the target shape produced under different humidity using single point calibration 120

10. BMC DM to Revibro DM 134

11. Lens data for imaging Revibro DM onto Y galvo scanner 137

12. Lens data for imaging Y galvo onto X galvo 140

13. Lens data for the combination of scan lens and Nikon tube lens 143

LIST OF FIGURES

Figure Page

1. Jablonski diagram of one-photon (left) and two-photon excitation (right) in traditional confocal fluorescence laser scanning microscopy and the Two-photon excitation fluorescence microscopy....7

2. Depth discrimination achieved through pinhole rejection of the out-of-focus light for confocal microscopy....8

3. TFPM....10

4. Comparison in axial resolution between an ideal high NA confocal microscopy and Two-photon excitation fluorescence microscopy....12

5. Imaging an object through (a)homogeneous medium and (b) turbid medium....15

6. The perfect 2D point spread function (PSF) at the focus (a) and when aberrations are present: (b) spherical aberration, (c) coma and (d) astigmatism....17

7. Cross section view of a common type of MEMS DMs....18

8. A cross section view of a FCDM....21

9. Mechanical structure of electromagnetic MEMS DMs....22

10. The three types of commercially available MEMS DMs....25

11. The mathematic modeling for the MEMS DMs....27

12. The achievable Strehl after aberration correction on astigmatism and primary spherical aberration (Z4,0) for different amplitudes....29

13. The Zemax simulation of the AO module with commercially available optics elements....33

14. Aberrated wavefront shapes at different focal depth for the proposed woofer-tweeter from simulations of the relay in Zemax....36

LIST OF FIGURES CONTINUED

Figure Page

15. The isometric view of the representative 25x1.0 NA water immersion objective lens 37

16. Aberrated wavefront shapes at different focal depth for the proposed woofer-tweeter from simulations of the objective lens in Zemax. All units for the scale bar are in waves at design wavelength of 1µm 38

17. Aberrated wavefront shapes at different focal depth for the proposed woofer-tweeter from simulations of the entire optical system in Zemax 39

18. Schematic diagram for mirror shape training with WFS 43

19. The BMC DM element chart 47

20. Standard Zernike shapes trained on the BMC Multi-DM and Revibro DM 50

21. The system setup for dynamic testing using stroboscopic phase-shift interferometry 54

22. Stroboscopic imaging for frequency response 56

23. Frequency response for different standard Zernike shapes on the BMC Multi-DM 57

24. Stroboscopic imaging for a step response 58

25. Step response for different tested Zernike modes at a step from 0 to 400nm in amplitude on the BMC Multi-DM 60

26. Step response for different amplitudes of astigmatism on BMC Multi-DM 63

27. Step response of active focus control with Revibro MEMS DM 64

LIST OF FIGURES CONTINUED

Figure Page

28. The step response for different amplitudes in spherical aberration correction on the Revibro MEMS DM 66

29. The schematic of the Active/Adaptive Microscopy 67

30. The SolidWorks model of the MEMS DMs, galvo scanner heads, relays with proper alignment and spacing label for the Active/Adaptive 2-Photon Microscope 69

31. The constructed Active/Adaptive 2-Photon Microscope 70

32. The architecture of the control interface for the active/adaptive laser scanning microscope 72

33. The 25 sub-regions of each single frame of an image 75

34. Triggering signals for the BMC DM 77

35. Driving signals for the 4 channel Revibro DM 79

36. Flowchart for the image based sensorless optimization 86

37. A demonstration of dynamic off-axis aberration training with BMC DM 87

38. The 25 sub-regions of a single frame image 90

39. The sub-wavelength resolution target (upper) before aberration correction and (lower) after spherical and off-axis aberration being corrected near the edge 91

40. The contrast of the submicron features in the region of interest after each iteration of sensorless image optimization 92

41. The aberration free PSF of a 500nm 95

42. The improvement in PSF of the 500nm disk near (left) the center and (right) the edge 96

LIST OF FIGURES CONTINUED

Figure Page

43. Images of a tilted diffraction grating with active focusing turned on/off 97

44.The wavefront map for focus control and primary spherical aberration correction for imaging the tilted diffraction grating 98

45. Active focusing on a tilted negative resolution target 101

46. The fitted 100 by 500 points of defocus to tracking the tilted target 102

47. The dynamic aberration correction throughout the entire field of view 103

48. Improvement in PSFs for the 1μm.....104

49. The wavefront maps for aberration.....104

50. Dynamic focus control and aberration correction on a rabbit testis in vitro.....107

51. Active focus adjustment and dynamic aberration correction on an image of Rabbit spinal Cord 109

52. The system setup for direct wavefront measurement under the influence of different humidity 114

53. Voltages applied vs Defocus (Z2,0) produced on the Revibro DM under the influence of different humidity.....115

54. Setup for the image base single point calibration 119

55. Zemax model for the optical path from BMC DM to Revibro DM.....132

56. The Spot diagram for the relay 135

57. Zemax model for the 4f relay between Revibro DM and Y galvo scanner ...136

58. Spot diagram for the 4f relay between Revibro DM to Y galvo.....137

LIST OF FIGURES CONTINUED

Figure Page

59. Zemax model for the 4f relay that image the Y galvo scanner onto the X galvo scanner 139

60. The spot diagram for the 4f relay between x and y galvo scanners at different scan angles.....140

61. The relay consists of a scan lens and the tube lens in the Nikon microscope stand for imaging x galvo scanner onto the back focal plane of the objective lens 142

62. Spot diagram for the Scan lens and tube lens at different scan angles 142

63. Strehl of the relay at different scan angle in x direction 144

64. The laser source illuminates the BMC DM and imaged onto the Revibro DM through a single lens relay 146

65. Both Revibro DM and BMC DM are imaged onto the WFS through a 4f relay.....147

66. The Y gavlo is imaged onto the back focal plane of the objective through a relay consists of the scan lens (SL) and a Nikon tube lens inside the Nikon TE 300 microscope stand 148

67. The sample stage mounted on a motorized x-y-z translation stage 149

ABSTRACT

Laser scanning techniques such as confocal microscopy and two-photon excitation fluorescence microscopy (TPM) are powerful tools for imaging biological samples with high resolution, offering three-dimensional (3D) visualization of the behavior of cells in their natural environment. Traditionally, the 3D images are acquired from 2D image stacks with focusing depth controlled through mechanical movement of the specimen relative to the objective lens. The slow mechanical movement (~<20Hz) does not allow the spot of light to be scanned axially sufficiently fast to monitor cell:cell and cell:environment interactions in real time over hundreds of microns in all three dimensions. A fast focus control mirror supports agile scan patterns such as vertical or oblique planes or even arbitrary surfaces, minimizing the time and photo damage required to monitor features of interest within the 3D volume. Because aberrations cause image quality to decrease as the focal point of the beam penetrates deeper into the sample, adaptive optics can enhance resolution and contrast at depth for confocal microscopy and TPM. Combining a fast focus control mirror with a fast aberration correcting mirror leads to a flexible platform called the active/adaptive laser scanning microscope, capable of aberration-corrected beam scanning throughout a 3D volume of tissue. This opens up the possibility of fully corrected, variable-depth imaging along oblique sections or more complex user-defined surfaces within a single image frame.

INTRODUCTION

Motivation

We have entered an exciting new era in biomedical imaging. The discovery of green fluorescent protein and the creation of many different genetically encoded biosensors and light regulated ion-channels, pumps and enzymes have revolutionized cell biology and opened a new frontier for non-invasive approaches to peer into the inner workings of sub-cellular structures and organelles. These groundbreaking techniques allow researchers to perform fantastic experiments such as imaging action-potential activity in functional neuronal circuits by loading brain slices with calcium indicators [1] [2]. Laser scanning microscopy such as confocal microscopy (CM), two-photon excitation fluorescence microscopy (TPM) and three-photon microscopy (3PM) are the current methods of choice for in vivo deep tissue imaging. TPM is a powerful tool for imaging biological samples with high resolution, offering direct visualization of the behavior of cells in their natural environment [3] [4]. TPM utilizes the non-linear laser excitation. As the Two photon excitation occurs proportional to the square of the local intensity of the beam, where the photon flux is highest, the total two-photon fluorescence falls off rapidly away from the focal plane. Therefore, the two-photon fluorescence emission that contributes to the acquired image only takes place at the focus of the illumination beam. TPM can maintain excellent photon efficiency even at imaging depths of over hundreds of microns.

The following introductory section is a verbatim excerpt from our previous publication in the Journal of Biomedical Optics [5].

However, the image quality decreases rapidly as the focal point of the TPM penetrates deeper into the sample. Although dependent on the type of tissue, TPM has not yet been able to acquire images with high resolution deeper than about 1 mm [4] [6]. The fundamental depth limit is due to several factors including attenuation of the excitation light through absorption and scattering in the tissue and, importantly, aberrations that degrade both resolution and contrast, obscuring features of interest. These aberrations can be due to the optical inhomogeneity of the biological sample when penetrating through hundreds of microns of tissue (sample-induced aberration) and may also arise from an imperfect optical system (systematic aberration). In TPM, degradation of the beam focus contributes directly to signal loss at depth due to the square-law dependence of the measured signal on the peak intensity of the focused beam.

Adaptive optics is known to enhance resolution and contrast at depth for confocal and TPM. Adaptive optical elements such as microelectromechanical systems (MEMS) deformable mirrors (DMs) can perturb the illuminating wavefront to pre-compensate for optical path length variations in the optical system as well as the sample [7] [8] [9] [10] [11] [12] [13]. For example, Booth et al. [7] incorporated a DM into a confocal microscope and showed good results with aberration correction in a mouse intestine specimen. Kong and Cui [14] have demonstrated that the iterative multiphoton adaptive compensation technique can greatly improve the signal strength, resolution, and contrast for in vivo neuron imaging in mouse cortex at a large depth (~660 μm). Others have

shown promising results with a liquid crystal modulator for wavefront error compensation in biological samples [13]. To date, these demonstrations have adopted a single wavefront correction for a particular depth. The correction is fixed for all points within the field of view, and may not optimally correct the aberrations throughout the field of view.

Although spherical aberrations introduced by refractive index mismatch of the objective and the medium have been well studied, the variation of specimen-induced aberrations is not typically known. These more complex natured aberrations arise from structure of the biological sample and spatially varies across the specimen. A traditional assumption for AO microscopy is that aberrations do not change over the field of view, but it is often proven invalid. The single/static aberration correction may improve the image quality in some area of the image, but others may be made worse [15].

In addition to managing aberrations, MEMS mirrors capable of large displacements can be used for dynamic focus control during imaging [16] [17] [18]. Compared to mechanical means of focusing that translate the objective lens or the sample, focusing by modifying the wavefront curvature using an MEMS deformable mirror introduces no vibrations and can be accomplished at much higher speeds. This opens up the possibility of imaging along oblique sections or more convoluted surfaces, and for multi-depth imaging within a single image frame. This innovative imaging method provides a new powerful tool to directly visualize organelles and networks with contoured planes at a cellular or even sub-cellular level without the need to capture a full 3D imaging stack.

A consequence of using a MEMS DM for focus control is an introduction of additional systematic aberration. The objective lens and the relay lenses in a scanning laser microscope are optimized only for a particular imaging depth in the sample. When used to image at other depths, both spherical aberration and uncorrected off-axis aberrations arise. Combining a focus control mirror with an aberration correcting mirror leads to a flexible platform capable of aberration-corrected beam scanning throughout a three-dimensional (3-D) volume of tissue. This is the system we are developing that we call an active/adaptive laser scanning microscope (end of JBO excerpt).

Overview of This Project

The contribution of this project is to address the pressing need for better imaging to realize the full potential of newly developed fluorescent biosensors. By building an active/adaptive laser scanning microscope, we are now capable of directly visualizing a contoured biological surface with high resolution throughout a 3D field of view.

This thesis is comprised of 9 chapters.

- The current chapter provides the background about current state of the art imaging techniques to image deep into biological samples in vivo and non-invasively. It addresses the motivation for this project to develop a novel imaging platform.
- Chapter 2 summarizes the concepts of common laser scanning microscopy, such as TPM and CM, and the application of fast focus control and adaptive optics in laser scanning microscopy.

- Chapter 3 reviews the current state of the art active and adaptive elements that are candidates for our active/adaptive laser scanning microscope. Mathematical modeling with Matlab and simulations with Zemax have been performed to evaluate the range of possible systematic aberrations and the ability of these active/adaptive elements to fully compensate the aberrations and restore the PSF. It leads to the decision to install two deformable mirrors (DM), a Boston Micromachines (BMC) Mulit-DM and a Revibro DM, and to use a modal compensation strategy based on Zernike modes to drive these active and adaptive elements.
- Chapter 4 describes the Zernike modal shape trainings on the BMC DM and the Revibro DM.
- Chapter 5 investigates the dynamic performance of the BMC multi-DM and Revibro DM. By building a stroboscopic interferometer, the step response and frequency response for each Zernike modal shape on the two DM elements are tested and reported in the context of performing real-time intra-field correction.
- Chapter 6 describes construction of the active/adaptive laser scanning microscope. The lens data including the spacing and orientation of each optical element is exported from Zemax. Based on the lens data, an exact 1:1 model of the entire optical system including all the lenses, mirrors, mounts, DMs and all other optical components are built with Solidworks. It guides the purchases and assembly of the active/adaptive laser scanning microscope.

- Chapter 7 details the software development for imaging acquisition and controlling the DMs and synchronization to the galvo scanners.
- Chapter 8 illustrates all the imaging results of resolution targets and biological samples from all the active contour surface tracking and systematic aberration corrections.
- Conclusions are drawn in Chapter 9.

CONCEPTS AND THEORY

The Active/Adaptive Laser Scanning Microscope is designed as a platform to accommodate both Two-photon Excitation Fluorescence Microscopy and Confocal Microscopy. The following is a review on these two imaging methods.

Two-photon Excitation Fluorescence Microscopy

Invented in 1990 by Denk et al [19], the two-photon fluorescence microscope (TPFM) is a revolutionary development in biological imaging. It is a new technique built on the basic laser scanning microscope but with significant improvement in penetration depth, image resolution, reduced phototoxicity and ability to initiate localized photochemistry.

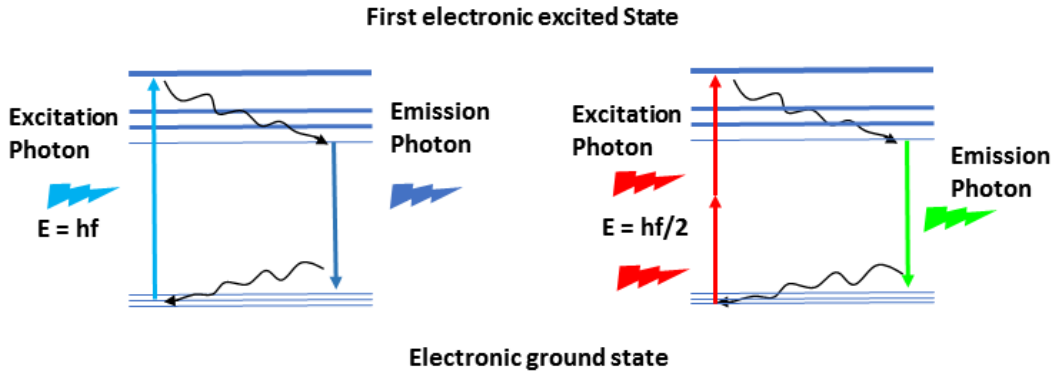

Figure 1. Jablonski diagram of one-photon (left) and two-photon excitation (right) in traditional confocal fluorescence laser scanning microscopy and the Two-photon excitation fluorescence microscopy.

The traditional fluorescence confocal laser scanning microscope (CLSM), which is a one-photon fluorescence process, involves exciting a fluorophore from the electronic ground state to an excited state by a single photon and uses a pinhole in front of the photodetector to achieve depth discrimination. As shown in Figure 2, the pinhole is in conjugate to the focal point of the objective lens so that the out-of-focus light is rejected by the pinhole.

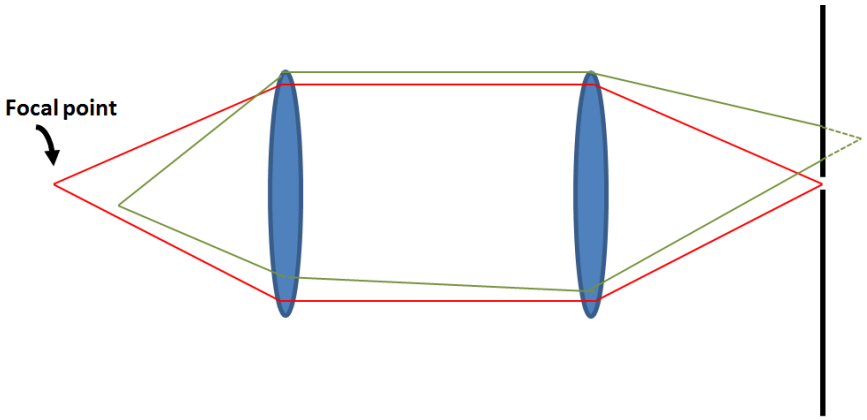

Figure 2. Depth discrimination achieved through pinhole rejection of the out-of-focus light for confocal microscopy. The rejection of out-of-focus light (green) is achieved through a pin hole in front of the photo-detector in CLSM. Meanwhile the light reflected from the focal point that reaches the screen will pass the pinhole and be detected (red).

In such configuration, the steepness of the falloff of the axial intensity largely determines the depth discrimination of a confocal microscope. The falloff of the axial intensity can be found to be a sinc function. For a fluorescent point reflector, the axial resolution for a confocal microscopy can be expressed as the equation below [20].

$$I_c(z) = \left[\frac{\sin\left(\frac{u_i}{4}\right)}{\frac{u_i}{4}}\right]^2 \left[\frac{\sin\left(\frac{u_f}{4}\right)}{\frac{u_f}{4}}\right]^2$$

$$u_i = 2k_i n_i z(1 - \cos(\alpha))$$

$$u_f = 2k_f n_f z(1 - \cos(\alpha))$$

where k_i and k_f are the wavenumber for the incident beam and fluorescence, n_i and n_f are the refractive index for the incident beam and fluorescence, α is the half angular aperture of the objective and z is the axial distance from the focal point.

On the other hand, the two-photon molecular excitation is achieved through a high numerical aperture (NA) objective focusing a high power laser into a diffraction limit spot where the two photon excitation occurs. The phenomenon of the two-photon excitation arises from the simultaneous absorption of two photons with a wavelength about twice that of the emission photon. Current fluorophores usually are excited by two photons of near-infrared light to emit a photon at a wavelength in the green/blue region of the spectrum as shown in Figure 1.

The two-photon molecular excitation depends on the square of the incident intensity of the laser, and it is favored when 1) the incident photon flux has high intensity, 2) high NA objective lenses are used and 3) the fluorophore has large excitation cross-section. In general, the probability of excitation is governed by the equation below [21]:

$$\text{Equation 1. } n_a = \frac{P_0^2 \sigma}{\tau_p f_p^2} \left(\frac{\pi NA^2}{hc\,\lambda}\right)^2, NA = n \times sin(\alpha)$$

where n_a is the probability of excitation, σ is the excitation cross section, P_0 is the average power of the incident laser light, τ and f are the pulse width and repetition frequency of the laser source, h is the Planck's constant, c is the speed of light, λ is the

incident wavelength, n is the refractive index of the medium and α is the half angular aperture of the objective.

Consequently, it is crucial to use a high NA objective for TPFM for depth discrimination. As the laser beam is focused with a high NA objective, the photons are concentrated in a sub-micron spot among the fluorophores. Therefore, the spatial intensity at focus increases dramatically, making it the only location within the 3D volume where the photons are crowded enough to generate significant interactions between photons and fluorophore, which leads to two-photon molecular excitations. In practice, this narrow localization of photons is further enhanced by using short pulses (few tens of femtoseconds usually) from a mode locked laser so that the photons are not only concentrated spatially by the high NA objective but also confined temporally.

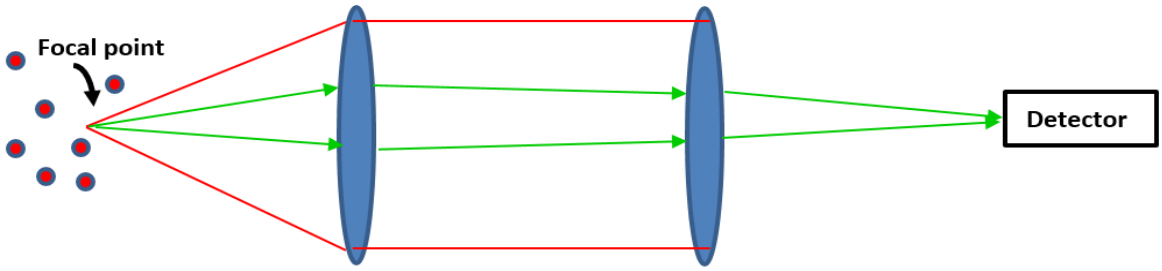

Figure 3. TPFM

The characteristic spatial beam profile for TPFM at the focus is described as below:

Equation 2. $I(u,v) = \left|2\int_0^1 J_0(v\rho)e^{-\frac{i}{2}u\rho^2}\rho d\rho\right|^2$

where $u = 4k(1 - \cos(\alpha))z \; and \; v = ksin(\alpha)r$ are the axial optical coordinate and radial optical coordinate normalized to wave number in medium $k = \frac{2\pi}{\lambda}$ [22].

The axial resolution of the TPFM can be expressed as below:

Equation 3. $I_{2p}(z) = \left[\frac{\sin\left(\frac{u_i}{4}\right)}{\frac{u_i}{4}}\right]^4$

where u_i is calculated using the wavenumber and refractive index of the incident beam.

To compare the axial resolution of confocal microscopy and two-photon excitation fluorescence microscopy side by side, a water immersion objective with high NA =0.9 is chosen. The following assumptions are made for the simulation. First, the imaging system is aberration free. Second, it is the ideal case that both pinhole size and the fluorescent point reflector are infinitesimally small. The values for the key parameters, refractive index for excitation wavelength (n_i), refractive index for fluorescent wavelength (n_f), are used as in Table 1.

Table 1. Key parameters for comparing axial resolution between confocal microscopy and Two-photon excitation fluorescence microscopy using an Alexa Fluor 488 fluorochrome [23]

	n_i	n_f	λ_i (μm)	λ_f(μm)
Confocal	1.33	1.33	491	515
TPFM	1.33	1.33	985	530

To compare confocal and TPFM side by side, a Fluorochrome Alexa Fluor 488 is chosen for the simulation. For confocal microscopy, the excitation wavelength is similar

to the emission wavelength. On the other hand, the excitation wavelength is nearly twice the emission wavelength for TPFM.

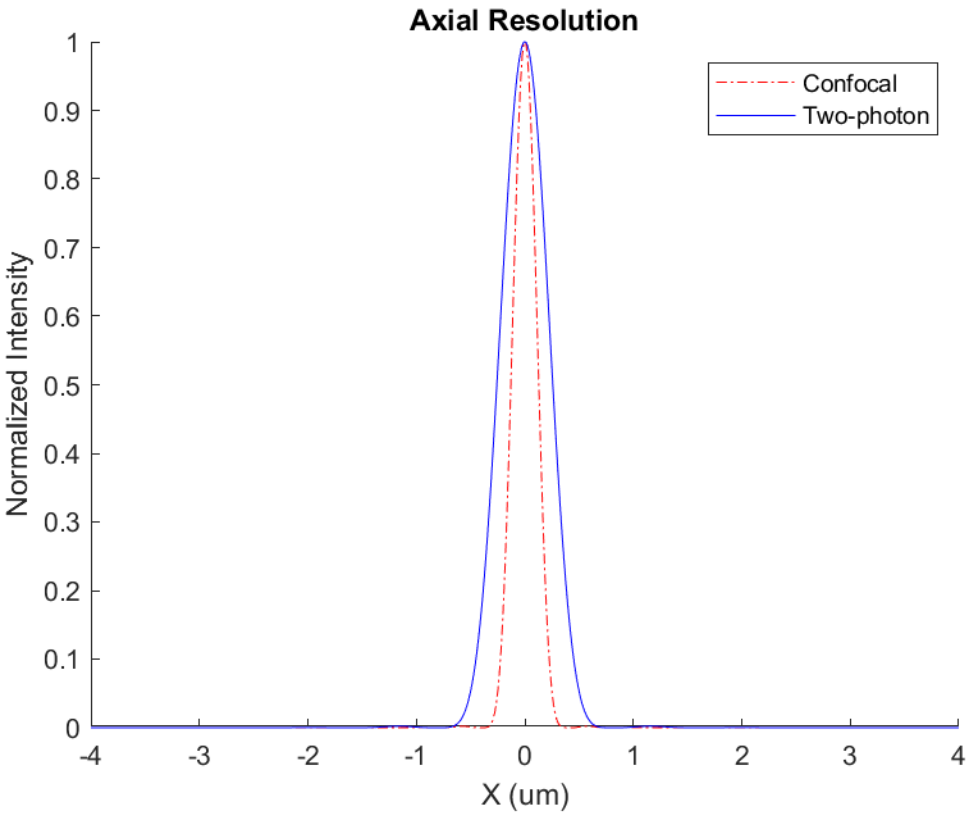

Figure 4. Comparison in axial resolution between an ideal high NA confocal microscopy and Two-photon excitation fluorescence microscopy

The narrow confinement of the photons of TPFM can have many advantages over the traditional CLSM. The most important advantage of TPFM is that the resolution of TPFM can achieve nearly the ideal image resolution of CLSM. As shown in Figure 4, although the longer excitation wavelength makes TPFM have a slightly wider FWHM in comparison to an ideal confocal microscopy with infinitesimal pinhole, the axial resolution of TPFM is very comparable to confocal microscopy.

Moreover, the imaging signal only originates from the focus, which does not require any pinhole for out-of-focus light rejection. This does not only simplify the system, but also provides more flexibility in detection geometry. Without the pinhole placed in front of the photo-detector, the TPFM can utilize the non-descanned signal and the photo-detector is placed right beneath the objective. Consequently, TPFM requires fewer optical elements and reduces the detection optical path length significantly. As a result, the photon collecting efficiency is highly increased and there is less multilayer reflections/interference with the fluorescent signal allowing much lower noise floor and signal-to-background ratio for small signal detection. Furthermore, since the photon excitation is confined to the focus, both photo-bleaching and photo-damage from above and below the focal point are minimized, which gives extended viability of the living cells and tissues being investigated.

Last but not least, the superior penetration depth makes the TPFM a much more powerful tool for deep tissue imaging. The penetration depth of confocal microscopy, which allows out-of-focus background fluorescence that produces photobleaching and phototoxicity throughout the specimen, is limited by absorption of excitation energy and scattering of both excitation and emission photons throughout the beam path. In comparison, the near infrared light (at twice the wavelength) used in TPFM is much more immune to both scattering and absorption by the specimen. Moreover, photon absorption only takes place at the focal plane. Consequently, 1) the minimized absorption in the out-of-focus specimen areas and 2) less photon scattering result in more excitation light penetrating deeper into the biological samples. The penetration depth of TPFM is

generally two or three times what can be achieved by CLSM. In general, TPFM can acquire images with sub-micron resolution down to a depth of few hundred microns.

The effective sensitivity of fluorescence microscopy makes TPFM excel at imaging thin (~1mm) specimens of living cells, particularly intact tissues such as embryos, brain slices, and even an entire small animal like the Zebra fish.

Nonetheless, recent studies have demonstrated that two-photon image resolution degrades in the presence of scattering and optical inhomogeneity found in biological samples [24] [25] [26] [6] [4]. The cause of image degradation is decomposed into 1) signal loss arising from attenuation of excitation photons and attenuation of fluorescence due to both scattering and absorption, and 2) degradation of the point spread function (PSF) as penetration depth increases due to sample induced aberration such as spherical aberration and off-axis aberrations.

Adaptive Optics in Laser Scanning Microscopy

When an image is taken for an object in a homogeneous medium, the incident light convolves with the object and forms an image as spatial variations light intensity on the detector. As shown in Figure 5(a), the photons from the light source is considered to be travelling in a straight line.

On the other hand, if the object is located in a scattering medium (such as human skin), the situation becomes much more complicated. First, the incident photons will experience multiple scattering and become diffused light that does not contain useful information for image formation. Second, ballistic photons, which are the photons that

still travel in a straight line and carry useful information, will be attenuated much faster by scattering.

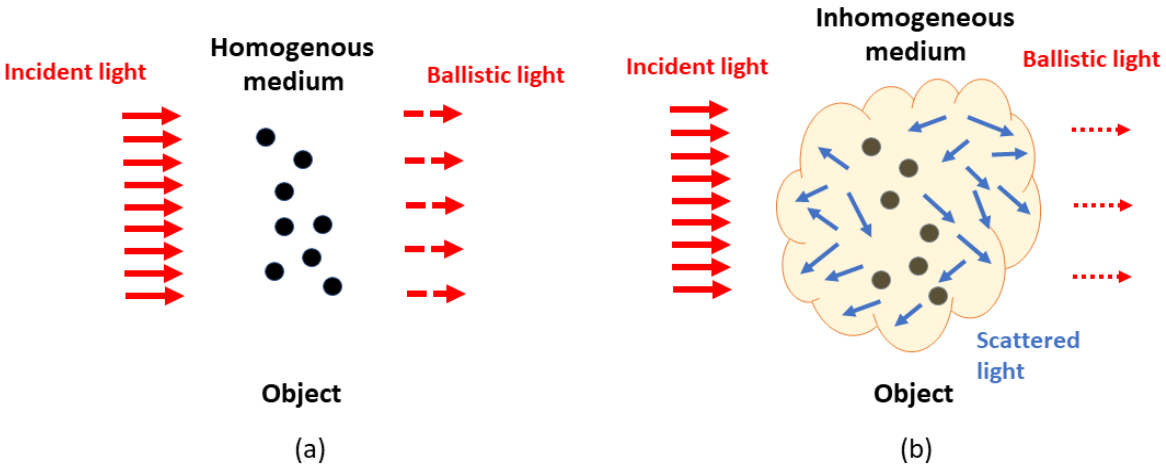

Figure 5. Imaging an object through (a)homogeneous medium and (b) turbid medium [27].

Aberrations (especially spherical aberration) increase with both NA and depth into the sample. This ultimately limits the useful penetration depth.

From Fourier optics, the objective lenses introduce a spherical phase function that converts a planar wavefront into spherical wavefront in the focal region. As the light passes through the biological samples, the ideal spherical wavefront is distorted by the planar refractive index mismatch and phase variation from the inhomogeneous structure of the biological samples. This distortion of the wavefront can be understood as the refractive index profile of the biological samples. Aberration leads to the degeneration of the focus in both lateral plane and axial plane in forms of reduction of focal intensity and distortion of the focal point. The reduced focal intensity lowers the image contrast and optical efficiency while the degeneration of focus corrupts both lateral and axial

resolution [28]. In many cases of biological imaging, high resolution at depth, an important goal of in vivo microscopy, is not achievable due to the heavily distorted wavefront induced from the inhomogeneity in the biological samples [29] [30] [31].

To compensate the aberrations in deep tissue imaging, a promising technique is to perform a pupil engineering. The wavefront (phase function of the pupil) coming into the specimen is modulated in such a way that this phase function will be cancelled out by the aberrations induced by large scale heterogeneities in the biological samples. The aberrations are usually categorized in different types, including coma, spherical aberrations, astigmatism, defocus, etc. The most common approach for the pupil engineering for wavefront correction is adaptive optics with Microelectromechanical systems deformable mirrors (MEMS DM), focus control deformable mirrors (FCDM) and spatial light modulators.

The simulation plots in Figure 6 demonstrate how the quality of the PSF can be largely affected by aberrations such as Figure 6(b) balanced primary spherical aberration, Figure 6(c) coma and Figure 6(d) astigmatism presence in the optical system as well as in biological samples. The wavelength for the simulation is 1μm and the amplitude for each aberration term is one wave.

The equation used for each aberrated pupil function is calculated as follows.

$$Aberration\ free\ phase\ function: W_0 = 0;$$

$$Phase\ function\ for\ balanced\ spherical\ aberration:$$

$$W_{Spherical} = \frac{\rho^4}{r^4} - \frac{\rho^2}{r^2};$$

$$Phase\ function\ for\ Coma: W_{Coma} = \frac{\rho^2}{r^3}x;$$

$$Phase\ function\ for\ Astigmatism: W_{Astigmatism} = \frac{x^2}{r^2};$$

$$pupil = circ(\frac{\rho}{r}) \times \exp(-1i \times k \times a \times W)$$

where$\rho = \sqrt{x^2 + y^2}$, r is the radius of a circular pupil, k is the wavenumber, a is the amplitude of the aberration in waves and W is the phase function.

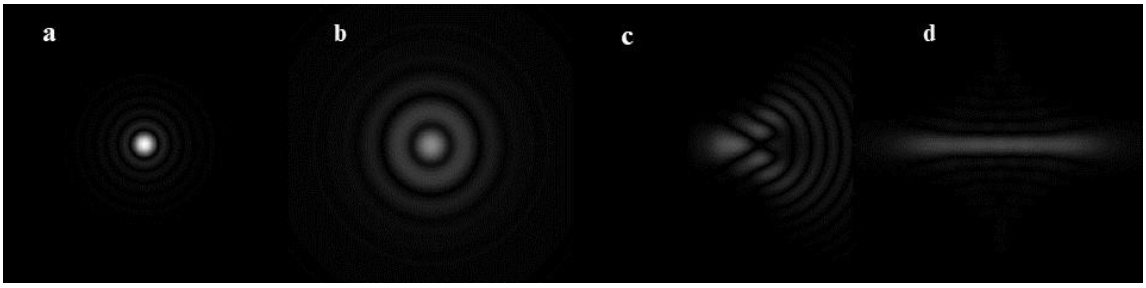

Figure 6. The perfect 2D point spread function (PSF) at the focus (a) and when aberrations are present: (b) spherical aberration, (c) coma and (d) astigmatism. Since the image quality is determined by the quality of the PSF, it is not hard to see how aberrations degrade the resolution of the image quickly before it becomes fully unreadable. The amplitude of all the aberrations for this plot are in one wave.

Liquid-crystal spatial light modulators (LC SLMs) are very versatile optical devices capable of producing wavefront shapes with high spatial resolution at a large amplitude. They also have the advantages of relatively low cost, high reliability and low power consumption. LC SLMs are built based on their optical and electrical anisotropy. Due to the electrical anisotropy, voltage applied on different areas of the LC leads to a variable tilt of the LC molecules. A combination of the tilt and optical anisotropy of the LC molecules causes variation of optical path length as light passes through the LC SLM.

As a result, a modified wavefront is formed. Each pixel pitch of LC SLM can be as small as a couple of microns, making it a very precise wavefront shaping device.

Nonetheless, the main drawbacks of LC SLMs are their slow response time and the fact they can only work with polarized light. These LC SLMs usually have a bandwidth of a few tens of hertz, making it unsuitable for aberration correction in real time imaging. Therefore, we look into the MEMS DMs seeking a much faster solution.

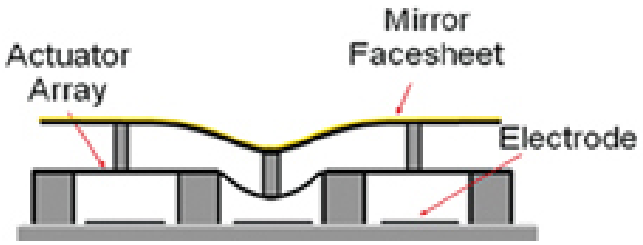

Figure 7. Cross section view of a common type of MEMS DMs [32].

As shown in Figure 7, the MEMS DMs are fabricated using silicon MEMS production techniques. The deformable mirror facesheet is connected by posts to an array of electrostatic actuators. When voltage is applied on the electrodes, electrostatic attractive force is generated to pull the central post towards the substrate, which will result in a changed shape of the mirror facesheet. The deflection of each individual actuator is proportional to the square of applied voltage on the corresponding electrode. The actuator count can be as many as 4092 (Boston Micromachines Corporation 4K-3.5). For its high-spatial-resolution, the MEMS DMs excelled in correcting high order aberration (astigmatism, coma and trefoil) both induced by the imaging sample and the

optical system. With a closed loop control, the residue wavefront error can be driven down to less than 10nm [5].

Nonetheless, the limitation of MEMS DM is that the range of deformation is much less comparing to FCDM. The maximum stroke for these MEMS DMs usually ranges from 1.5μm to 8μm. To provide focus control, a large magnitude of wavefront correction is required, and MEMS DMs can't deliver the desired wavefront with sufficient amplitude. The relative larger range of achievable spherical deformation of the FCDM is a good solution for defocus and low orders of spherical aberration correction. However, the only motion for this type of DM is radial - no azimuthal variation is possible. More complicated aberration is very difficult to be compensated through this type of FCDMs due to its limitation of deformation shape.

Focus Control in Laser Scanning Microscopy

Traditional focus control in microscopy is based on methods of using servo motors to physically translate the optics or the imaging sample under investigation. It presents problems such as mechanical complexity, undesired mechanical vibration, high power requirement and slow speed for focus adjustment.

To overcome these limitations, alternative approaches have been taken with devices such as an electrowetting liquid lens [33], pneumatic liquid lens [34] [35] [36], variable-focus liquid-filled optical lens [37] and MEMS DMs.

In the research done by Naumov et al, a large birefringence and low control voltage nematic liquid crystal lens was built that has a focal length range of 2mm [35].

As for the dynamic performance, the liquid crystal lens is capable of doing large defocus in the speed in the order of few hundreds of milliseconds. Shibuya et al has demonstrated a liquid lens can be driven with a high-speed voltage booster to the target wavefront sag of 2.5μm within 66ms [38]. As for electrowetting, which is based on changing the shape of a liquid lens in a conducting liquid through voltage applied between the substrate and the conducting liquid, the switching speed is typically 10ms [39]. These results are representative of what is possible with liquid crystal and liquid lens approaches.

Comparing to both the liquid crystal lens and either electrowetting or pneumatic liquid lenses, the FCDM stands out in its fast speed for making large range of focus control. A small mirror can provide up to hundreds of kilohertz for precise focus control including adjustable aspherical parameters [40]. A larger FCDM is capable of up to 15μm stroke (Δd**)** within 58 micro-seconds [5].

Focus control based on wavefront modification in an optical microscope is governed by the equation [41]

Equation 4. $$\Delta f = \frac{2 \times \Delta w \times n}{NA^2}$$

where Δf is the adjustment of the focal plane, Δw is the peak to valley parabolic sag of the wavefront (for a mirror, $\Delta w = 2\Delta d$), n is the refractive index of the sample under investigation (e.g. 1.33 for water) and NA is the numerical aperture of the objective lens. For example, a FCDM with 16 μm stroke used at NA=0.9 can provide axial focus adjustment over a range of 105 μm, which is a useful range for many high resolution microscopy applications. The combination of large effective adjustable wavefront sag

and high speed makes the FCDM highly attractive for automatic focus control in a laser scanning microscope.

The FCDM shown in Figure 8 has a metal coated silicon nitride or SU-8 membrane with several microns in thickness suspended over silicon substrate with an air gap. The electrodes are in a shape of concentric rings and located under the mirror facesheet. When a high voltage is applied on electrodes relative to the grounded membrane, it deforms spherically and modulates the wavefront of the incoming light. By changing the voltage, it is possible to control the deformation of the membrane electronically so that focus control can be achieved. In addition to focus control, low order spherical aberration induced by the objective and imaging sample can also be compensated.

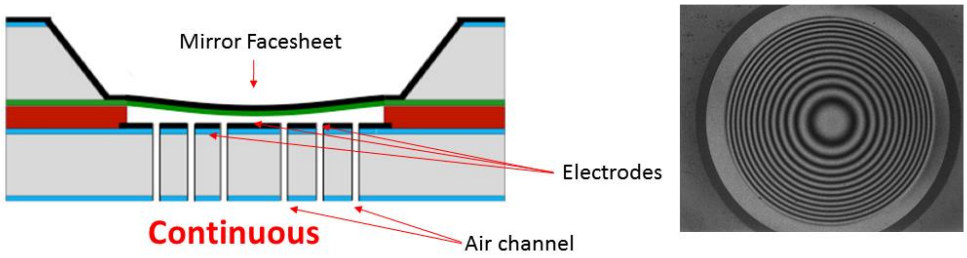

Figure 8. A cross section view of a FCDM. The structure of the MEMS mirror (left) and the interferogram shows the surface height of the membrane under electro-static actuation (right) [42] [5].

There is another type of electromagnetic FCDM commercially available for focus control with a slightly different structure as the FCDM shown in Figure 9. A representative can be the Mirao 52-e (Imagine Eyes, France) and DM468 (ALPAO, France). This type of FCDM usually has a continuous membrane capable of large

deflection. A high reflective coating is applied on the top of the membrane. The dynamic motion is driven by the magnetic actuators attached on the back side of the membrane. When current flows through the coils beneath the magnets, a local magnetic field is created, which attracts or repels the magnet depending on the sign of the applied current. Consequently, different wavefront maps can be created on the membrane.

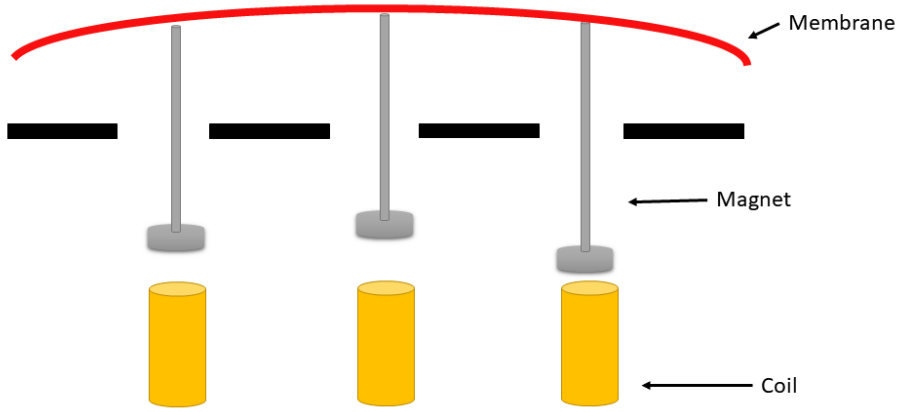

Figure 9. Mechanical structure of electromagnetic MEMS DMs

The electromagnetic FCDMs can support actuator count up to a few thousands on a pupil size of 90mm in diameter [43]. Tens of micron of deflection can be achieved on electromagnetic FCDMs. However, due to hysteresis and large inertia from the mass of the magnets, the settling time is usually ranges from 0.5 to 2ms. It will be too slow to keep up with the fast galvo-scanner to performance intra-scan focus control and aberration correction.

In previous publications [44] [45], FCDM is combined with MEMS DMs and implemented in the same adaptive optical system to fully utilize the versatility of MEMS

DMs and the larger range of deformation of FCDMs. This is the basic theory for the ‘woofer/tweeter’ configuration used in our active/adaptive TPFM design. In contrast to static aberration correction in previous publications, we utilize much faster adaptive optical elements in our ‘woofer/tweeter’ configuration to perform dynamic aberration correction.

System Implementation of Adaptive Optics for Microscopy

Much research has been done in the recent years on the application of adaptive optics in bioimaging, including CLSM [46] [47] [7], TPFM [48] [11], multiphoton microscopy [49] [30], OCM [50], and OCT [51] [52]. It has been reported that the adaptive optics system can lead to significant improvement in deep tissue imaging by compensating for tissue aberration effects.

There are mainly two ways of creating the target wavefront for aberration correction. The first way is to change the voltage applied to the actuator by modal or zonal approach, which are sensorless wavefront optimization. As a result, the best wavefront shape for imaging deep into the biological samples is created through thousands of iterations [29]. On the other hand, the distortion of the wavefront can also be detected by a Shack-Hartmann wavefront sensor (WFS), which consists of a two-dimensional sub-aperture of a lenslet array and CCD sensor. When an incoming beam arrives at the lenslet array, each sub-aperture divides the beam and provides a separate focus on the CCD sensor. By measuring the displacement of the local focus compared to the center of each sub-aperture, the slope of the local wavefront is determined so as to

reconstruct the incoming wavefront through each local wavefront. Upon knowing the incoming wavefront, a compensation can be made to cancel the aberrations carried in the incoming light [30]. Although direct detection with WFS can determine the amplitude of the aberrations much faster and more accurately once it is properly integrated into the optical system, it suffers from several significant disadvantages. Firstly, the extra optical elements required for direct wavefront sensing can increase cost and be labor intensive. Secondly, non-common path wavefront errors can be significant. Thirdly, the extra space required for WFS may not be possible for a compact imaging system. Nonetheless, both sensorless wavefront optimization and direct sensing are commonly used in microscopy.

Although many publications so far have not quantified the exact improvement in the penetration depth of imaging into biological samples through adaptive optics, many qualitative results have demonstrated the great potential of adaptive optics in depth imaging for high NA imaging techniques like TPFM, and OCM.

SELECTION OF ADAPTIVE OPTICAL COMPONENTS

Mathematical Modeling for the Tweeter DM

There are three types of configurations for the MEMS DM that are commercially available, which are the 1) segmented mirror facesheet with piston motion, 2) the segmented mirror facesheet with tip/tilt/piston motion, and 3) the continuous facesheet. The Figure 10 illustrates the setup of these DMs.

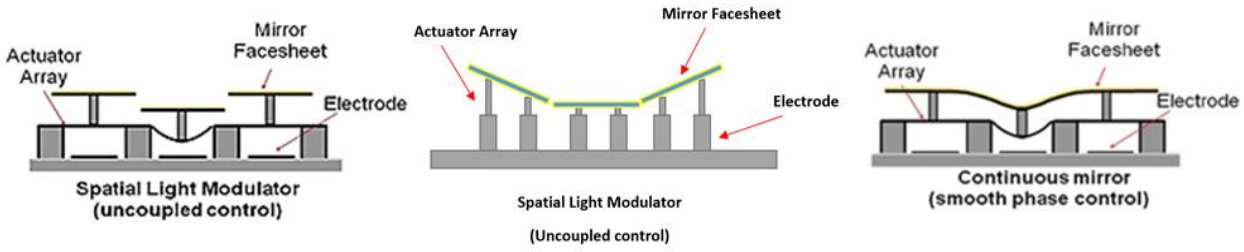

Figure 10. The three types of commercially available MEMS DMs. (left) A segmented facesheet with piston motion only (mid) The segmented facesheet with tip/tilt motion (right) A continuous facesheet for smooth phase control.

We are interested to know whether a segmented mirror is capable of creating the shapes that meet our prescription with a residual error that is small enough to achieve diffraction limited imaging.

These three types of MEMS DMs can all modulate the wavefront of the incident light beam with their own pros and cons. The 140-actuator count segmented facesheet with piston motion provides a solution with simplicity and high-speed modulation at a low cost. There is no coupling between neighboring electrodes, and each actuator drives individual mirror segments to the proper height to form a highly pixelated wavefront

map. Mathematical models are built in Matlab and these mirrors are analyzed by applying Fourier optics analysis to determine how well they can emulate a desired wavefront map of the typical Zernike aberration modes.

For Mathematical modeling, we are using the "normalized" polynomials for our Zernike basis, given explicitly here:

Defocus: $\tilde{Z}_{2,0}(\rho,\theta) = \sqrt{3}(2\rho^2 - 1)$

Astigmatism: $\tilde{Z}_{2,-2}(\rho,\theta) = \sqrt{6}(\rho^2 \sin 2\theta)$

Coma: $\tilde{Z}_{3,-1}(\rho,\theta) = 2\sqrt{2}(3\rho^2 - 2)\rho \sin\theta$

Vertical Trefoil: $\tilde{Z}_{3,-3}(\rho,\theta) = 2\sqrt{2}\rho^3 \cos 3\theta$

Primary Spherical: $\tilde{Z}_{4,0}(\rho,\theta) = \sqrt{5}(6\rho^4 - 6\rho^2 + 1)$

Secondary Astigmatism: $\tilde{Z}_{4,2}(\rho,\theta) = \sqrt{10}(4\rho^2 - 3)\rho^2 \cos 2\theta$

Secondary Coma: $\tilde{Z}_{5,1}(\rho,\theta) = \sqrt{10}(10\rho^4 - 12\rho^2 + 3)\rho \cos\theta$

As shown in Figure 11, two mathematical models have been built based on two segmented MEMS DMs, the IrisAO PTT111 and the Boston Micromachines Corp. Multi-DM.

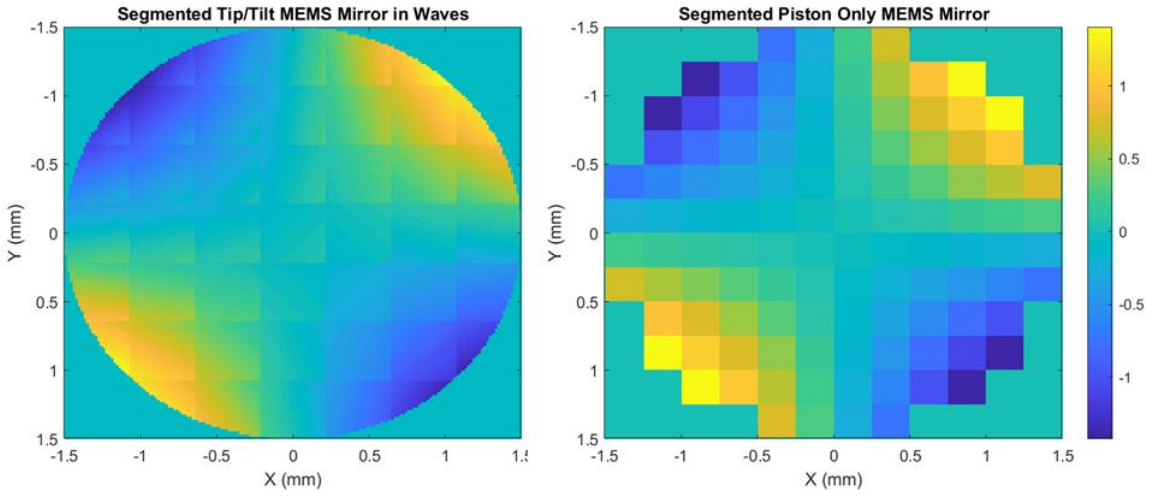

Figure 11. The mathematic modeling for the MEMS DMs with (a) The segmented facesheet with tip/tilt motion (b) segmented facesheet with piston motion only and.

For instance, the Strehl is calculated based on the difference between the target wavefront ($\tilde{Z}_{2,-2}$) and the wavefront created by the MEMS DMs as follows:

Equation 5. $W_{target} = 2 \times \tilde{a}_{2,-2}\, \tilde{Z}_{2,-2}(\rho, \theta)$

Equation 6. $W_{DM} = 2 \times \tilde{a}_{2,-2}\, DM_{2,-2}(\rho, \theta)$

Equation 7. $I_{err} = \left(\mathcal{F}\{W_{target} - W_{DM}\}\right)^2$

Equation 8. $strehl = \frac{I_{err,max}}{I_{0,max}}$

Where $\tilde{a}_{2,-2}$ is the amplitude of the Zernike polynomial, W_{target} and W_{DM} are the target wavefront and the wavefront created by the MEMS DM, I_{err} is the point spread function after aberration correction by the MEMS DM, and $I_{err,max}$ and $I_{0,max}$ are the maximum

intensity of the point spread function after aberration correction and the perfect point spread function.

As shown in Figure 11(a), the wavefront map being generated on the segmented piston motion only is $\tilde{a}_{2,-2}$ = 0.5μm of astigmatism ($\tilde{Z}_{2,-2}$). Even with 140 mirror segments, the simulation shows that the MEMS DM with piston motion only has such a large residue error due to the difference between the actual smooth wavefront and the pixelated wavefront on the MEMS DM, so that it can only recover the Strehl up to 0.3. This is not acceptable for diffraction limited imaging according to Marechal's criterion (Strehl $\geq$ 0.8).

On the other hand, the Iris AO PTT111 MEMS DM with segmented facesheet with tip/tilt/piston motion demonstrates a much better result even with fewer mirror segments. As shown in Figure 11(b), the MEMS DM has 49 mirror segments, but because each mirror segment can tilt to form a slope that is much closer to the desired wavefront, the residue/surface quality error has been driven to a small value that can nearly be ignored. With the same target wavefront of $\tilde{a}_{2,-2}$ = 0.5μm of astigmatism ($\tilde{Z}_{2,-2}$)., this type of MEMS DM can recover the Strehl over 0.92, which makes it a possible candidate for our application.

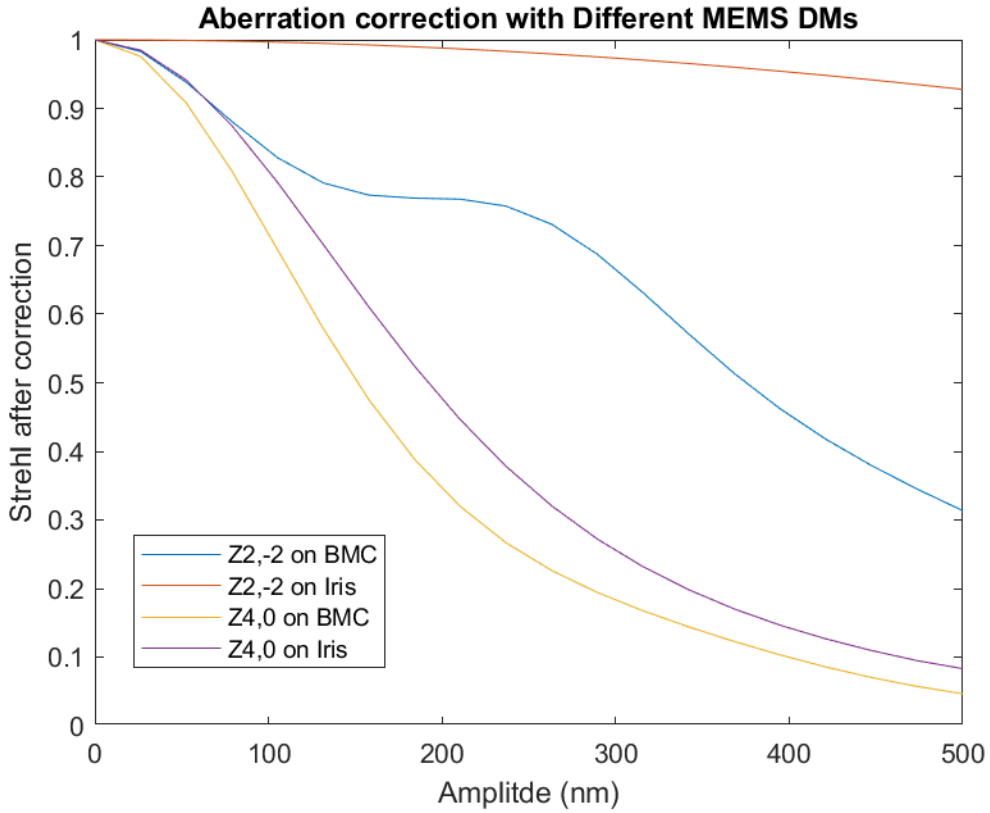

Figure 12. The achievable Strehl after aberration correction on astigmatism ($\tilde{Z}_{2,-2}$) and primary spherical aberration ($\tilde{Z}_{4,0}$) for different amplitudes

As shown in Figure 12, the achievable Strehl after aberration correction for the segmented piston motion only (BMC) and the segmented facesheet with tip/tilt/piston motion (Iris) are plotted against the target amplitude to be formed on the MEMS DMs. As the target wavefront amplitude increases, the Strehl that can be recovered after aberration correction decreases for all cases. However, the MEMS DM with segmented facesheet with tip/tilt/piston motion shows a superior performance.

Lastly, the continuous facesheet MEMS DM is expected to have the capability of producing the best wavefront map with the smallest residue/surface quality error, but

modeling the surface shape requires solving a complex influence function with many variables including air pressure, elasticity of the membrane, mechanical attachment to the membrane, coupling between electrodes, etc. Unlike the other two types of MEMS DM, the continuous facesheet MEMS DM requires a much more convoluted training process for the desired shapes, therefore, the proper training process also has a significant impact on the accuracy of the actual shape on the MEMS DM. Without sufficient data, it is nearly impossible to predict how well the continuous facesheet type MEMS DM can recover the Strehl. Nonetheless, the specifications provided from the manufacturer (Boston Micromachines Corp.) indicate that it has a surface quality error less than 40nm rms and a max frame rate over 200kHz, which makes it a good potential candidate for our application. We later confirm the surface height accuracy from measurements of the trained surface shapes of actual mirrors.

It is worth noting that while the published technical data on the mechanical response of the MEMS DMs provide an estimate of the static and dynamic performance that is possible, it does not provide quantitative information on the residual error that may be expected when driving to an actual prescription on the DM, or, just as important, how quickly the residual error will settle when switching from one prescription to another. Our testing directly measures this important performance.

Consequently, we acquired both the segmented facesheet with tip/tilt motion MEMS DM (IrisAO, Inc. PTT111) and the continuous facesheet MEMS DM (Boston Micromachines Corp. Muliti-DM) for further mirror training and testing. After initial testing, both the segmented facesheet with tip/tilt motion MEMS DM, and the continuous

facesheet MEMS DM demonstrated promising results with static aberration correction. However, the PTT111 could not support dynamic aberration correction due to synchronization limitations of the electronic interface. We moved on to dynamic characterization with BMC MEMS DM only. In this dissertation we only report on the static and dynamic performance of the continuous facesheet BMC MEMS DM from BMC.

In addition to these third party MEMS DMs for the “tweeter”, we fabricated a “woofer” FCDM with large stoke over 16μm for large amplitude of focus control and spherical aberration corrections here in the Montana State University Microfabrication facility [17] [16] [18]. Production of those mirrors has now been commercialized by Revibro Optics in Bozeman, MT.

Simulations with Zemax

To select and test appropriate MEMS mirrors, we need to know which Zernike modes will be most important in order to compensate systematic aberrations, and the magnitude of correction that will be required. Therefore, we performed a Zemax simulation of an optical system that was comprised of the MEMS mirrors, relays, scan lens, tube lens and a representative 25x 1.0 NA water immersion objective lens selected from the patent literature [53]. A more detailed description and schematic of the optical system is provided in the appendix. The MEMS mirrors are modeled as Zernike fringe surfaces, with the Zernike coefficients treated as variables for optimization. The focus

control mirror is capable of a stroke of 15μm, which corresponds to a focus adjustment of 80 μm using NA=1.0 in an aqueous sample.

The Zemax model is built with commercially available optical elements. As shown in Figure 13, the incident beam reflected from the tweeter illuminates the first doublet lens (f = 150mm), which acts as a single lens relay. The collimated incident beam becomes a diverging beam when it arrives at the woofer/focus control mirror. As the membrane of the woofer deflects, the diverging beam changes into a collimated beam, and a converging beam as more deflection on the woofer. The three focal depths for this simulation are chosen for the three following cases:

1. Furthest focus. Here the mirror surface of the woofer is flat ($Z_{2,0} = 0\mu m$). The focal depth is beyond the designed working distance of the objective.
2. Medial focus. At around 5μm of center deflection ($Z_{2,0} = -2.53\mu m$), the woofer collimates the incident beam and the same collimated beam illuminates the objective.
3. Nearest focus. The woofer at it maximum deflection ($Z_{2,0} = -7.5\mu m$), which pulls the focus towards the objective lens.

The woofer is then imaged onto the Y galvo through a 4f relay consisting of two identical doublets (f = 100mm). An additional 4f relay is used to image the Y galvo onto the X galvo.

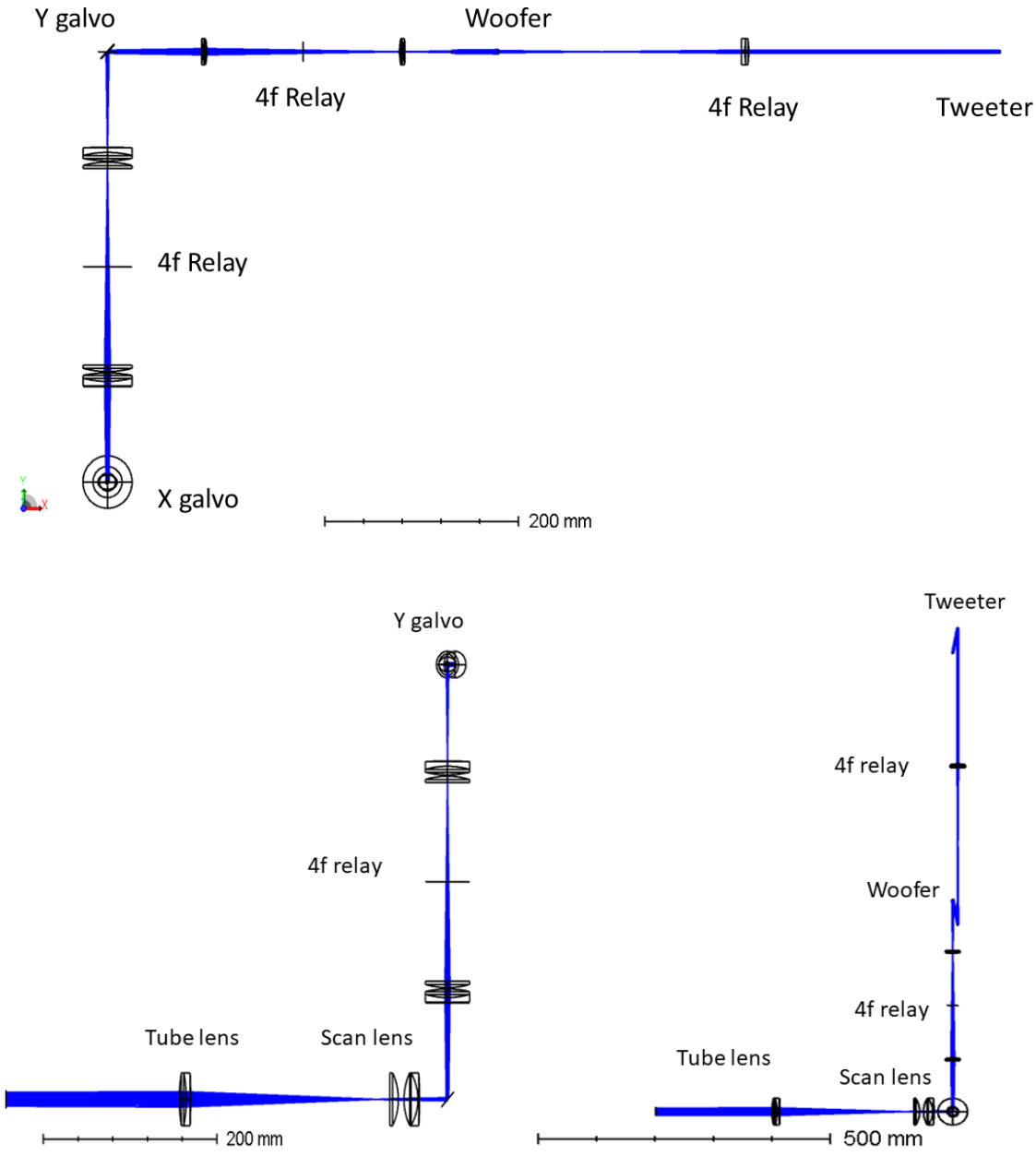

Figure 13. The Zemax simulation of the AO module with commercially available optics elements. Isometric view of the AO module in (upper) X-Y view; (lower left) Y-Z view; and (lower right) X-Z view.

The scan lens after the X galvo produce a flat image plane to minimize the distortion as the angle of the incident beam varies with respect to the optical axis of the

lens. It ensures the image is produced from a geometrically correct scanning pattern that requires no extensive post processing after image acquisition. Finally, a 200mm doublet is used to simulate the tube lens in a standard Nikon microscope stand (Nikon Eclipse TE300, USA).

The dominant aberrations of the optical system that the DMs must correct are coma $Z_{3,1}$ and spherical aberration $Z_{4,0}$ (we use the ANSI Standard $Z_{n,m}$ indexing scheme for radial order n and azimuthal frequency m), arising from the fact that the active focus control makes the objective lens operate at a focus location other than its optimum working distance. Other off-axis aberrations also come into play when the galvo-scanners steer the beam to larger scanning angles, with appreciable contributions from both the relay optics and the objective lens. The simulation results show significant astigmatism $Z_{2,2}$, secondary astigmatism $Z_{4,2}$, secondary coma $Z_{5,1}$, trefoil $Z_{3,3}$, and secondary spherical aberration $Z_{6,0}$. The range of simulated aberration coefficients are summarized in Table 1. Note that we are using the "un-normalized" polynomials for our Zernike basis, given explicitly here:

Defocus:	$Z_{2,0}(\rho,\theta) = 2\rho^2 - 1$
Astigmatism:	$Z_{2,2}(\rho,\theta) = \rho^2 \cos 2\theta$
Coma:	$Z_{3,-1}(\rho,\theta) = (3\rho^2 - 2)\rho \sin\theta$
Vertical Trefoil:	$Z_{3,-3}(\rho,\theta) = \rho^3 \cos 3\theta$
Primary Spherical:	$Z_{4,0}(\rho,\theta) = 6\rho^4 - 6\rho^2 + 1$
Secondary Astigmatism:	$Z_{4,2}(\rho,\theta) = (4\rho^2 - 3)\rho^2 \cos 2\theta$
Secondary Coma:	$Z_{5,1}(\rho,\theta) = (10\rho^4 - 12\rho^2 + 3)\rho \cos\theta$

Secondary Spherical: $Z_{6,0}(\rho,\theta) = 20\rho^6 - 30\rho^4 + 12\rho^2 - 1$

The wavefront maps are created during simulation of our instrument by inserting two Zernike standard phase surfaces in conjugate planes to the back aperture of the objective lens and galvo scanners. We are using a total of 22 standard Zernike terms in the Zemax model. The Zernike terms are indexed as described by Noll [54]. The values of these 22 terms are generated during the optimization process in Zemax for the highest Strehl ratio as well as the lowest peak to valley wavefront error. The Strehl ratio is chosen as the most important parameter due to the nonlinear optical phenomenon of the two-photon absorption, from which the intensity of the detectable signal is linearly proportional to the intensity squared of the incident illumination. A high Strehl ratio over 0.8 can guarantee not only a sufficient detectable signal but also a diffraction limited performance of the optical system.

The optimization was conducted at various focus locations as well as different scanning angles, and the corresponding Zernike coefficients are recorded in waves. Note that these are wavefront aberrations, so the mirror shape will have half of the indicated modal amplitudes.

The simulation results are as shown in Figure 14. The different wavefront maps needed to maintain a high Strehl over 0.8 at the different focus locations and scan angles with in the 500x500x80μm imaging volume.

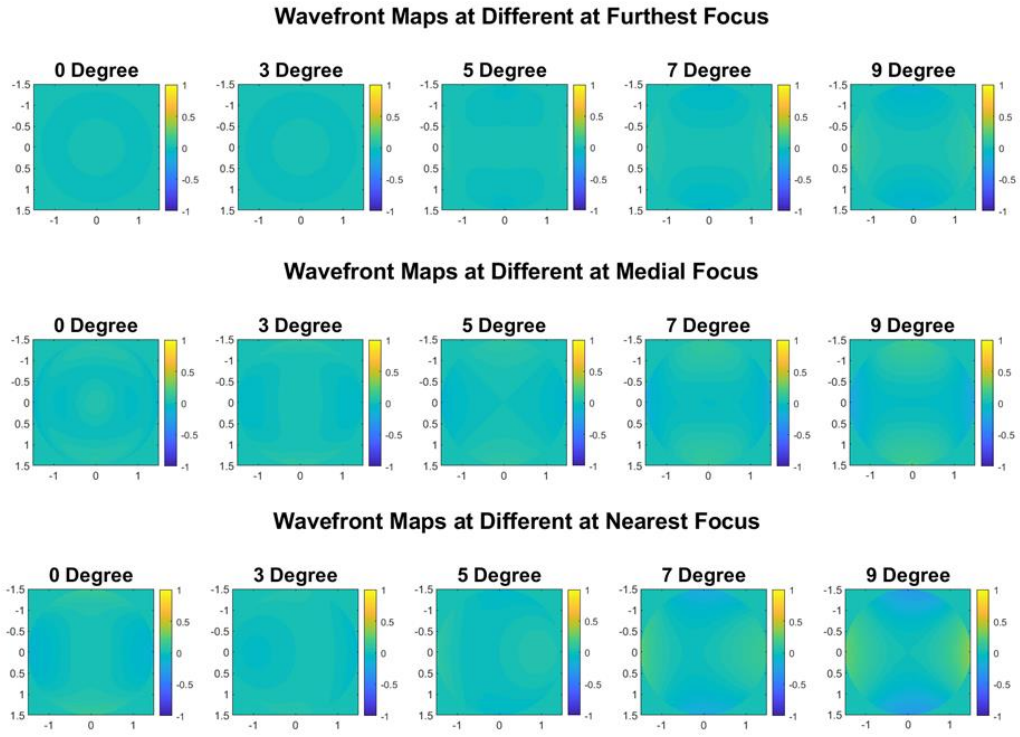

Figure 14. Aberrated wavefront shapes at different focal depth for the proposed woofer-tweeter from simulations of the relay in Zemax. All units for the scale bar are in waves at the design wavelength of 1μm.

At the three different focal depths, the 'furthest focus', 'medial focus', and 'nearest focus', the Zemax simulation of the AO module showed that wavefront maps needed for aberration correction consists mainly primary spherical aberration ($Z_{4,0}$), coma ($Z_{3,1}$) and astigmatism ($Z_{2,2}$). Moreover, the amplitude of each of these aberrations is noticeably small. It is an indication that the AO module that consists of MEMS deformable mirrors and relays are well designed.

On the other hand, the more significant source for aberration is the objective lens. A Zemax modal is built using the parameters reported from the patented literature [53]. The internal optical structure is illustrated as in Figure 15.

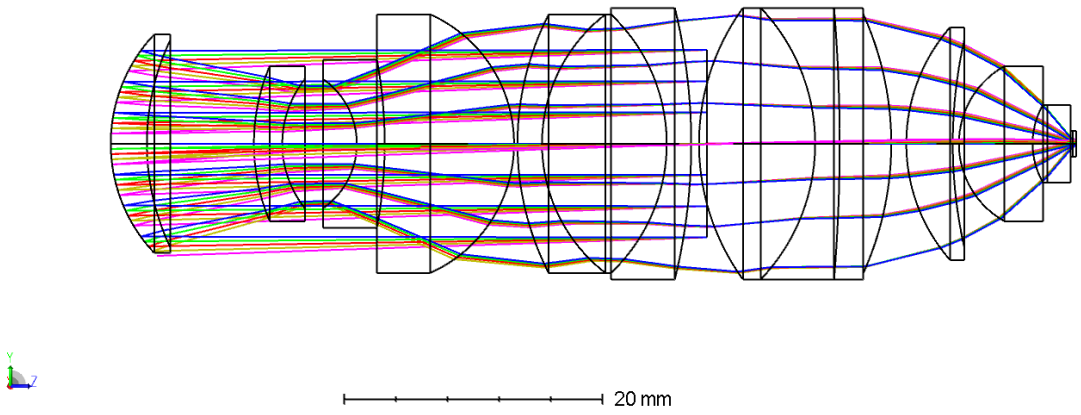

Figure 15. The isometric view of the representative 25x1.0 NA water immersion objective lens

As mentioned previously, the objective lens is optimized only for a fixed imaging depth. The focus control through MEMS DM introduces additional systematic aberration. The Zemax simulation results validate this assumption. The wavefront maps for the on and off-axis aberrations introduced by focus control is depicted in Figure 16.

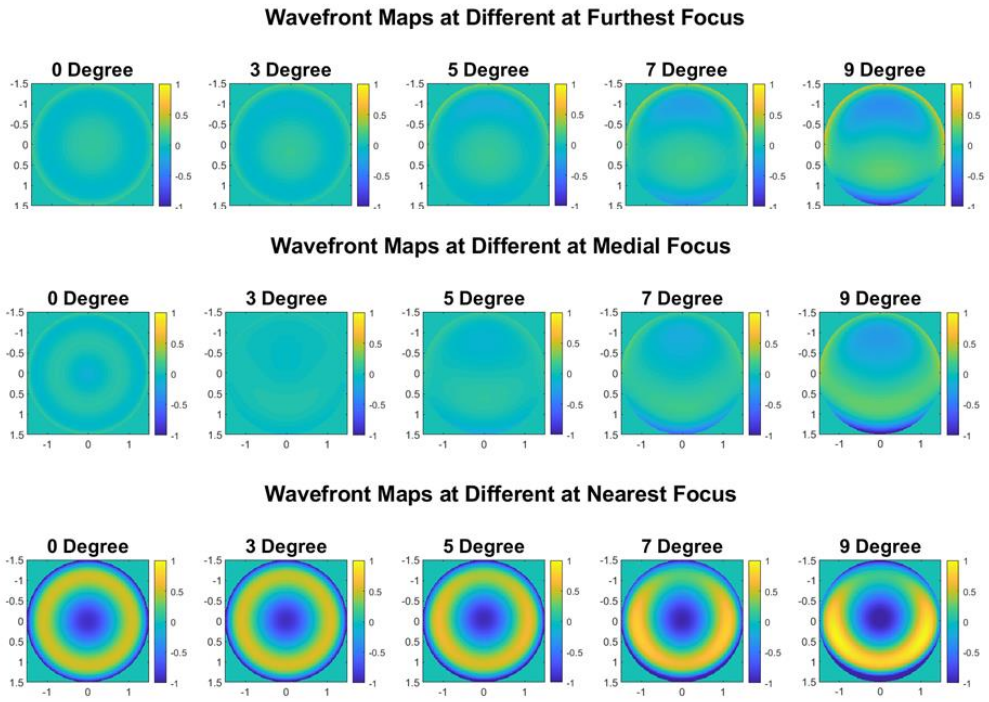

Figure 16. Aberrated wavefront shapes at different focal depth for the proposed woofer-tweeter from simulations of the objective lens in Zemax. All units for the scale bar are in waves at design wavelength of 1μm.

The Δz from the natural focus for these three simulated depths at the furthest, medial and nearest focus are +15, 0 and -65μm respectively. The aberration wavefront maps can be found by superimpose the aberrated wavefront shapes of the objective lens on the aberrated wavefront shapes of the relay. And the results are plotted in Figure 16.

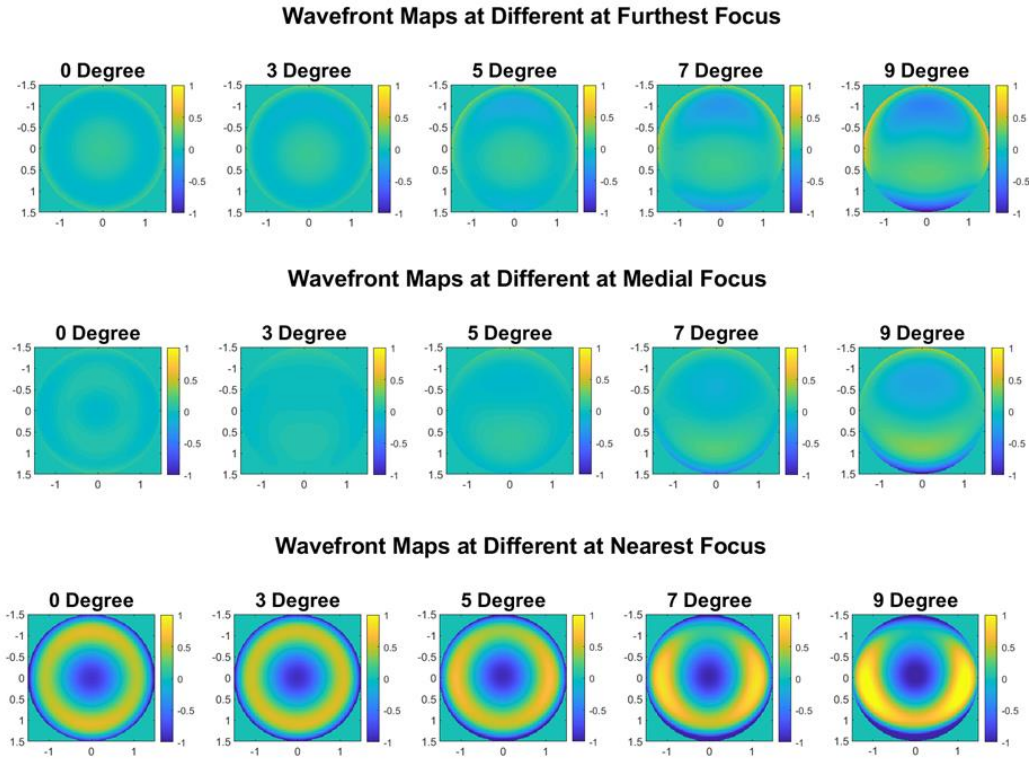

Figure 17. Aberrated wavefront shapes at different focal depth for the proposed woofer-tweeter from simulations of the entire optical system in Zemax. All units for the scale bar are in waves at design wavelength of 1μm.

The instrumental aberration for the optical system arise from the fact that the active focus control makes the objective lens operate at focus other than its optimal location. Off-axis aberration such as astigmatism and coma also come into play when the galvo scanner steer the beam to larger scanning angles. From simulation of the optical system in Zemax, the results also show a significant amount of astigmatism, coma, primary spherical aberration at different focus. Therefore, astigmatism, coma, primary spherical aberration and trefoil are chosen to be main shapes to be evaluated on the 'woofer' and 'tweeter' respectively. A summary of the systematic aberration from the simulation can be found in Table 2.

Table 2. The dominant aberrations over a 500 µm field of view and full 80µm focus range, from our Zemax model. The numbering of the Zernike terms follows the ANSI Standard Zn,m indexing scheme for radial order n and azimuthal frequency m.

Z. Terms	$Z_{2,2}$	$Z_{3,-1}$	$Z_{3,-3}$	$Z_{4,0}$	$Z_{4,2}$	$Z_{6,0}$
Mode amplitude range of the Wavefront aberration (nm)	(-928, 928)	(-692, 692)	(-130, 130)	(-1248, 131)	(-313, 313)	(-210, 27)
Mode amplitude range of surface deflection (nm)	(-464, 464)	(-346, 346)	(-65, 65)	(-624, 65)	(-156, 156)	(-105, 13)

SHAPE TRAINING ON BMC DM AND REVIBRO DM

With a phase-shifting Michelson interferometer, we are able to capture the surface height of the deformable mirrors. For analysis, the surface height is fit to 55 spatially orthogonal aberration modes (the un-normalized Zernike modes, up to order *n*=10), with the surface deflection *S* reconstructed according to $S = \sum_{n,m} a_{n,m} Z_{n,m}(\rho, \theta)$. Since the commercially available DMs do not come with a mapping between surface shapes and control voltages, the first task was to train the mirror to the target shapes we elected to test.

An iterative algorithm was used to find the control voltages that produced a single Zernike mode of desired amplitude, while suppressing all other terms. In brief, the algorithm for training the continuous facesheet MEMS DMs is as follows. A target surface shape was calculated for the desired mode. The mirror surface deflection was then measured using the interferometer, and the height of a region near the center of each actuator zone was compared to the target for that location. The control voltage V_i is updated according to $V_{i,n+1}^2 = V_{i,n}^2 + \alpha \epsilon_{i,n}$ where $\epsilon_{i,n}$ is the error between the target height and the measured height, and $V_{i,n}$ is the control voltage, for the i^{th} zone and the n^{th} iteration. The gain parameter α is chosen to facilitate convergence of the algorithm. We work with the square of the voltage, since the electrostatic force varies as the square of the applied voltage. It should be noted that because the BMC mirror and the Revibro mirror are electrostatically actuated and they can be deflected only in one direction. The Zernike modes, on the other hand, exhibit both positive and negative displacements. We therefore bias the mirror with an initial deflection, with the Zernike mode superimposed

on that initial shape. For the BMC mirror this initial deflection is an “active flat” surface. We train the membrane to be a flat plane at a height at the midpoint of its maximum deflection. This is the ‘active flat’. For the Revibro mirror the initial deflection is a midrange defocus setting that is purely parabolic in shape.

For analysis, the surface height is fit to 55 spatially orthogonal aberration modes (the un-normalized Zernike modes, up to order n=10), with the surface deflection S reconstructed according to $S = \sum_{n,m} a_{n,m} Z_{n,m}(\rho, \theta)$. Since the commercially available DMs do not come with a mapping between surface shapes and control voltages, the first task was to train the mirror to the target shapes we elected to test.

Defocus, Primary Spherical and Secondary Spherical Training on Revibro DM

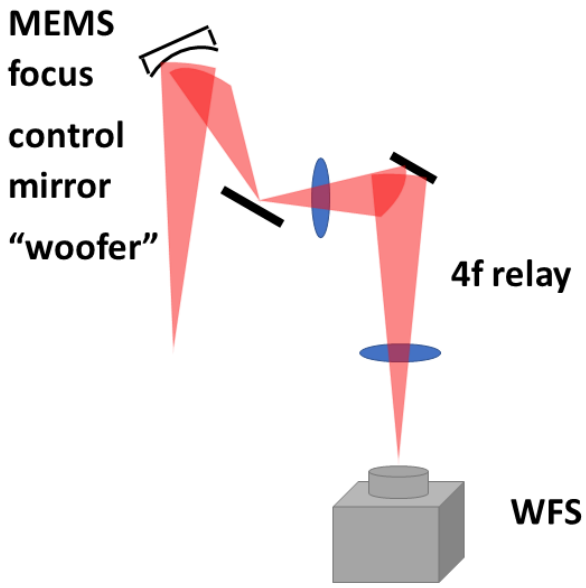

Figure 18. Schematic diagram for mirror shape training with WFS

The pre-requisite for successful sensorless wavefront optimization is that we has to be able to drive the MEMS DM to a desired shape with minimum rms error. For the woofer, we used a WFS as a feedback to obtain the transfer matrix for a conversion between desired shape on the woofer as well as a measurement for the accuracy of the shape trained. The setup is as shown in Figure 18.

The incident beam is a diverging beam illuminates the woofer. The illumination overfills the woofer and an iris is placed on the woofer as the stop of the entire optical system. The diverging beam allows the woofer to manipulate the wavefront to generate a range of defocus to form a diverging beam to a converging beam. The woofer is imaged

onto the WFS through a 4f relay so that we can define the area and the centroid accurately for Zernike polynomial fitting.

The training process begin with having 100V is applied on all 4 electrodes/zones on the Revibro DM. The electrode pattern is as shown in Figure 8. A cross section view of a FCDM. The structure of the MEMS mirror (left) and the interferogram shows the surface height of the membrane under electro-static actuation (right) .Figure 8. A linear sweep with equal voltages across the 4 zones on the Revibro DM from 100V to 300V (31 steps with 10V increment each step) is conducted to measure the voltages and $Z_{2,0}$ readout on the WFS. The fitting between voltages and $Z_{2,0}$ readout gives a 2^{nd} order polynomials equation for calculating focus adjustment and corresponding baseline voltages required.

A total of twenty-five different baseline focus settings, which are equally spaced from nearly zeros when Revibro DM is near flat to maxim focus adjustment when Revibro DM is at its maximum deflection, are chosen for spherical aberration training. The baseline voltages for these twenty-five different focus adjustments are then calculated from the fitting between voltages applied on Revibro DM and the $Z_{2,0}$ readout on the WFS. Then a small voltage variation from the baseline is chosen to generate a binary count for varying the voltages among each zone so as to characterize the spherical aberration produced on the Revibro DM. For instance, as baseline of 250V and a 20V variation will produce the following voltage maps for the total 9 tests.

Table 3. The binary count for defocus and spherical aberration characterization

		Voltages on each zone			
		Zone 1	Zone 2	Zone 3	Zone 4
Test number	1	250	250	250	250
	2	250	250	250	270
	3	250	250	250	230
	4	250	250	270	250
	5	250	250	230	250
	6	250	270	250	250
	7	250	230	250	250
	8	270	250	250	250
	9	230	250	250	250

At each test, the voltage on each zone is applied and the defocus ($Z_{2,0}$), primary spherical ($Z_{4,0}$) and secondary spherical ($Z_{6,0}$) readout from the WFS are recorded. The $Z_{2,0}$, $Z_{4,0}$ and $Z_{6,0}$ are then fitted to the variation in voltages in the following way. The basic assumption here is that the changes in voltage squared is linear to the changes in amplitude of the $Z_{2,0}$, $Z_{4,0}$ and $Z_{6,0}$ readout. A new voltage matrix is created by taking voltages squared from all four zones in test 2 to 9 and minus the baseline voltage squared, which gives the voltage variation matrix (volt2Data).

$$\text{Equation 9. } volt2Data = \begin{bmatrix} V_{1,2}^2 & \cdots & V_{4,2}^2 \\ \vdots & \ddots & \vdots \\ V_{1,9}^2 & \cdots & V_{4,9}^2 \end{bmatrix} - V_{baseline}^2;$$

$$In\ this\ case: V_{baseline} = 250$$

The measured $Z_{2,0}$, $Z_{4,0}$ and $Z_{6,0}$ readout for all 9 tests are save in another matrix (trainingInfo.zerns) with columns represents $Z_{2,0}$, $Z_{4,0}$ and $Z_{6,0}$ respectively and rows for different test numbers. The matrix for variation in $Z_{2,0}$, $Z_{4,0}$ and $Z_{6,0}$ readout is created in the following:

Equation 10. $zernData = \begin{bmatrix} Z_{2,0}^{(2)} & Z_{4,0}^{(2)} & Z_{6,0}^{(2)} \\ \vdots & \vdots & \vdots \\ Z_{2,0}^{(9)} & Z_{4,0}^{(9)} & Z_{6,0}^{(9)} \end{bmatrix} - \begin{bmatrix} Z_{2,0}^{(1)} & Z_{4,0}^{(1)} & Z_{6,0}^{(1)} \\ \vdots & \vdots & \vdots \\ Z_{2,0}^{(1)} & Z_{4,0}^{(1)} & Z_{6,0}^{(1)} \end{bmatrix}$

The $[Z_{2,0}^{(1)}\ Z_{4,0}^{(1)}\ Z_{6,0}^{(1)}]$here is the baseline $Z_{2,0}$, $Z_{4,0}$ and $Z_{6,0}$ readout when baseline voltages are applied on the Revibro DM. The transfer function X is then found by taking the left division of zernData and volt2Data.The transfer function X will allow us to calculate the required voltages (V_1, V_2, V_3, and V_4) on the each of the four zones on the Revibro DM to generate the desired $Z_{2,0}$, $Z_{4,0}$ and $Z_{6,0}$.

Equation 11. $X = zernData \backslash volt2Data;$

The voltages required on different zones are then calculate as shown in equation s below.

Equation 12.

$$volt2desired = \begin{bmatrix} V_{1,desired}^2 \\ V_{2,desired}^2 \\ V_{3,desired}^2 \\ V_{4,desired}^2 \end{bmatrix} = \left(\begin{bmatrix} Z_{2,0,\,desired} \\ Z_{4,0,\,desired} \\ Z_{6,0,\,desired} \end{bmatrix} - \begin{bmatrix} Z_{2,0,\,bias} \\ Z_{4,0,\,bias} \\ Z_{6,0,\,bias} \end{bmatrix} \right) \times X + V_{baseline}^2;$$

Equation 13. $voltDesired = \begin{bmatrix} V_{1,desired} \\ V_{2,desired} \\ V_{3,desired} \\ V_{4,desired} \end{bmatrix} = \sqrt{volt2desired}.$

Off-axis Aberration Trainings on BMC DM

Off-axis aberrations are non-radially symmetric Zernike shapes, which are more complex than defocus, primary and secondary spherical aberrations. To obtain more accurate shapes with minimum rms error, a Michelson phase-shift interferometer is used. This instrument has a piezo actuator installed on the sample stage, and it steps through 4 quarter-wavelength height adjustments and records the interferogram at each height. From these four interferograms, the mirror surface height can be calculated through phase reconstruction and subsequent unwrapping [55].

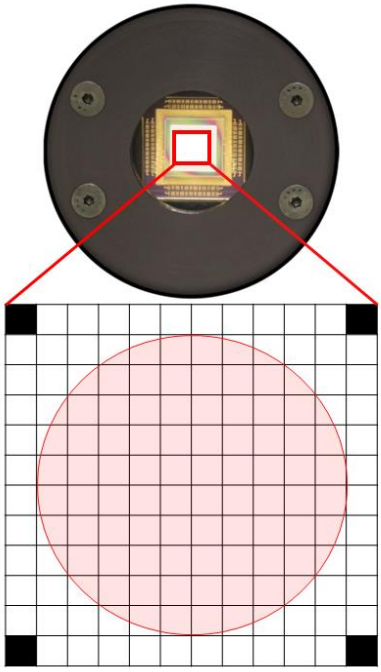

Figure 19. The BMC DM element chart

As mentioned in previous chapters, the BMC DM consists of a continuous facesheet supported by the active 12 by 12 grid of electrostatic actuators/posts. The membrane is a metal-coated active aperture. As shown in Figure 17, each of the 144 zones is in a shape of a square, with the actuator tethered to a small region at the center. There are 140 active actuators and the four actuators in the corners are fixed. The red circle in Figure 19 indicates the pupil size of the trained Zernike modal shapes. Although there are more actuators outside the circle are available for shape training, membrane edge effects on the most outside actuators can reduce the shape accuracy. Since it is a continuous membrane, the most outside actuators are coupled to the inactive mirror plane. The tension between the most outside actuators and the inactive mirror plane tends to increase wavefront error and reduce shape coherence. Therefore, we reduce the pupil size to the edge of the 10 by 10 grid, but we actively control the 12 by 12 grid to obtain the best shape possible. As the BMC DM has a 400μm pitch for each actuator and thus the Zernike pupil has a diameter of 4mm. The most outside actuators are used as a buffer so that a smooth transition can be created from the inner post height to the flat surface of the inactive mirror plane.

These posts can be driven to desired heights by setting a proper voltage. With no voltage applied on the actuators, the membrane is in a slightly bowed shape. The Zernike modal shapes are all computed relative to the ‘active flat’ as described in previous section. In general, the actuator deflection is proportional to the electrostatic force applied on the actuator. The electrostatic force is in turn proportional to the square of the voltage

on the actuator. Therefore, the change in deflection of the post height is roughly proportional to the change in the square of the voltage on the actuator.

Equation 14. $\Delta d \propto \Delta(V^2)$

The height of each one of the 12 by 12 actuators can be calculated with the 2D equation governs each Zernike mode. The hypothesis here is that we can superimpose scaled $\Delta(V^2)$ maps onto the active flat V_{flat}^2 baseline.

During training of each Zernike shapes, the 140 parallel voltages are iteratively adding or subtracting the sum of the current voltage squared and difference of current post height to the desired post height multiplied by a scaling factor. The mathematical procedure is listed as below.

$$\Delta(V_{old}^2) = V_{old}^2 - V_{flat}^2$$

$$\Delta(V_{new}^2) = \Delta(V_{old}^2) \pm \alpha \times (d_{desired} - d_{current})$$

$$V_{new}^2 = \Delta(V_{new}^2) + V_{flat}^2$$

$$V_{new} = \sqrt{V_{new}^2}$$

where the V_{new} is the new voltage, V_{old} is the current voltage, V_{flat} is the voltage corresponding to the active flat, $d_{current}$ is the current post height, $d_{desired}$ is the target post height and the α is the scaling factor.

One remark to make here is that the scaling factor α has a significant impact on the training outcome. A large value of α can make the close loop training converge much faster to achieve the target shape, but it can also make the loop unstable that it never converges. On the other hand, a small value of α will make the close loop training more stable which can lead to a much more accurate shape to be trained on the BMC DM.

However, the drawback is that the training would require more iterations, thus higher cost of time and computation power. Generally, we make the α a variable rather than a constant. The close loop training starts with a large α but it is gradually reduced to stabilize the loop, which keeps close loop training at its optimal.

We were successful in training each of the test modes, with residual contribution from all other modes less than 20 nm rms. Height maps from these trained shapes on the BMC multi-DM are shown in Figure 20.

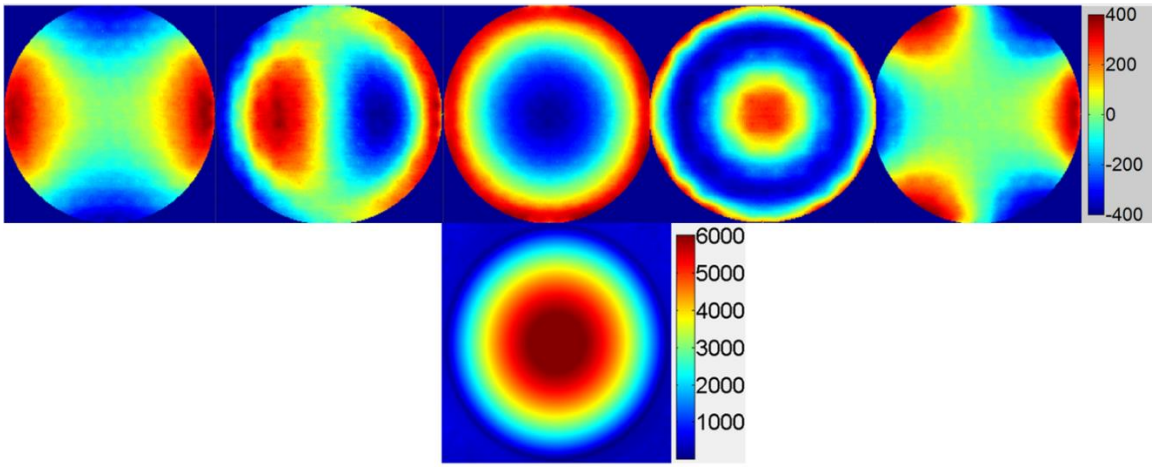

Figure 20. (Upper) Standard Zernike shapes trained on the BMC Multi-DM using a closed loop feedback training process. From left to right, Astigmatism, Coma, Defocus, Primary Spherical and Trefoil. The amplitude for these standard Zernike shapes is 400nm. The residual rms error on these shapes are 5nm, 19nm, 7nm, 20nm, and 12nm for Astigmatism, Coma, Defocus, Primary Spherical and Trefoil, respectively. (Lower) 300nm primary spherical aberration superimposed on 3µm defocus trained on the Revibro deformable mirror. [5]

Combination of Multiple Zernike Shapes of Desired Amplitude

The woofer tweeter configuration enables the AO module to correct aberrations of multiple Zernike shapes simultaneously at high speed during active scanning. The woofer

(Revibro DM) can produce a combination of defocus, primary spherical and secondary spherical aberration by changing the differential voltage among the 4 electrodes. It is then imaged onto the tweeter (BMC DM) through a single lens relay so that the woofer and tweeter are in conjugate planes. All the off-axis aberration correction is performed with the tweeter. In this case, different shapes of Zernike modes are combined in the following way. The close loop training on the BMC DM produced a series of voltage maps as reference for Zernike mode ranging from $Z_{2,2}$ to $Z_{5,5}$ (25 modes in total). The first step is to calculate the voltage for the target Zernike shape.

Equation 15. $$V_{Target} = \sqrt{\left(V_{reference}^2 - V_{flat}^2\right) \times \frac{a_{desired}}{a_{reference}} + V_{flat}^2}$$

where the V_{Target} is the voltage for the desired amplitude of the target Zernike shape, $V_{reference}$ is the voltage for the reference amplitude of the target Zernike shape, $a_{desired}$ is the desired amplitude, $a_{reference}$ is the reference amplitude and V_{flat} is the voltage for the flat wavefront map.

Equation 16.

$$V_{combined} = \sqrt{\left(V_{Astigmatism}^2 - V_{flat}^2\right) + \left(V_{Coma}^2 - V_{flat}^2\right) + \left(V_{Trefoil}^2 - V_{flat}^2\right) + \cdots + V_{flat}^2}$$

$$V = \sqrt{\frac{a_{2,2}}{a_{2,2ref}}\Delta\left(V_{2,2}^2\right) + \frac{a_{3,1}}{a_{3,1ref}}\Delta\left(V_{3,1}^2\right) + \cdots + V_{flat}^2}$$

where V is the combined voltage for the combination of multiple Zernike shapes of desired amplitudes $a_{n,m}$, where $\Delta\left(V_{n,m}^2\right)$ is the squared voltage difference for the trained *n,m* mode with reference amplitude $a_{n,mref}$. One remark to be made here is that the

voltage here is a 12 by 12 matrix, and each element contains a voltage value for the 144 actuators/posts (although the four corner values are ignored by the hardware since those actuators are fixed).

DYNAMIC TESTING OF MEMS DM

The following introductory section is a verbatim excerpt from our previous publication in the Journal of Biomedical Optics [5]. Fully flexible 3D acquisition can be realized only if the focus and aberration correction mirrors can be modulated quickly enough to keep up with the fast scan galvo mirror. To frame the problem in a more quantitative way, we might consider segmenting a single fast scan into multiple zones, with a unique focus or aberration setting in each zone.

Since speed is critical for active scanning and intra-scan focus control and aberration correction, liquid crystal spatial light modulators that can achieve frame rates up to a few hundred Hertz are too slow and were not considered. On the other hand, commercially available MEMS DMs have electronic update rates of hundreds of kHz and published mechanical response times of tens of μs, making them candidates for this application. Furthermore, previous publications demonstrate that MEMS DMs are capable of correcting sample induced aberration in a variety of tissue types up to imaging depths of a few hundred microns [11] [13] [56]. Having measured the actual step response or frequency response of a potential DM, we can then make an informed choice about the maximum galvo scan rate, or the complexity of the mirror trajectory, that might be possible while maintaining imaging integrity.

Stroboscopic interferometry can effectively freeze high-speed motion when the light pulses are sufficiently short and synchronized with the periodic movement of the MEMS DMs. We have constructed a custom phase-shifting Michelson interferometer with stroboscopic interferometry for dynamic testing.

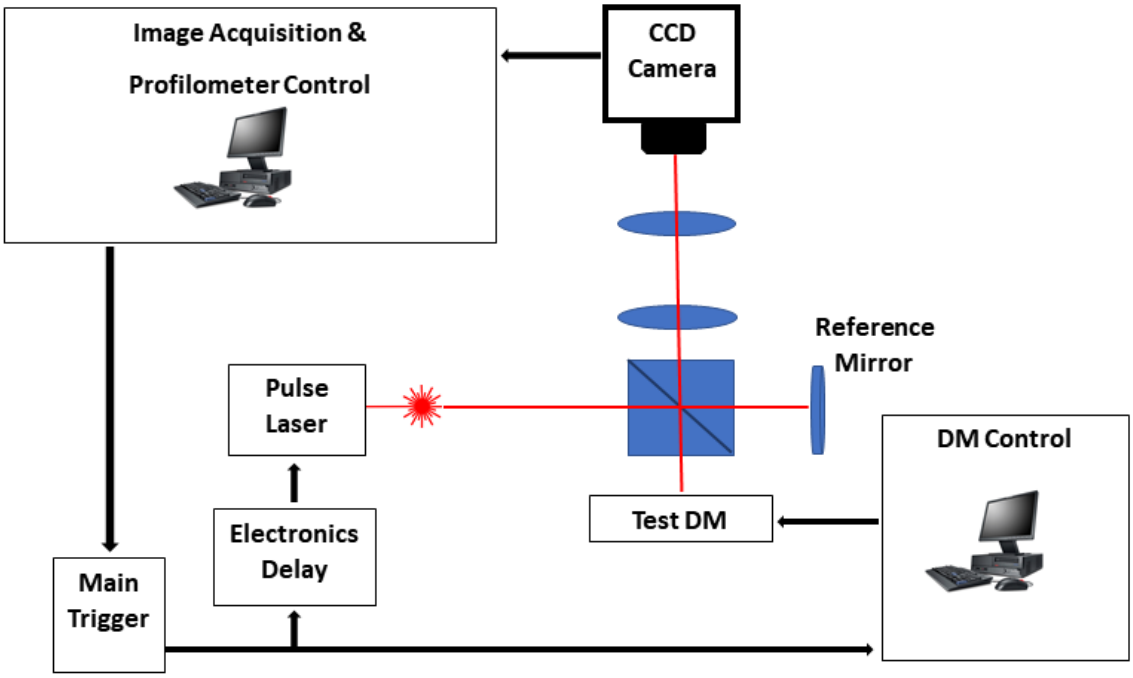

Figure 21. The system setup for dynamic testing using stroboscopic phase-shift interferometry.

Sinusoidal Steady State Response

For continuous intra-scan correction of aberrations such as coma or astigmatism, the time dependence of any particular wavefront shape will be nearly periodic, synchronized to the fast-scan mirror. In order to quantify the capability of the DM we chose to measure a sinusoidal steady state frequency response for specific aberration modes. The mode amplitude is varied sinusoidally at a particular frequency, and the mirror response is measured in terms of amplitude and phase delay of that specific mode relative to the driving waveform. These are plotted vs. frequency using a Bode style plot.

As shown in Figure 22, a sampled sinusoidal signal at frequencies ranging from near DC to several kHz drives the MEMS DM. For the BMC DM, a pulse triggers a new voltage map to be assigned to the 140 actuators, with 12 shapes per period comprising the stepwise sinusoidal trajectory. For example, in the figure, the mirror is driven to 12 different amplitudes of trefoil, with the amplitude following a sinusoidal time dependence. Synchronously, the phase-shifting interferometer strobe is progressively set to 6 different sampling delays, generating 6 different height maps. Each height map is decomposed into Zernike modes, and the measured amplitude of the mode of interest is then curve fit to find the magnitude, and the phase relative to the driving phase. Using the X-driver and high speed camera card (X-CL^{TM} PCIe Interface Card) we can update the BMC voltage map at a maximum speed of 400 kHz. This sets a maximum sinusoidal test frequency of 400/12=33 kHz. Our tests included a maximum sinusoid frequency of 12.5 kHz.

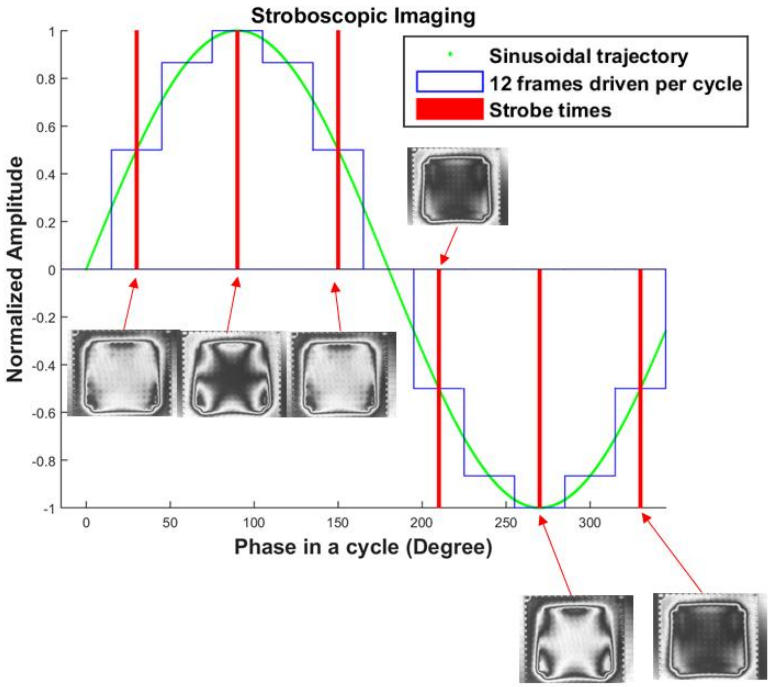

Figure 22. Stroboscopic imaging for frequency response. 12 frames of 12 different amplitudes (trefoil shown in the figure) form a periodic sinusoidal movement on the BMC DM, and the sub-microsecond light illumination pulses take place at 30^{o}, 90^{o}, 150^{o}, 210^{o}, 270^{o} and 330^{o} in each cycle to capture the instantaneous movement of the BMC DM.

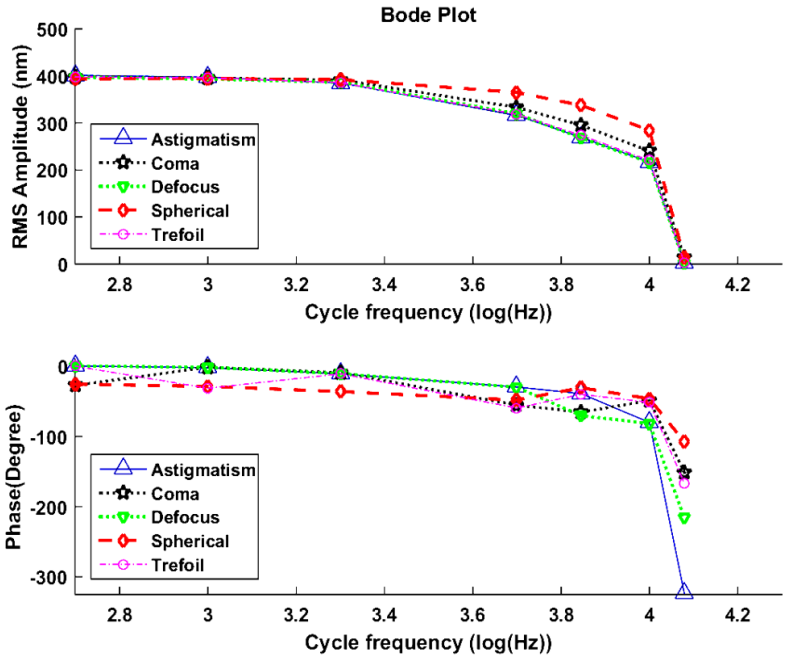

Zernike Mode	f_{3dB} (kHz)
Astigmatism	6.5
Coma	7
Defocus	6.7
Spherical	10
Trefoil	6.5

Figure 23. Frequency response for different standard Zernike shapes on the BMC Multi-DM [5].

Figure 23 plots the magnitude and phase response for five different Zernike modes on the BMC Multi-DM. The results show that astigmatism, defocus and trefoil exhibit a 3dB frequency near 6.5 kHz. Coma has a 3dB frequency closer to 7 kHz, while spherical aberration has the largest 3 dB bandwidth near 10 kHz. All modes were driven with the same 400 nm amplitude, but the membrane shapes are different, as are the peak-to-peak deflections. Defocus, astigmatism, coma and trefoil all have peak-to-peak displacement of the membrane equal to twice the Zernike amplitude (800 nm), while spherical aberration has peak to peak displacement of 1.5 times the amplitude (600 nm). The higher 3 dB frequency of spherical aberration thus seems to correlate to smaller peak-to-peak membrane deflection; but the damping due to air flow beneath the

membrane is important, and its dependencies on mode shape and on amplitude have not been separated here. It is noteworthy that the frequency response for all modes shows a smooth roll-off with no peaking, indicating that these mirrors are over-damped and exhibit no resonances at least up to 12.5 kHz.

Zernike Modal Step Response

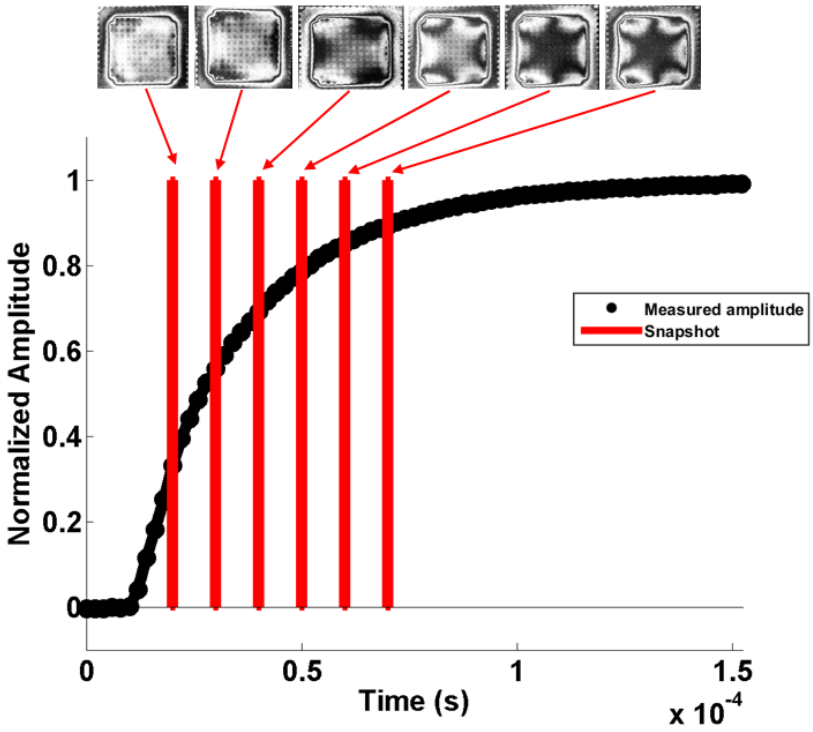

Figure 24. Stroboscopic imaging for a step response. The sub-microsecond illumination pulses capture the instantaneous movement of the rising edge during a step from flat to the target amplitude of a specific Zernike mode (trefoil shown as in the figure). By using proper delays, we evaluate the full evolution of the mirror shape.

To capture fast transients of the MEMS DM with a periodic square-wave driving signal, we use a short laser diode pulse ranging from 400ns to 1us. The short pulse width

ensures that averaging during image acquisition on the CCD camera will not degrade the fringe contrast of the interferogram. A pulse train with a proper delay has been created to capture 100 points spanning 200μs during the rising edge and falling edge for the step response.

Under the weak aberration limit, a Strehl intensity $I \geq 0.8$ (diffraction limited) corresponds to the rms wavefront error less than 1/14 of the operating wavelength (the Maréchal condition). Therefore, when plotted against time, the rms error can function as a good indicator to tell not only how fast the mirror can achieve the desired shape but also how soon the MEMS DM can compensate the target aberration to achieve diffraction limited imaging. After the Zernike shape fitting, we are able to gather a matrix that contains the amplitudes of each Zernike polynomial, from which the residual rms error is calculated using the following equation.

Equation 17. $Error_{rms} = \sqrt{\sum_{n,m}(N_{n,m}(a_{n,m} - a_{n,m\ target}))^2}$

where $a_{n,m}$ is the amplitude of each Zernike term from the surface height fitting, $a_{n,m\ target}$ is the amplitude of the target shape of the specific Zernike mode, and $N_{n.m}$ is the rms normalization factor of the Zernike polynomial for the specific term,

Equation 18. $N_{n,m} = \begin{cases} 1/\sqrt{n+1}, & m = 0 \\ 1/\sqrt{2(n+1)}, & m \neq 0 \end{cases}$.

Note that our error is for the mirror surface, so in order to maintain a wavefront error less than λ/14 we must keep the mirror surface height error to less than λ/28, since the mirror is used at near normal incidence where the wavefront retardation upon reflection is twice the mirror height variation. Assuming a two-photon excitation

wavelength of λ=1.0 μm, the error threshold for λ/28 is 36nm rms. This threshold value is used when analyzing the error relaxation responses.

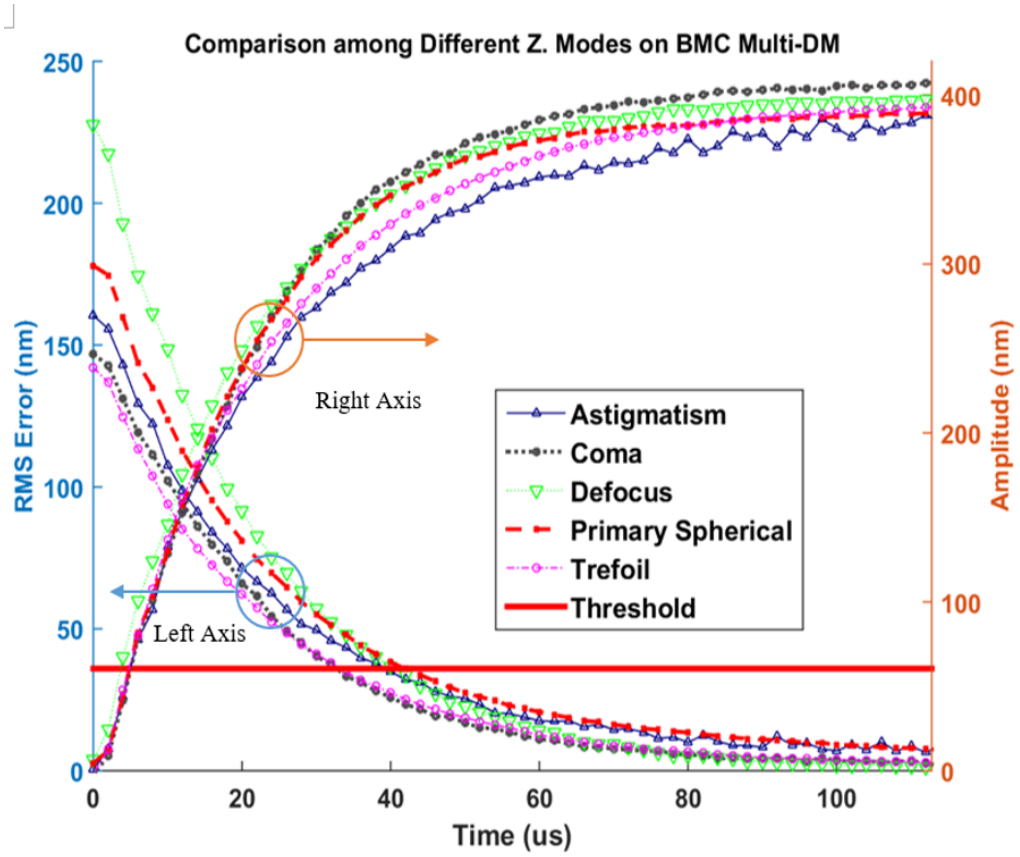

Figure 25. Step response for different tested Zernike modes at a step from 0 to 400nm in amplitude on the BMC Multi-DM (referred to right side y-axis). The rms error is also plotted against time for each Zernike mode step (referred to the left y-axis). The solid line at 36 nm RMS error is the threshold to recover to 80% Strehl, according to the Marechal's criterion (λ=1.0 μm) [5].

Figure 25 shows step response measurements for 5 different Zernike modes. Each mode was driven from the active flat membrane position to the mode shape with 400 nm amplitude. 10% to 90% rise times are calculated and tabulated in Table 2. Rise times measured for all 5 aberration modes ranged from 44 μs to 61 μs. By computing the rms

surface deviation from the final target shape we can plot rms surface error vs. time in an error relaxation plot. Although the step height for each mode has the same 400 nm amplitude, these are the non-normalized Zernike modes and so exhibit a different rms deviation. That is reflected in the starting rms error value for each of the 5 modes. Note that the RMS error includes the error contribution from all modes, including the mode that is being stepped; the full transient membrane shape is accounted for. A meaningful metric is the error settling time, when the overall mirror rms error is less than $\lambda/28$, corresponding to Maréchal's criterion for Strehl ≥ 0.8. With $\lambda = 1.0$ μm this limit is 36 nm rms, which is indicated by the solid red line in Figure 25. Error settling time for all five of these mode steps is less than 42 μs. The results are tabulated in Table 5.

Table 4. Summary of the rise time for the BMC Multi-DM [5]

	Rise Time (μs)					
	100nm	200nm	300nm	400nm	500nm	-400nm
Astigmatism	41	54	56	61	57	55
Coma	57.6	41	42	45	43.6	45
Defocus	42	49	51	44	48	61
Spherical	42	37	36	44	37	39
Trefoil	61.5	53	53	52	52	52

Table 5. The time needed for the BMC MEMS DM to settle below 36nm of RMS error to achieve diffraction limited imaging. [5]

	Settling Time (μs)					
	100nm	200nm	300nm	400nm	500nm	-400nm
Astigmatism	3.3	22	32	40	46	38
Coma	2	14	18	32	37.5	32
Defocus	9	30	38	40.5	48	52
Spherical	6	24	32	42	40	36
Trefoil	2	17	28	33.5	40	34

We also investigated the influence of mode amplitude on step response and error settling time. Fig 10 shows a family of step response curves for astigmatism with amplitudes ranging from 100 nm to 500 nm, and also -400 nm. Rise times range from 40 μs for the smallest step to 63 μs for the 400 nm step. Error settling times show a particularly strong dependence on mode amplitude, since the threshold of 36 nm error is barely exceeded for the full amplitude 100 nm astigmatism step. Even the 500 nm astigmatism step settles to within the 0.8 Strehl limit within 46 μs.

Table 4 summarizes the rise times, and Table 5 summarizes the wavefront error settling times for all five tested modes for amplitudes from 100 nm to 500 nm and -400 nm. Within this range of correction all of the steps reach the threshold for diffraction-limited precision in less than 52 μs.

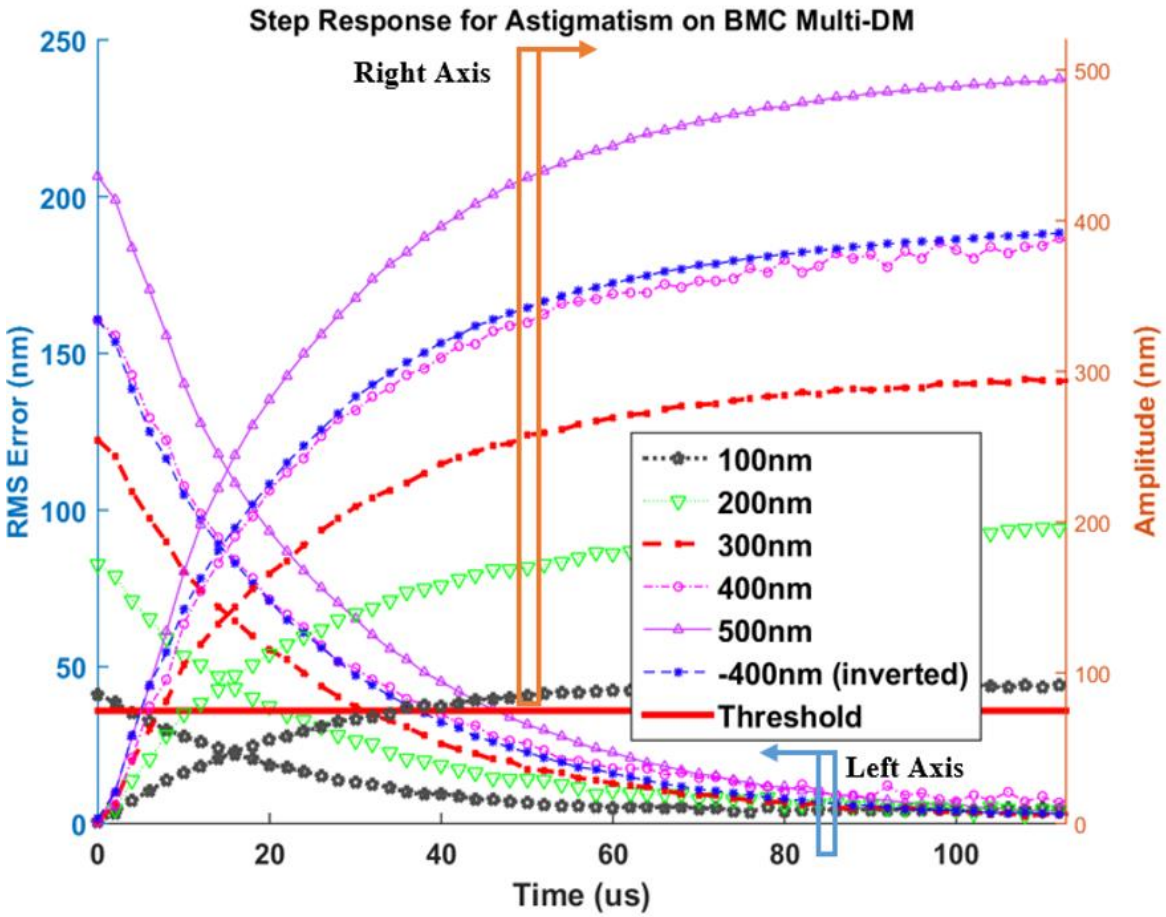

Figure 26. Step response for different amplitudes of astigmatism on BMC Multi-DM and the RMS error is plotted against time for astigmatism on BMC Multi-DM at its rising edge during a step response [5].

Figure 27 plots the response for five different defocus steps of the Revibro DM. The peak-to-peak deflection is twice the Zernike amplitude, so that 1 µm and 8 µm steps correspond to mirror sags of 2 µm and 16 µm, respectively. We see that the step response is somewhat underdamped with a slight overshoot, so that the error plots show some oscillation. The smaller step from 2.9 to 3.1 µm also shows a slight overshoot. Rise times (10%-90%) range from 28 µs to 39 µs for these tests.

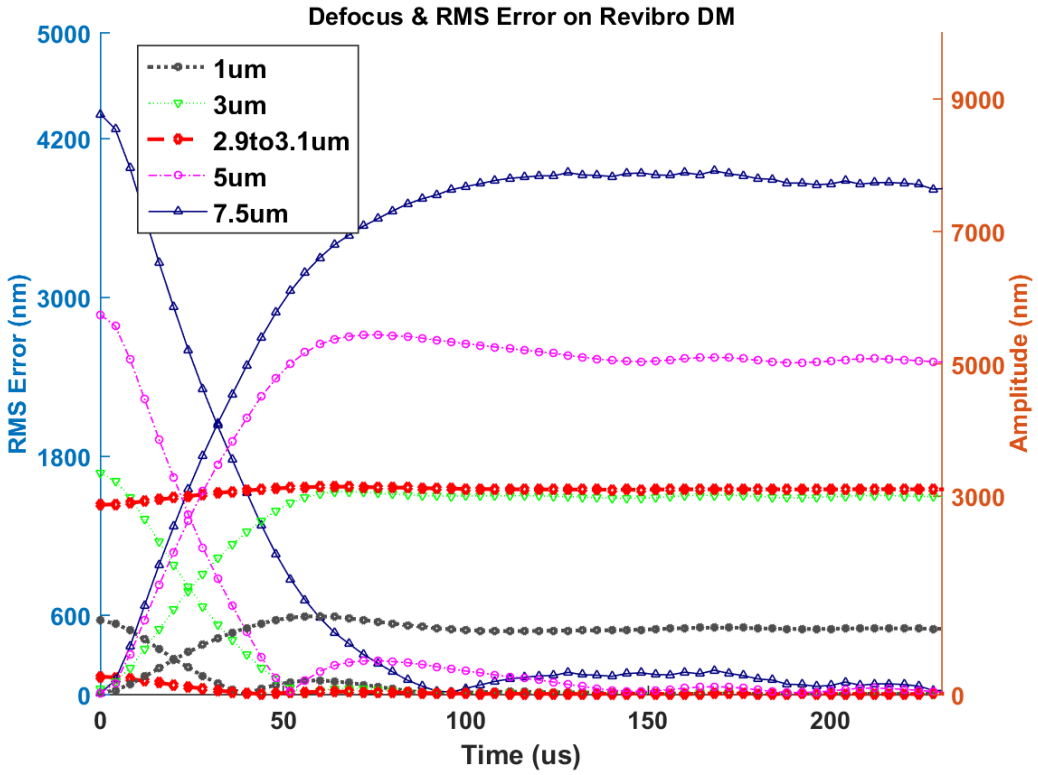

Figure 27. Step response of active focus control with Revibro MEMS DM at 0-1µm, 0-3µm, 2.9µm to 3.1µm, 0-5µm and 0-7.5µm. The RMS error is also plotted against time at the rising edge of a step response for different amplitude in focus control on the Revibro Multi-DM [5].

Because of the ringing in the step response, the settling times are a bit longer for the larger focus steps, all of which require at least 76 µs (up to 226 µs for maximum deflection at 8 µm) to reach a diffraction limited shape. The smaller defocus step from 2.9 to 3.1 µm has an error that settles much faster, in about 32 µs. The rise times and settling times for defocus on the Revibro mirror are summarized in Table 6. Summary of dynamic performance for defocus on Revibro MEMS DM

Table 6. Summary of dynamic performance for defocus on Revibro MEMS DM.

	Defocus on Revibro DM				
	1 μm	3 μm	2.9 to 3.1 μm	5 μm	8 μm
Rise time (μs)	28	39	32	37	58
Settling time (μs)	82	76	32	138	226

Finally, we measured the step response for a change in spherical aberration $Z_{4,0}$ on the Revibro mirror. We characterized mode amplitudes of 200 nm, 400 nm and 600 nm. These are superimposed on a defocus bias of 3 μm (6 μm mirror sag). The Result is plotted in Figure 28. More ringing is observed for these steps, showing that the spherical aberration shape is less damped in this free-standing membrane. The rise times are quite short, less than 15 μs. The error settling times are variable, ranging from 16 μs to 50 μs, affected by the oscillation in the step response. The rise times and error settling times for primary spherical aberration on the Revibro DM are summarized in Table 7.

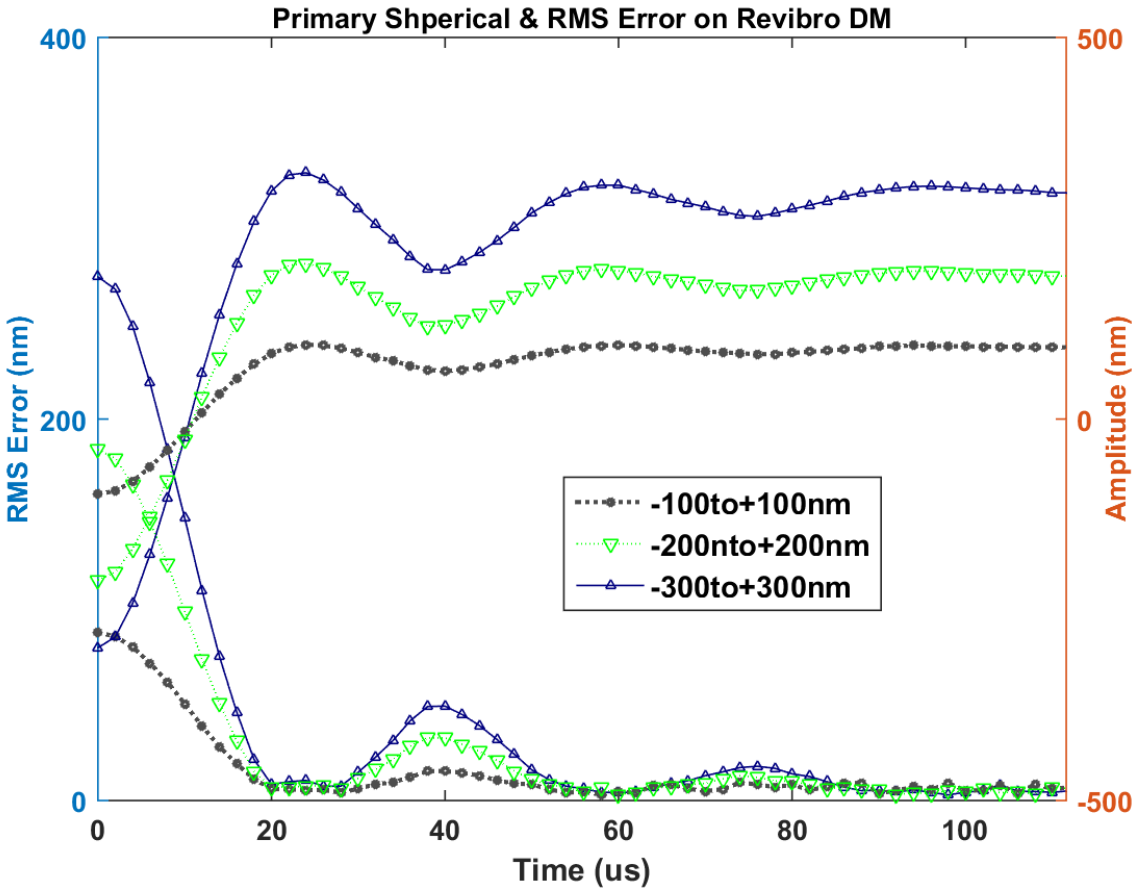

Figure 28. The step response for different amplitudes in spherical aberration correction on the Revibro MEMS DM. The RMS error (with defocus set to 0) during the step response is also plotted (referred to y-axis on the left side) [5].

Table 7. Summary on dynamic performance for primary spherical aberration on Revibro MEMS DM [5]

	Primary Spherical on Revibro DM		
	-100 to 100nm	-200 to 200nm	-300 to 300nm
Rise time (μs)	14	13.4	13.4
Settling time (μs)	13	15	45

Here is the end JBO excerpt.

ACTIVE/ADAPTIVE MICROSCOPE CONSTRUCTION

Schematic of the Active/Adaptive Laser Scanning Microscope

Here is the schematic diagram as shown in Figure 29.

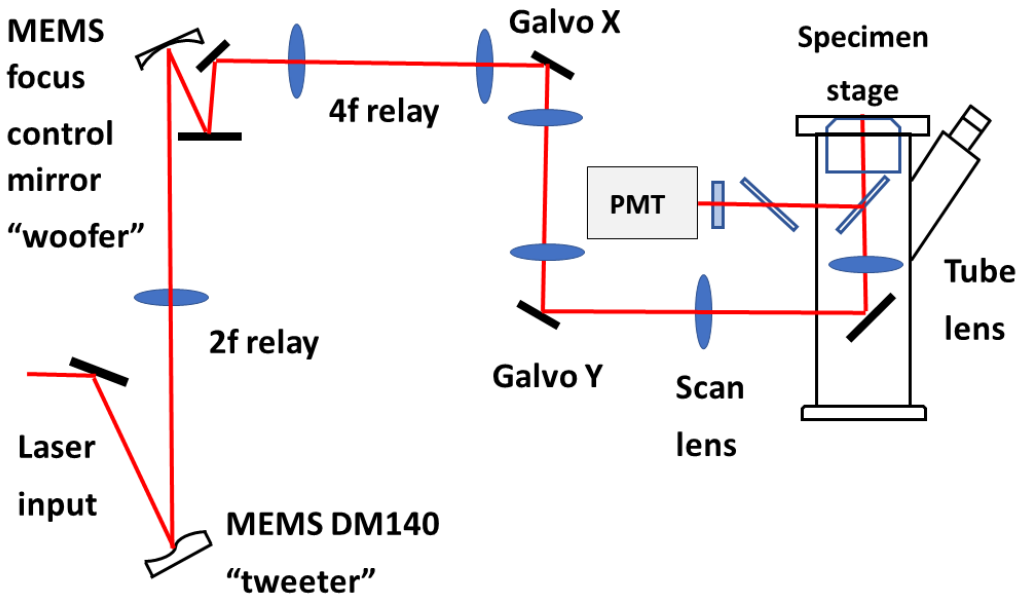

Figure 29. The schematic of the active/adaptive Microscopy. With fast active wavefront modification, both the z-position of the beam focus and local aberration may be continually controlled during beam scanning, enabling oblique or contoured sectioning of the sample. In the diagram it is assumed that the beam scanners and wavefront control mirrors are mutually conjugate to the aperture plane of the objective lens.

The illumination beam is a continuous laser beam from a fiber filtered 635nm diode laser. The beam width is slightly larger than and overfills the aperture of the MEMS DM140 (Boston Micromachines Corp. Multi-DM, 3.5 μm max deflection with 140 actuation channels). This is the "tweeter" that can handle aberrations with higher spatial frequency, including non-axially symmetric modes (for example, astigmatism $Z_{2,2}$ coma $Z_{3,1}$, etc.). The "tweeter" is imaged onto the focus control mirror through a single

lens 2f relay. This is a large-stroke deformable mirror (Revibro Optics MFC mirror, 16 μm max deflection) used for high-speed focus control and correction of depth induced spherical aberration. This mirror, referred to as the “woofer”, is capable of large deflection but low spatial frequencies. The “woofer” and the “tweeter” are the AO module working side by side to maintain a Strehl ratio exceeding 0.8 at any point in the 3D imaging volume. Both the “woofer” and the “tweeter” are imaged onto the imaging galvo scanner mirrors through two 4f relays. Together with a custom designed scan lens and the tube lens in the Nikon microscope stand (Nikon Eclipse TE300, Inverted), the “woofer” and the “tweeter” as well as the Galvo scanners are imaged onto the rear pupil plane of the objective (Nikon CFI APO LWD objective, 1.1NA, 2mm working distance, 380-1050 spectral range). The reflect beam are collected and detected by a pair of photomultiplier tube (PMTs), which is held by a functional block. Although we are currently performing surface reflectance imaging, this imaging platform can easily accommodate multiphoton microscopy by inserting chromatic/fluorescent filters in the functional block or confocal microscopy with installation of a pinhole.

Solidworks Modeling

Zemax is a powerful optical design tool that not only predicts the systematic aberrations but also provides us a platform to optimize the optical system with selection of the proper optical elements, setup the correct separation and alignments between lenses, mirrors, etc., so that the systematic aberration is minimized. These lens data can be directly exported into Excel spread sheet to assist purchases and system setup. In our

case, we use the export lens data and build the exact 1:1 model using off-the-shelf components in Solidoworks. It guides and facilitates the building process of the Active/Adaptive 2-Photon Microscope.

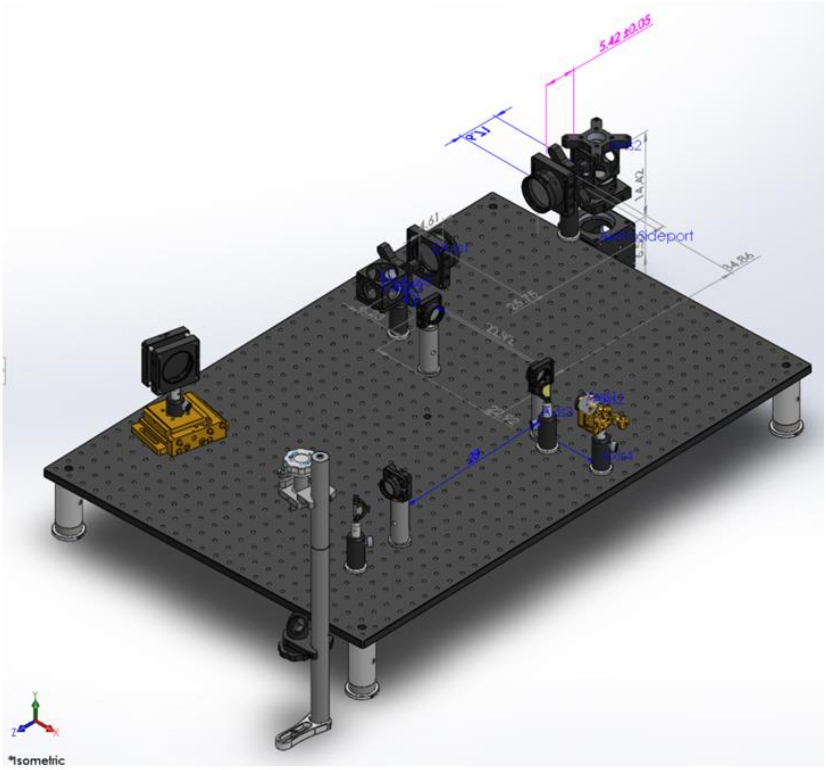

Figure 30. The SolidWorks model of the MEMS DMs, galvo scanner heads, relays with proper alignment and spacing label for the Active/Adaptive 2-Photon Microscope.

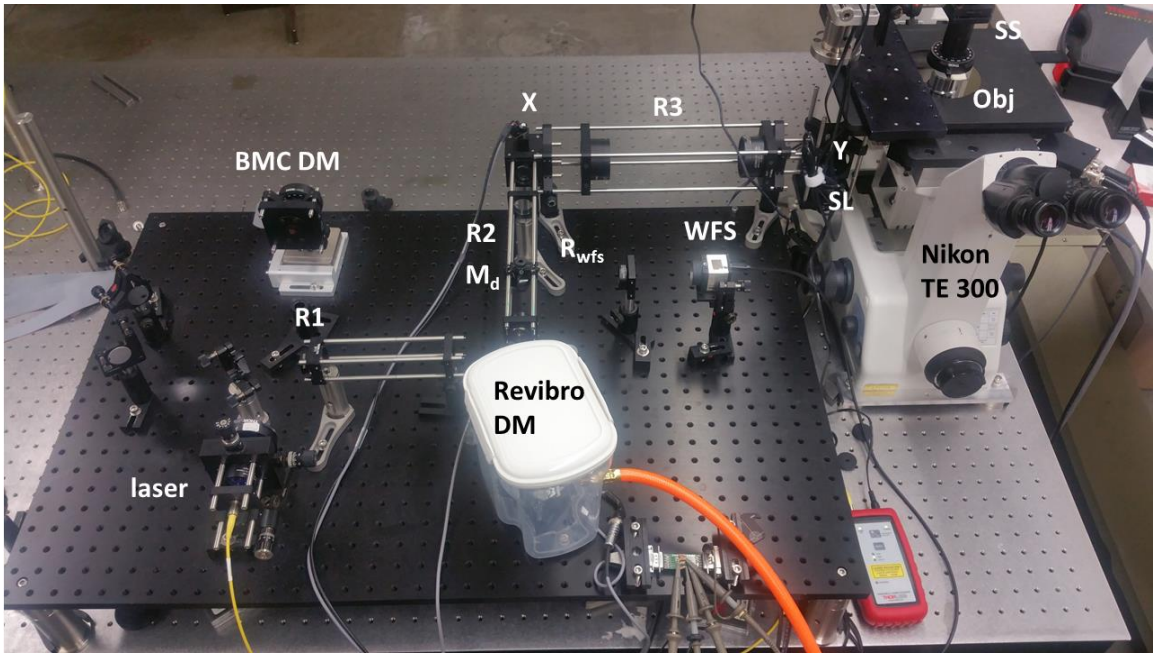

Figure 31. The constructed Active/Adaptive 2-Photon Microscope. A fiber filter laser source illuminates the BMC DM. The BMC DM is imaged onto Revibro DM through a single lens relay (R1). The Revibro DM is imaged onto X galvo through a 4f relay (R2). A detachable mirror (M_d) is used to steer the beam from the imaging path to the wavefront sensor. Both BMC DM and Revibro DM are imaged onto the WFS through a 4f relay (R2). X galvo is imaged onto Y galvo through a 2 inch 4f relay (R3). Y galvo is then image onto the back focal plane of the objective (obj) through a relay consists of a scan lens (SL) and tube lens inside the Nikon TE 300. A sample stage (SS) is mounted on a motorized x-y-z translation stage. More detailed images and descriptions can be found in the Appendix.

SCANNERS AND MEMS DM CONTROL AND IMAGING SOFTWARE DEVELOPMENT

The software for controlling all the scanners and MEMS DMs was built on basic open-source imaging software Scanimage (SI) provided by Vidrio Technologies, LLC. Four PCIe cards from National Instruments (NI) provided the digital/analog output and analog-to-digital conversion for the image signal from the PMTs. Using the Object-Oriented Programming under Matlab environment, we developed 4 channels of analog voltages output to drive the 4-zone Revibro DM. On the other hand, a single channel of digital logic output was created to provide the trigger signal to change shapes on the BMC DM, which step through a preprogrammed shape trajectory. All these analog output and digital output voltages were properly synced with the movement of the galvo-scanners and image acquisition, which ensured the desired wavefront maps were created at the right time and location during active scanning and intra-scan aberration correction.

Software/Hardware Interface

The software for controlling the Revibro DM, BMC DM and PMTs was developed at the Montana State University. The overall architecture for the software/hardware interface is shown in Figure 32.

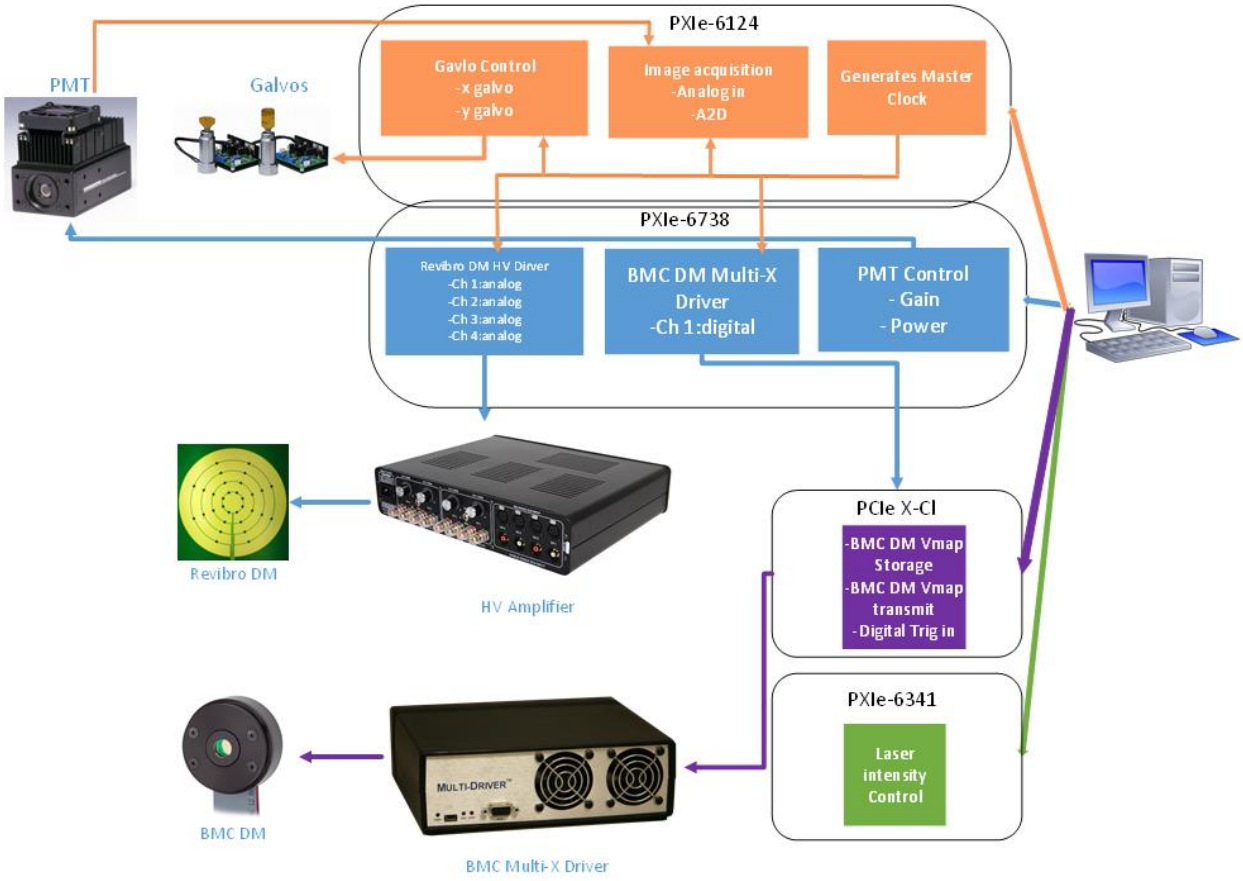

Figure 32. The architecture of the control interface for the active/adaptive laser scanning microscope.

Three PXIe cards were used for the hardware/software interface: 1) PXIe-6124 (Texas Instruments, Multifunction I/O module), 2) PXIe-6738 (Texas Instruments, Analog/Digital Output Module) and 3) PXIe-6341 (Texas Instruments, Multifunction I/O module). As shown in the orange function blocks in Figure 32, the SI software provided the functionalities including driving signals for the galvo scanners and digitization of the analog signal from the PMTs to form each frame of the image. A master clock, frame trigger, was generated for synchronization of all the MEMS DMs, galvo scanners and

data acquisition. All the signal processing of the built-in functionalities from SI are carried on the PXIe-6124.

As shown in blue in Figure 32, all the custom functionalities developed at the Montana State University were carried out on the PXIe-6738. A four-channel analog signal was created to drive the Revibro DM to create desired defocus($Z_{2,0}$), primary spherical $(Z_{4,0})$ and secondary spherical aberrations ($Z_{6,0}$). This analog signal was synchronized to the movement of the galvo scanners through the master clock from PXIe-6124. A single channel LVTTL was also created on the PXIe-6738. Synchronized to the movement of the galvo scanners, this digital signal provided the trigger to the PXIe X-CL to update the mirror shape on the BMC DM.

As shown in purple in Figure 32, one additional PCIe X-CL card (Matrox Solios Camera Link frame grabber) was used to interface with the BMC multi-X driver. It sent a 12×12 matrix of digital numbers to the BMC Multi-driver and maps it onto the address of the 12×12 electrodes. The BMC multi-driver received the digital numbers and address of the electrodes through a mini (HDR) camera link cable from the PCI X-CL interface card. These digital numbers were then converted into 12×12 voltages and applied on the actuators under the membrane of the BMC Multi-DM to form the desired wavefront. More importantly, it was also designated for storing the voltage maps for controlling the BMC DM. A 50-ohm SMA+SMB connector was on board to take in LVTTL digital input for updating a new voltage map onto the BMC DM. This is a crucial feature for dynamic aberration correction. We created a synchronized LVTTL digital signal to the galvo scanners using the PXIe-6738 (labeled as BMC Multi-X driver- Ch1:digital). This

LVTTL digital signal triggered the PCI X-CL interface card to pass on the pre-stored voltage map to the BMC Multi-X driver, so that the desired wavefront map was put onto the DM at the right time and location as the laser beam scans across the field of view.

Our active/adaptive microscope is a platform designed to accommodate multi-photon microscopy. Hence, a laser beam power controller is necessary. The PXIe-6341 (shown in green in Figure 32) is reserved to provide control signal to adjust the optical power of a mode-locked femtosecond pulse laser through a Pockels cells modulator. This feature is currently under development.

Synchronization

To synchronize both Revibro DM (woofer) and BMC DM (tweeter) to the movement of the fast galvo, there needs to be a master clock that triggers the events for all galvos, woofer, tweeter and the data acquisition, etc. Ideally, a line trigger that generates a positive rising edge at the beginning of each line scan will easily function as a master clock. It will easily allow the subsequent trigger signals for the woofer and tweeter to be synchronize with the movement of the fast galvo. In this case, the woofer and tweeter can produce the desired wavefront at right time and right location of each line scan and waits for the next line scan to start. There are two types of triggers exported from the imaging software (Scanimage, Vidrio Technologies, LLC): Line Trigger when resonant mirrors are used and Frame Trigger for galvo mirrors. Since there was no line triggering signal available for galvo scanners, the frame triggering signal was used to synchronize the deformable mirrors to the movement of the galvo scanners.

Unfortunately, there was no line trigger available from the SI software for the Gavlo scanners we are using. The imaging software generates a triggering signal (TTL edge) at the beginning of each frame. After a GRAB or LOOP is initiated from the Main Controls panel, this triggering signal starts the galvo scanners and data acquisition for each pixel in a single frame of an image. As shown in Figure 32, it was generated on the programmable functioning interface on the PXIe 6124. This frame trigger signal was internally wired through the chassis that holds all the PXIe cards. In this case, no external cables were required so that both electronic noise and jitter can be minimized.

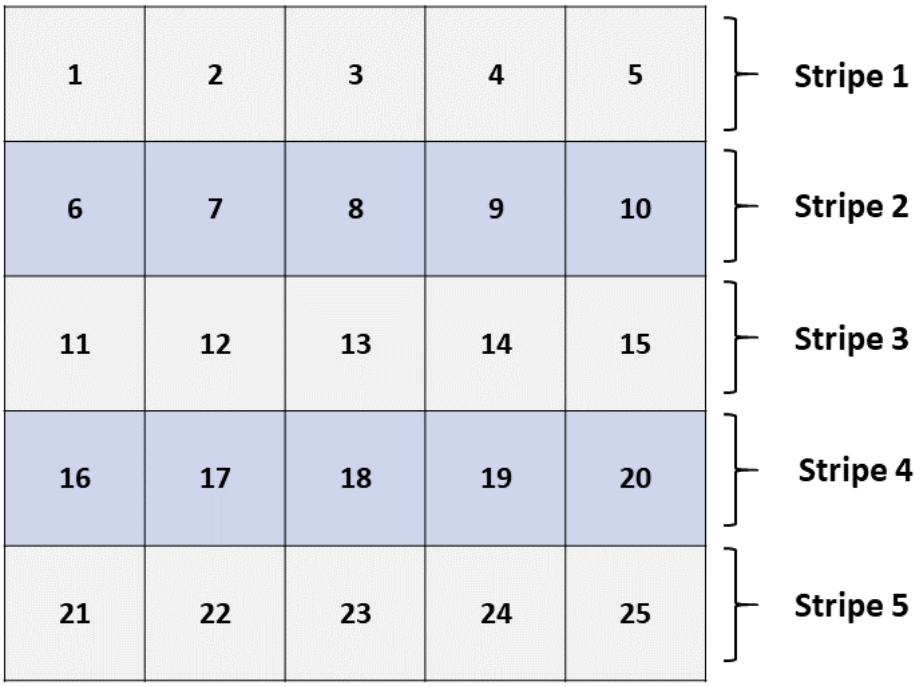

Figure 33. The 25 sub-regions of each single frame of an image. During image acquisition, the single image frame is divided into 5 stripes. Each stripe is then sub-divided into 5 zones. Consequently, there are 25 sub-regions in each single frame of image. Each sub-region is having a unique wavefront map of its own for correcting the local wavefront aberrations.

Each single frame of an image was divided into a 5×5 grid as show in Figure 33. Each of these 25 zones had a unique wavefront map designated for the aberration correction in this sub-region of the image/field of view. Generally, there are 500 data points per line and 500 lines per frame, which indicates each sub-region of the image consists of 100 lines with 100 points per line.

The more sub-regions there are in each single frame of the image indicates that each wavefront map corrects a smaller region that allows less spatial aberration variations. Consequently, better image quality could be obtained. The most ideal case would be to use a variable, point-by-point correction as microscope scans across the specimen. On the other hand, more numerous, smaller zones might be good for imaging, but require longer training times. As we are currently limited by the buffer size of the PCI X-CL, we settled for a 5×5 grid. The 5×5 grid turns out to be a reasonable compromise for full-frame "training" to find the best aberration correction wavefront maps. We adopted the same 5×5 grid for training Revibro DM and interpolate to make smoother transition for the focus adjustment and spherical aberration trajectories. Nonetheless, the number of sub-regions can be easily increased as new versions of BMC Multi-X driver with larger buffer size are under development.

Tweeter/BMC Multi-DM. After collecting the total 25 unique wavefront maps for each of the 25 zones, they are uploaded into the memory/buffer of the BMC Multi-X driver. The maximum number of data points for this driver is 65000 or 468 wavefront maps for the 140-channel Multi-DM. The sequencing hardware is then enabled and

awaits the TTL triggering signal to load the wavefront maps onto the MEMS DM. The synchronization setup is shown as in

Figure 34. A LVTTL signal for updating the wavefront maps on the BMC DM is generated through a digital I/O port on the PXIe card (NI PXIe-6738). The arbitrary waveform (BMC TTL) is designed in Matlab and then loaded into the buffer of the PXIe card awaits the frame trigger to start the output.

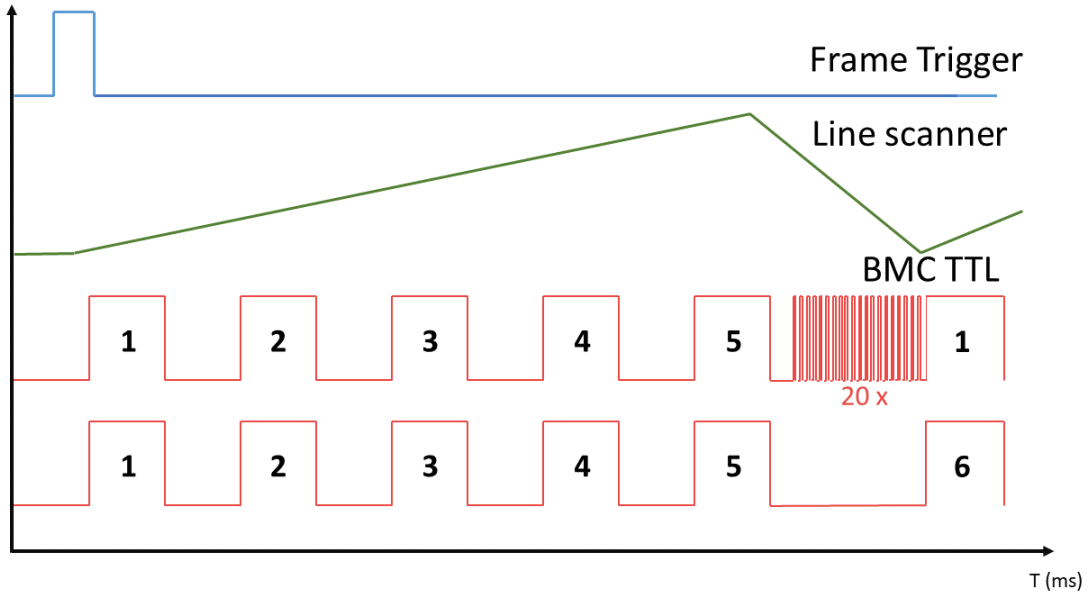

Figure 34. Triggering signals for the BMC DM. The blue TTL signal is the master clock generated at the beginning of each frame. The blue analog signal is the driving voltage signal for the fast galvo scanner. The upper BMC TTL signal in red is the trigger for the BMC DM to update a new wavefront map during each line scan. The lower BMC TTL signal in red is the same trigger for the BMC DM at every 100th line.

As shown in Figure 34, the upper red line BMC TTL is the triggering signal for the Multi-X driver. At the very beginning of image acquisition, the Frame Trigger starts the Line scanner and the BMC TTL. Five pulses are evenly spaced to trigger the first five wavefront maps during the forward scan of the line scanner. Twenty pulses quickly flush

the rest of the twenty frames of the twenty-five wavefront maps stored in the Multi-X driver during the retrace of the line scanner. As a result, the first five wavefront maps will be put on the BMC DM again when the line scanner return to the zone 1 to collect the second line of the image. After collecting 100 lines of the image, it reaches the end of the stripe 1. The next five wavefront maps are numbered from 6 to 10. In this case (for line 100), the twenty fast pulses are replaced with a logic low to wait for the forward scan of the next line. This version of the BMC clock signal is shown as the lower red line in Figure 34.

The BMC TTL signal is created with the NI PXIe-6738 digital I/O. The data points for the arbitrary waveform contain the regular five triggering pulses and the twenty fast pulses during the retrace. All the data of the BMC TTL signal for the 500-line full frame image are pre-designed in Matlab and uploaded to the memory of the PXIe card. A constant sampling frequency is set and it starts clocking through all the data points of the arbitrary waveform after receiving the frame trigger. Since the digital output channel can only operate at a constant sampling frequency, the difference between a regular triggering pulse and the twenty fast pulses during the retrace is number of points. Each regular pulse consists of 184 data points (92 points for logic 1 and 92 points for logic 0), whileeach fast pulse contains 4 data points (2 points for logic 1 and 2 points for logic 0). There are totally 1000 data points per line and 500,000 data points for a 500-line frame. Knowing the total number of data points per frame N and frame rate f of 1.1Hz, the sample rate is calculated as below.

$$Sample\ Rate = N\ \times f = 500{,}000\ \times 1.1 = 550kHz$$

Woofer/Revibro DM. The case for Revibro DM is quite a bit different from the triggering setup for BMC DM. The Revibro DM is working entirely in analog and the memory is large enough so that the total number of data points is not a concern for the driving signal.

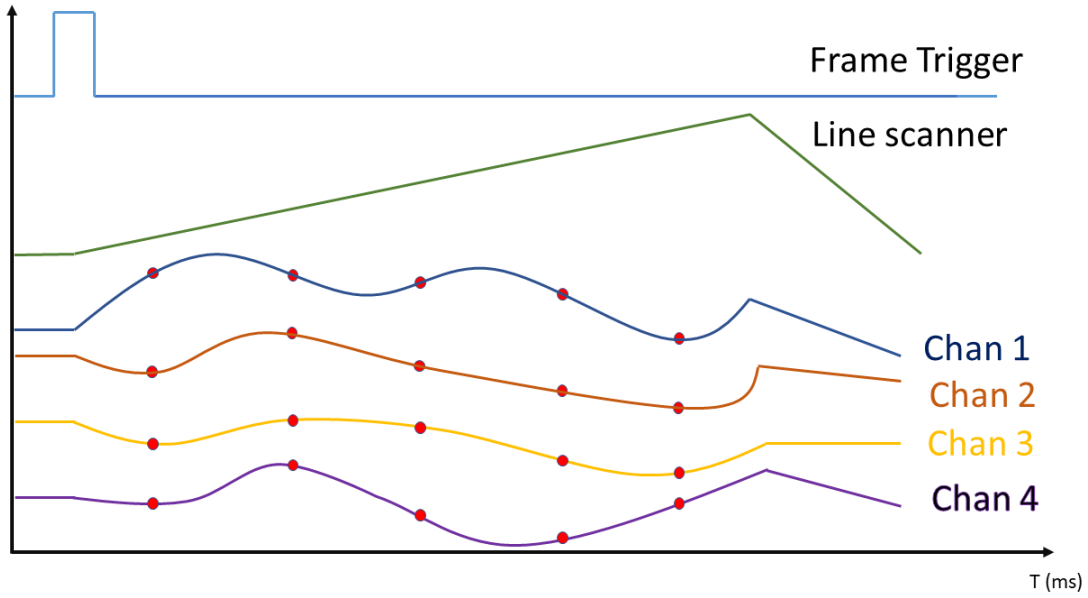

Figure 35. Driving signals for the 4 channel Revibro DM. The blue TTL signal is the master clock generated at the beginning of each frame. The blue analog signal is the driving voltage signal for the fast galvo scanner. The analog signal in blue, orange, yellow and purple are the driving signal for the 4 electrodes on the Revibro DM respectively. These four driving signals are interpolated from the actual trained voltage date shown in red dots on each line.

As shown in Figure 35, the five wavefront map/voltage map during a line scan are interpolated with 100 data points for each channel. The total number of the data points for the four-channel device in a 500-line frame is 200,000 or 50,000 data points for each channel. The sample rate for the same 1.1Hz frame rate is then calculated as below.

$$Sample\ Rate = N \times f = 50{,}000 \times 1.1 = 55k\ Hz$$

ACTIVE SCANNING WITH DYNAMIC ABERRATION CORRECTION

Sensorless Aberration Measurement and Correction

A conventional adaptive optics system employs a wavefront detection module such as a Shack-Hartmann wavefront sensor (WFS) to measure the wavefront of the back-scattered light from excitation. This measured wavefront guides the adaptive elements such as a deformable mirror to form a feedback control system for a closed loop aberration correction in real time. It is an effective approach in many applications. However, this type of direct wavefront sensing could be of great difficulty for 2PM. Tao et al [47] demonstrated direct wavefront sensing with a fluorescence confocal microscope. They incorporated a solid-state laser (λ = 515nm) to excite yellow fluorescent proteins for imaging in addition to the He-Ne laser (λ = 633nm) used for excitation of the fluorescent reference beacons for direct wavefront sensing. The WFS was placed in a conjugate plane as the photomultiplier so that the optimizing the reflected light from the solid-state laser results in an improved image quality [57]. A similar technique for direct wavefront sensing using a spectrally distinct fluorescent bead as a guide star was used for widefield fluorescence microscopy [58], and direct backscattered light with a pinhole filter in front of a Shack-Hartmann sensor was used for direct wavefront sensing for adaptive confocal microscopy [59]. However, the double-pass effect made these measurements with a WFS weakly sensitive to odd aberration. This type of direct wavefront measurement detects the reflected light that passes the same optics twice (referred to as ‘double-pass’). As a result, antisymmetric aberrations

(aberrations suffering a sign change upon inversion about the origin, corresponding to odd values of Zernike azimuth index *m*) such as coma could be canceled by the second pass through the same optical elements [60].

The photons collected for imaging from a 2PM is such a weak optical signal that barely any photons can be shared for wavefront sensing. A CCD-camera-based wavefront sensor can hardly detect this signal, which makes the wavefront reconstruction inaccurate. Even if there is sufficient back scattered light for wavefront sensing, it is very difficult to exclude the light reflect from the out-of-focus layers in the imaging sample [61]. Moreover, the PMTs are mounted directly behind the objective, so there is physically very limited space for a wavefront sensor to be implemented into a 2PM. Consequently, we decided to implement the sensorless wavefront optimization.

Image-based sensorless wavefront optimization can be a great choice for multi-photon microscopy for biological imaging. Generally, the feedback for sensorless wavefront optimization is the loss of contrast in the output images, instead of the directly measured wavefront data with a WFS. Debarre et al [11] have shown that an image-based adaptive optics could significantly improve the resolution and signal strength for two-photon excitation fluorescence microscopy when imaging at a depth of 50 μm in a mouse embryo [62]. Bueno et al [63] used both adaptive lens and liquid-crystal-on-silicon spatial light modulator to compensate the aberrations presence at a depth of 100μm in the specimen. With a hill-climbing algorithm and a metric for image sharpness, the imaging results showed a significant improvement in image quality [63].

The sensorless wavefront optimization is usually through iterative training in a closed-loop feedback to improve a measurable parameter in the image such as image brightness, sharpness or contrast. Many optimization algorithms such as the hill-climbing algorithm, gradient descent and genetic algorithms are widely used. Moreover, the aberrations in the optical systems can be decomposed into the orthogonal Zernike modes. For small aberrations, the Strehl intensity of a wavefront directly depends on the variance $\emptyset$ of the wavefront, which is the sum of the variance of all the orthogonal Zernike modes of the aberration present in the optical system [64]. All the Zernike modes of the aberration can be represented by the amplitude a_i of the ith normalized Zernike polynomial Z_i, in which case the variance of each mode is just a_i^2 and the overall variance is

$$\text{Equation 19. } \emptyset = \sum_i a_i^2$$

and the Strehl intensity can be expressed as

$$\text{Equation 20. } S \approx 1 - \sum_i a_i^2$$

Any aberration can be considered as a summation of Zernike aberration modes. By applying different Zernike mode with the MEMS DM sequentially and iteratively, an optimum correction can be achieved. The highest Strehl could lead to improvement in both contrast and brightness, which are the feedback information that can be measured from images.

Sensorless wavefront optimization has been proven effective in many imaging systems such as confocal microscope and ophthalmoscopes [65] [7]. The static mirror shapes on both woofer and tweeter we have trained so far are all represented by Zernike

modal shapes. Therefore, we have chosen the image-based sensorless wavefront optimization with hill-climbing optimization algorithms.

Image-based wavefront sensorless adaptive optics modal optimization algorithm

The optimization process was initialized with selection of a region of interest (ROI) of the 3D imaging volume. Two merit functions can be used here to either optimize image brightness or contrast. The brightness optimization is reserved for the case when the signal strength from ballistic photons are weak. On the other hand, merit function of contrast is better suitable for reflected light imaging of biological samples to bring out finer features. Difference in the index of refraction between neighboring features in biological samples can be very small. For instance, the refractive index of the three layers of the fish cornea, epithelium and stroma I and II, are measured to be around 1.446, 1.345 and 1.392 [66]. Optimizing the image brightness could bring up noise floor and further obscure feature of interest. Consequently, algorithms for both image brightness and contrast are developed and implemented in our AO module.

The contrast (Michelson contrast) is calculated by finding the top ten brightest and dimmest pixels near the ROI for each of the twenty-five Zernike modes. The maximum brightness B_{max} and minimum brightness B_{min} are found by summing up the top 10 brightest and dimmest pixels respectively. The contrast is calculated by dividing the difference of maximum brightness B_{max} and minimum brightness B_{min} values by the sum.

Equation 21. $C = \frac{B_{max} - B_{min}}{B_{max} + B_{min}}$

For some imaging targets such as the 1μm holes negative target presented in the Figure 47 , we implement a merit function for both brightness and contrast. It not only allows us to enhance the contrast of the image, but also keep the focus on the most reflective aluminum surface. The merit function can be expressed as follows.

Equation 22. $M = \alpha \times B_{max} + \beta \times C$

The α and β are the weights of optimizing B_{max} and C respectively. With both woofer (Revibro DM) and tweeter (BMC multi-DM) working side by side, our woofer and tweeter configuration can produce over 25 modal shapes of amplitude range from -2000nm to +2000nm (wavefront) , which corresponds to each Zernike polynomial up to the 6th order in Zernike expansion.

During the optimization process, each Zernike mode is evaluated independently due to the orthogonality of the Zernike polynomials. For each Zernike mode, a step size of a positive delta value and a negative delta value of equal amplitude is applied sequentially onto the DMs. The values of the merit function are recorded and compared to the baseline value. These three values for each Zernike mode are fitted with a 2nd order polynomial and the optimum amplitude for each Zernike mode is found from the fitted curve. This newly found amplitude for each Zernike mode is converted into voltage maps which are superimposed and applied on the woofer and tweeter. A new baseline value of the merit function is calculated and the optimization algorithm advances to the next iteration. Here, a smaller step size of a positive delta value and a negative delta value of equal amplitude relative to the new baseline is applied onto the DMs. Then a curve-fit is performed for the values of the merit function at the baseline, baseline with a positive delta and baseline with negative delta. A new baseline amplitude is found from the curve-

fitting for each Zernike mode. For the case that there is no improvement in image quality for a particular Zernike mode, the delta amplitude is set to zero. This optimization process takes usually 3-4 iterations to fully correct the primary, secondary spherical aberrations and the off-axis aberrations. The algorithm controls the maximum number of iterations. After the reaching the limit, the algorithm finds the best amplitude for each Zernike mode that produced the best result, and combine them to form a final shape on the DMs. A fully corrected image is then acquired and the optimization algorithm is terminated.

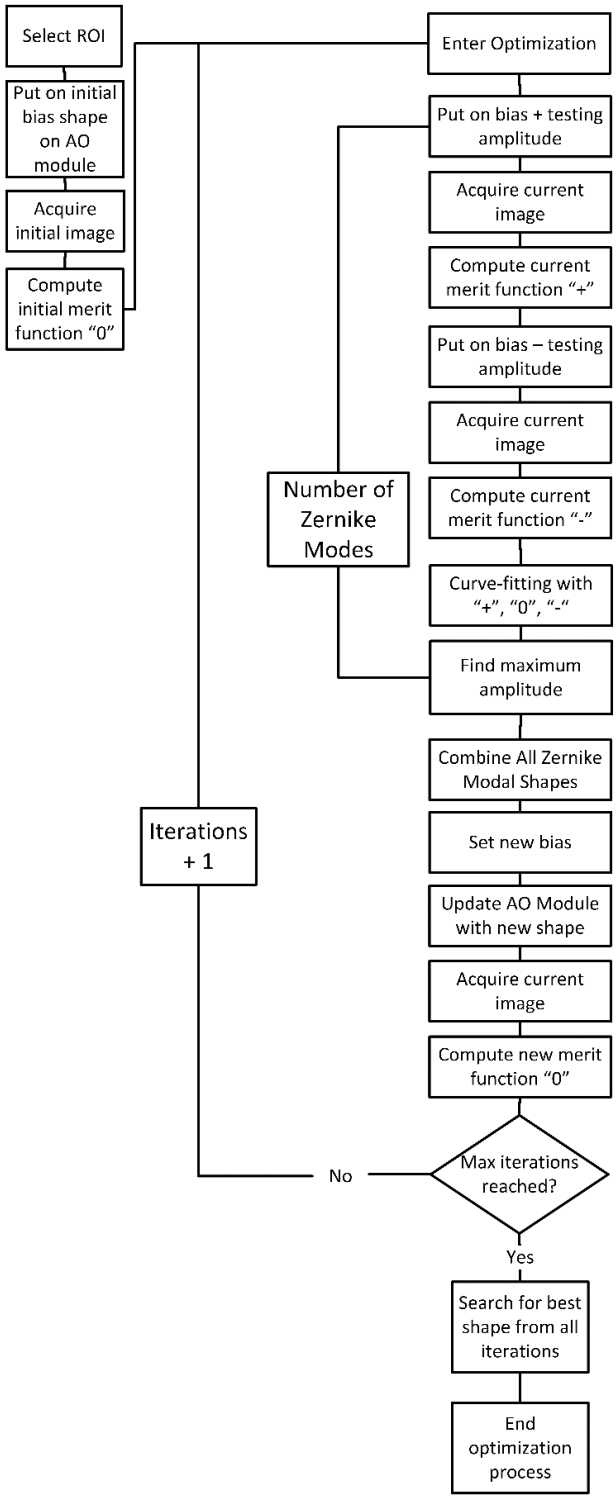

Figure 36. Flowchart for the image based sensorless optimization

Dynamic off-axis aberration training during active scanning. To speed up the optimization process, image data from all twenty-five zones are processed simultaneously. The tester wavefront maps are preloaded into the BMC X-driver. These twenty-five zonal wavefront maps are synced with the movement of the galvo-scanners and put on the BMC DM at the right time and in the right location of the image.

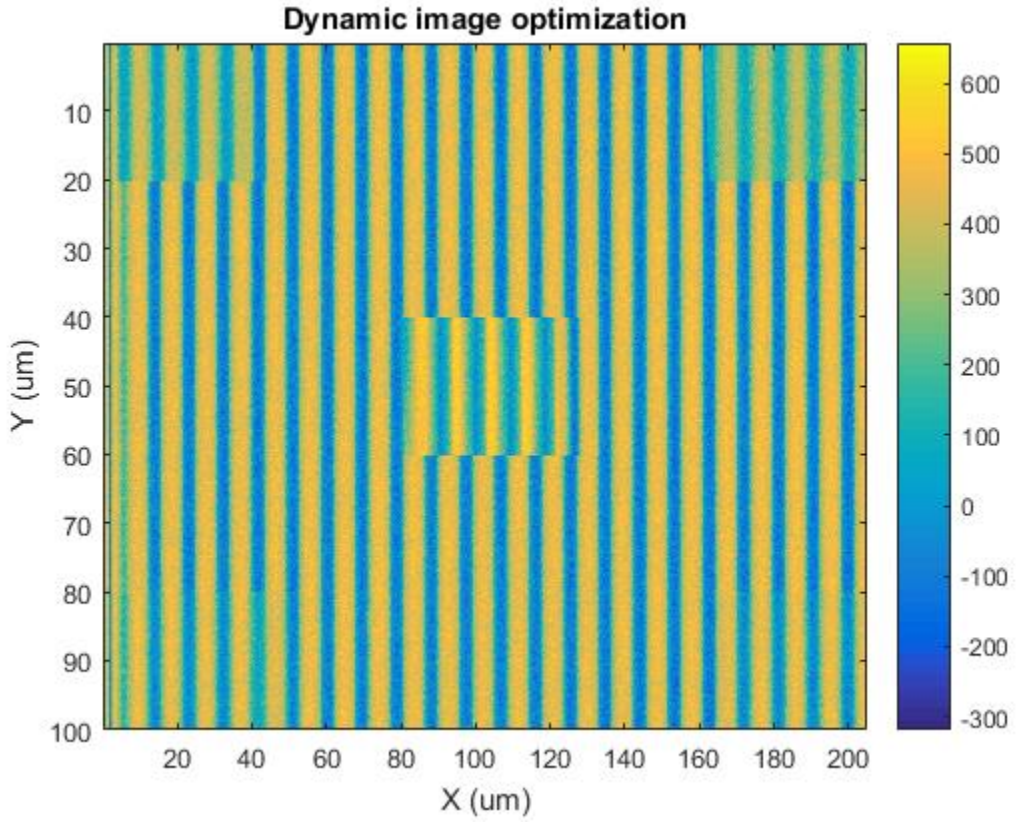

Figure 37. A demonstration of dynamic off-axis aberration training with BMC DM.

As an example (shown in Figure 37), the wavefront maps on the BMC DM are 400nm of Astigmatism and Coma at four corner zones of the image while 800nm of Trefoil in the center of the image. The frame rate for this image acquired is at 1.1Hz. The blurred zonal pattern demonstrates the capability of dynamic correction that our AO

system can put on desired wavefront map at any location of the image during active scanning during image acquisition. It allows us to correct any off-axis aberration within each of the 25 sub-regions with a unique set of wavefront maps individually. Traditional static aberration correction, for which one wavefront map is used for the entire image, may not optimally correct the aberrations throughout the field of view, especially when the image surface is a more convoluted surface with multiple-depth within a single frame of image. The dynamic aberration correction immediately stands out as it sub-divides the entire image into 25 individual zones and address the aberrations in each zone individually without sacrificing the speed of image acquisition. So far, we are able to sub-divide the entire image into 25 zones due to the buffer size of the Multi-X driver of the BMC DM. As the buffer size increases in the future release, this 25-zone approach can easily be further increased to hundreds of sub-regions and eventually correct each single pixel to maintain a diffraction limited imaging for even more complex biological surfaces.

Dynamic vs static aberration correction with targets. The most significant contribution of this project is that our active and adaptive optical system is the first ever imaging platform capable of aberration-corrected beam scanning and tracking irregular surface throughout a three-dimensional volume.

Ideally, point-by-point aberration correction should be made as the microscope scans across the specimen. However, there is a concern on current bandwidth of the AO elements. Our previous investigation has shown that both woofer and tweeter in our AO module will be able to keep up with a galvo scanner at around 1kHz. The practical

limitation we have faced so far is actually not bandwidth of the BMC Multi-DM, but the limited number of frames that can be stored during image acquisition.

Nonetheless, we were able to divide the full frame image is into twenty-five sub-regions, and each region has a unique wavefront map consisting of defocus ($\tilde{Z}_{2,0}$), primary spherical ($\tilde{Z}_{4,0}$), secondary spherical ($\tilde{Z}_{6,0}$), astigmatism ($\tilde{Z}_{2,-2}$), coma ($\tilde{Z}_{3,1}$), trefoil ($\tilde{Z}_{3,3}$) and higher order off-axis aberrations up to 6th order of Zernike polynomials. In this way, region-by-region aberration correction is performed to address spatial variations in the wavefront aberration. It should be a refinement of single prescription, full frame static aberration correction.

As an example, Figure 38 demonstrates the tiling of the image. In this case, each zone is having a unique amplitude of astigmatism. The fast scan is in the x direction and the slow scan is in the y direction. At 500Hz fast scan, the higher order wavefront such as astigmatism is updating over 3kHz in this case to keep up with the fast scan mirror during each forward line scan. All these twenty-five frames of voltage maps are determined during the training and loaded into the buffer of the BMC X-driver, and the PXIe card that creates the analog output that drives the Revibro DM.

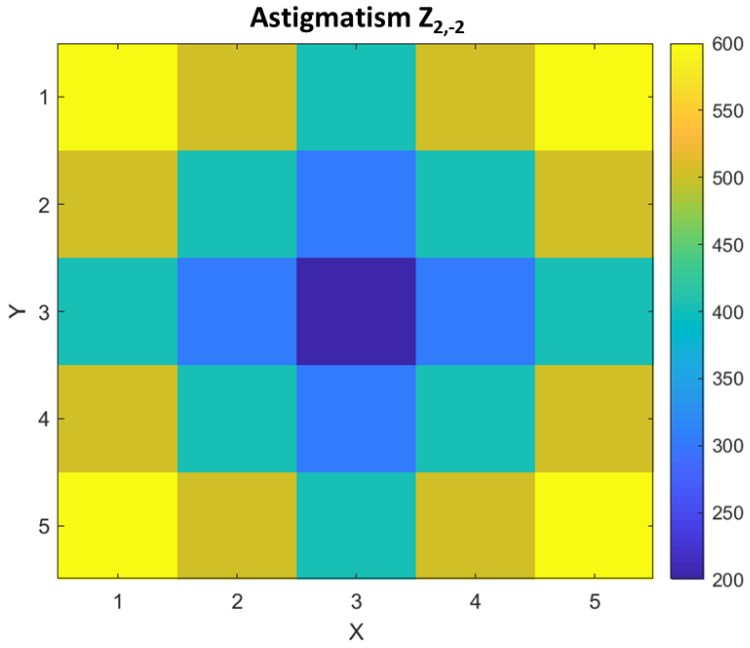

Figure 38. The 25 sub-regions of a single frame image.

Imaging with sub-micron features. Static aberration correction is performed on a sub-wavelength target to validate our AO operation and evaluate the maximum achievable spatial resolution of our active/adaptive microscope. The submicron target has aluminum features deposited on glasses substrate, which is created using e-beam lithography with a liftoff process (Thanks to Dr. Wataru Nakagawa's group for providing this submicron target).

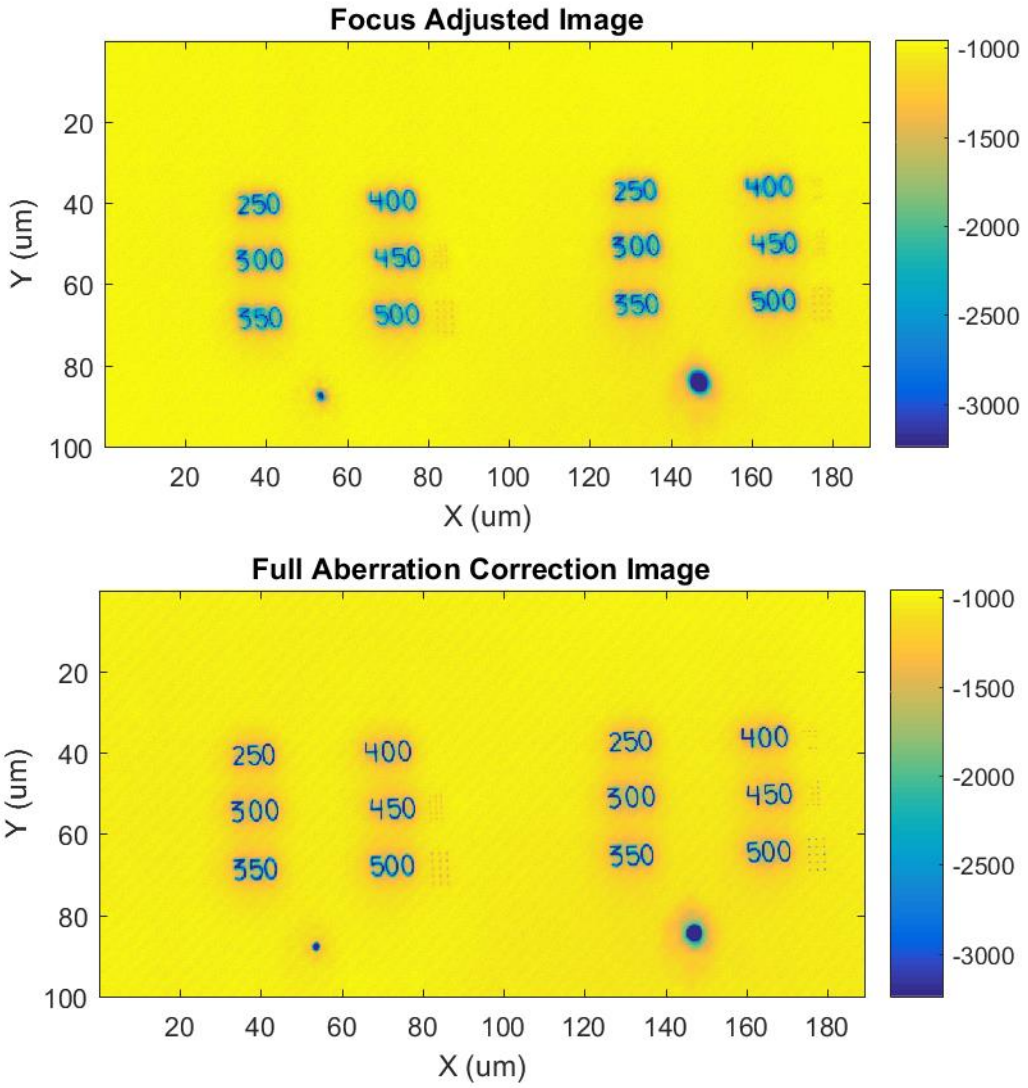

Figure 39. The sub-wavelength resolution target (upper) before aberration correction and (lower) after spherical and off-axis aberration being corrected near the edge.

As shown in Figure 39, two 5×3 groups of 500nm imaging targets located near the center and right edge of the field of view are chosen to perform aberration correction on. The region of interest for the training shown in Figure 39 is the group of submicron target disk of 500nm in diameter located in the right-hand side of the image. After focus adjustment, the features are still blurred due to the spherical aberration and off-axis aberrations such as astigmatism and coma present in the image. We performed sensorless

wavefront optimization using image contrast as the merit function. A total of 8 iterations of optimization were performed and the best result was obtained from the 4th iteration, giving a maximum contrast of 0.68. The resulting wavefront map consists of a superposition of Zernike modes with the amplitudes given in Table 8. The result, shown in Figure 39(lower), is that the sensorless wavefront optimization significantly improved not only the contrast of the image but also the brightness of the submicron features.

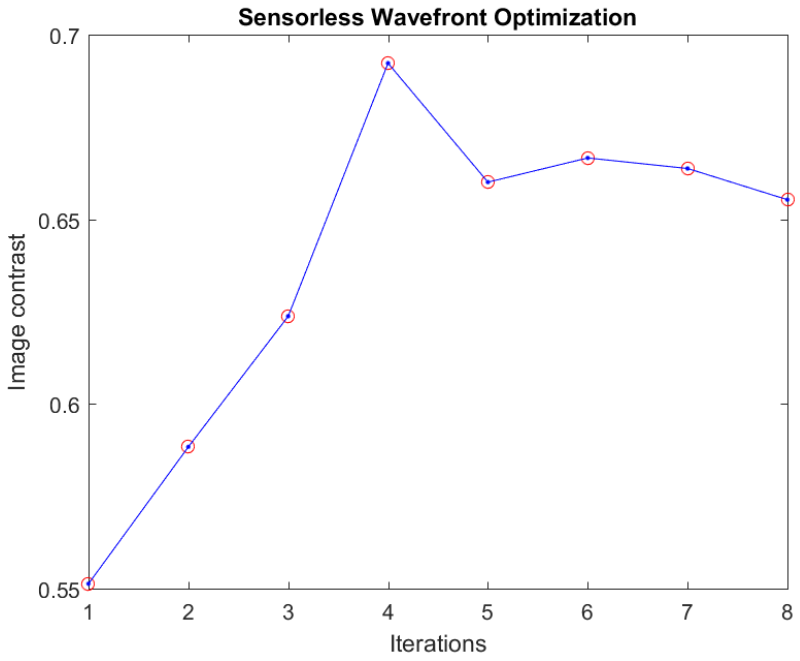

Figure 40. The contrast of the submicron features in the region of interest after each iteration of sensorless image optimization.

Table 8. The Zernike coefficients for the correction wavefront map used in Figure 39.

	Spherical Aberration		Astigmatism		Coma	
	$Z_{4,0}$	$Z_{6,0}$	$Z_{2,-2}$	$Z_{2,2}$	$Z_{3,-1}$	$Z_{3,1}$
Amplitude (nm)	-47	41	68	0	-114	0

More quantitative results can be obtained by evaluating the point spread function of the sub-wavelength target disks. The spatial resolution of the objective can be determined by the radius of the central disk of the Airy diffraction pattern. The Airy pattern radius from the central peak to the first minimum is governed by

$$\text{Equation 23. } r = \frac{1.22\lambda}{2NA}$$

where r is the radius of the central disk, λ is the wavelength of incident beam (635nm), and the NA is the numerical aperture of the objective. The objective being used in our microscope is a Nikon CFI Apo LWD 25X objective, which features a wide field of view and a long working distance with designed NA of 1.1. To calculate the effective NA, we measured both the illumination beam width and the size of the back aperture. The back aperture of the Nikon objective is measured to be 1.76cm in diameter. As the incident beam overfills the MEMS DMs, a circular stop on the Revibro DM is introduced to filter out the unwanted photons coming from the illumination outside the defined Zernike circle. Due to the fact the incident beam comes in at a small angle ($<5^o$) onto the Revibro DM, laser beam after the circular stop turns into an oblong shape. The oblong shaped illumination beam measured at the back focal plane of the objective is 1.2cm in the x direction and 1.4cm in the y direction. We take the averaged beam diameter of 1.3cm, which gives the effective NA as

$$NA = \frac{1.3}{1.76} * 1.1 = 0.8$$

Therefore, the image resolution is found by calculating the diameter of the Airy disk,

$$D = 2r = \frac{1.22\lambda}{NA} = 0.97m$$

and the airy function can be found using the effective NA of the objective and Bessel function of the 1st kind.

Equation 24. $u(r) = \frac{2J_1(k \times NA \times r)}{k \times NA \times r}$

Equation 25. $I(r) = |u(r)|^2$

where the wavenumber $k = \frac{2\pi}{\lambda}$ and the radial coordinate of the airy function $r = \sqrt{x^2 + y^2}$.

The PSF can be found by 2D convolving the airy function I(r) with a pillbox function rect(r/r_0) representing the 500nm dot. r_0 is 250nm here.

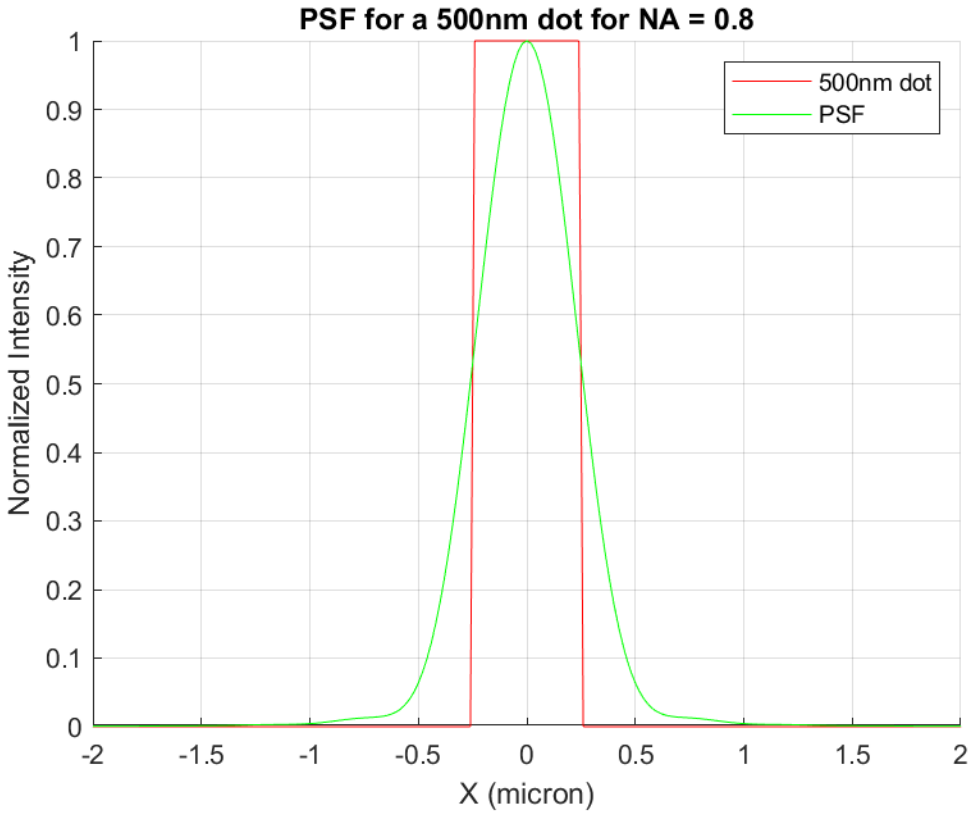

Figure 41. The aberration free PSF of a 500nm

The cross section of the aberration-free PSF for our active/adaptive microscope is plotted in Figure 41. The full width half maximum (FWHM) for the ideal PSF is 0.5μm. The measured PSF for the same 500nm target disk located in the center and near the edge as shown in the Figure 39 are plotted in Figure 42. Separate optimization was performed for each of these regions of interest.

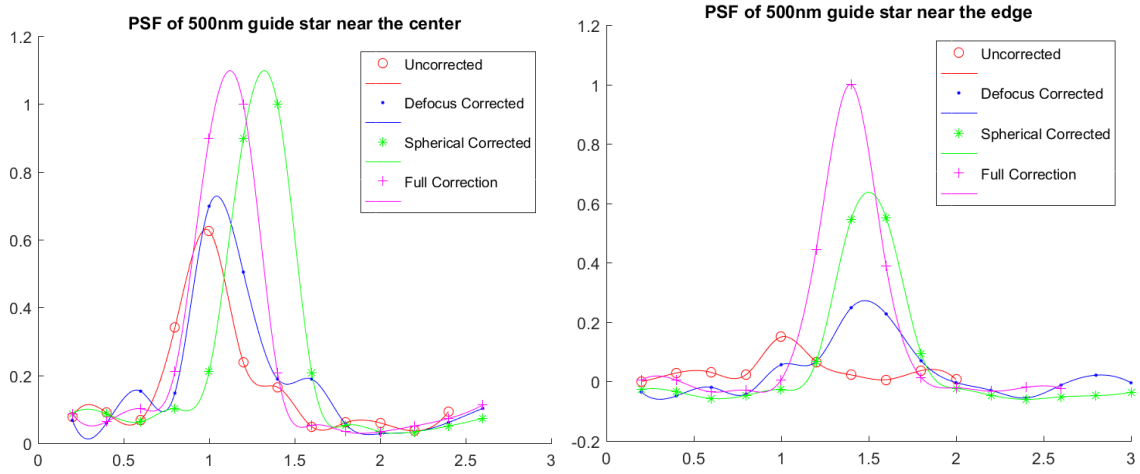

Figure 42. The improvement in PSF of the 500nm disk near (left) the center and (right) the edge. These PSFs are obtained from a line profile of a target disk located in the center and near the edge of the image shown in Figure 39. The markers are the actual normalized pixel value and the solid line is from a cubic spline interpolation.

The peak intensity of the 500nm disk in the center shows a significant improvement after primary spherical and secondary spherical aberrations are corrected. The peak intensity increases by nearly 40%. As there is minimum off-axis aberration present in the center of the FOV, the fully corrected PSF shows nearly identical characteristics as the case after correction for primary and secondary spherical aberrations. The measured FWHM for the PSF is 500nm, which is the same as the ideal PSF as the previous calculation. On the other hand, the improvement is even more dramatic for the targets near the edge due to the larger amplitude of coma and astigmatism at the maximum FOV. The peak intensity increases more than 40% after the spherical aberration is corrected. An additional 40% increment is shown after off-axis aberrations have been corrected. The FWHM here is near the theoretical value of 500nm after both spherical and off-axis aberration correction.

Fast focus control with primary and secondary spherical aberration correction. To demonstrate we are capable of imaging a tilted plane within the focus range of the Revibro MEMS DM in a single frame, we imaged a target with periodic lines and spaces, with the target tilted in both x and y axes. Without active scanning, the LSM can only resolve the region on the target that is in focus, which is the lower right corner of the grating as shown in Figure 43 (left).

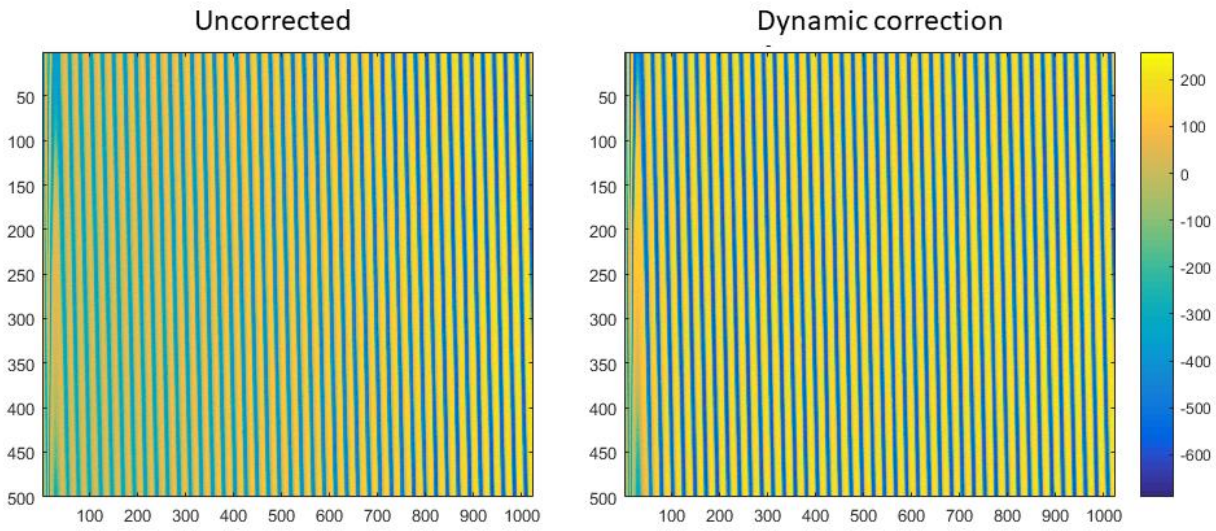

Figure 43. Images of a tilted diffraction grating with active focusing turned on/off. (left) Due to the different distance of each pixel from the focus of the objective created by the tilt of the diffraction grating in both x and y, the image shows most of the regions are out-of-focus when active focusing is off. (right) With active focus turned on, all pixels are now in focus.

To correct the out-of-focus pixels, a scaled voltage map is created to drive the Revibro DM to pull the focus to scan across the oblique plane. The wavefront map is as shown in Figure 44.

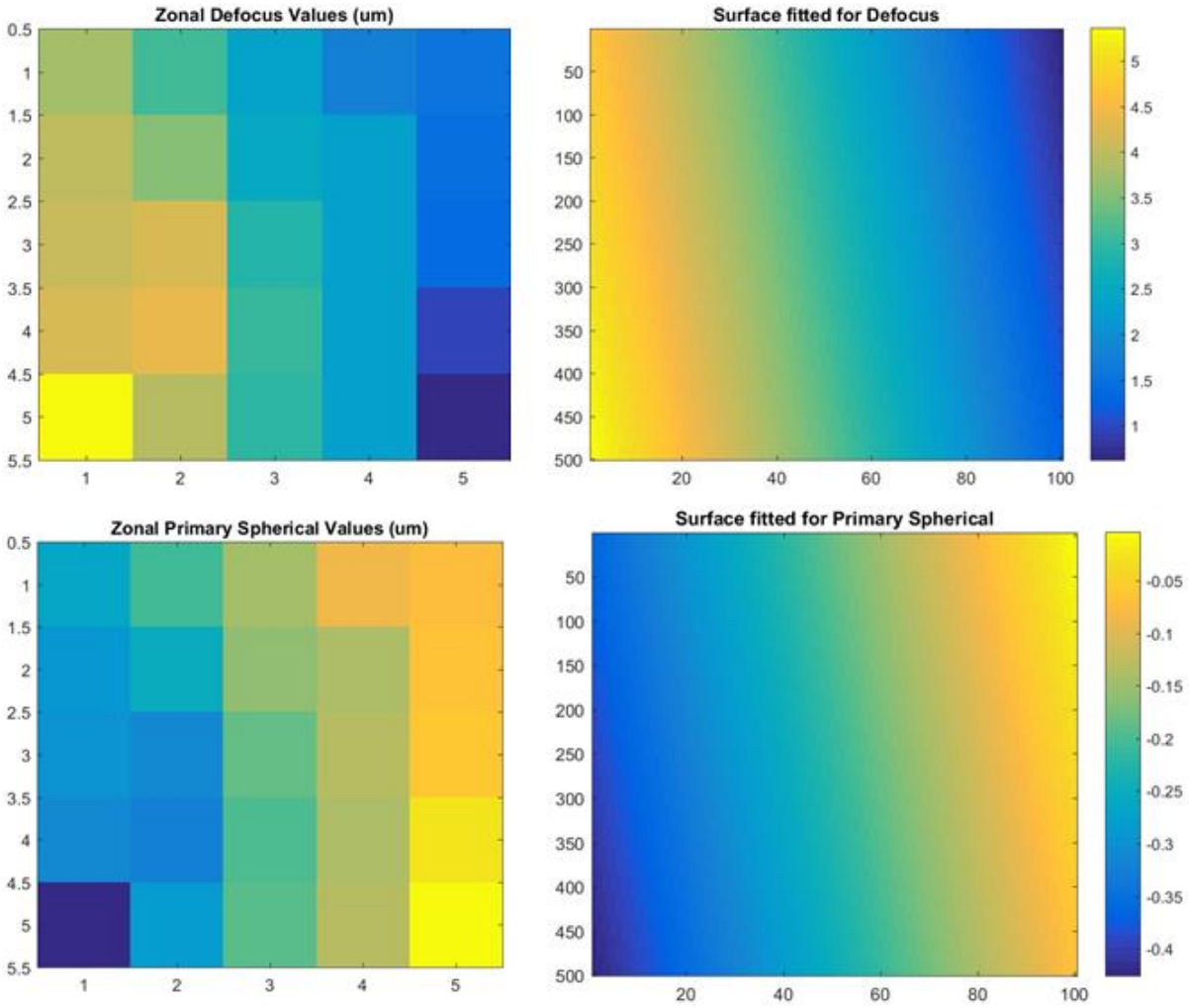

Figure 44. The wavefront map for focus control and primary spherical aberration correction for imaging the tilted diffraction grating shown in Figure 43. (Upper left) The actual defocus ($\tilde{Z}_{2,0}$) value applied in each of the 25 zones during active training for tracking the contour surface; (Lower left) The actual value for the primary spherical aberration ($\tilde{Z}_{4,0}$)during active training; (Upper right) The surface-fitted voltage map from the 5 by 5 zonal defocus value to a smooth 100 points per line by 500 lines (50,000 points); (Lower right) The similar surface-fitted primary spherical value from the 5 by 5 zonal value. One remark to make here is that the secondary spherical aberration ($\tilde{Z}_{6,0}$) has a very small value (<10nm) which was ignored. The contrast was the parameter used for the optimization merit function.

Since the wavefront map created by the defocus ($\tilde{Z}_{2,0}$) of the Revibro DM is linearly proportional to the focus adjustment at the image plane, it is very intuitive to see

thesmooth transition from minimum to maximum focus adjustment in both the x and y direction of the wavefront map, which resembles a tilted plane that matches the actual tilted diffraction grating. At minimum focus adjustment at upper right-hand corner of the image (as shown in Figure 44, the defocus value is near zero), it indicates that a collimated beam illuminates the objective and there should not be any primary spherical aberration in the optical system. On the other hand, the largest amount of primary spherical aberration correction is needed at maximum focus adjustment at the lower left-hand corner. The wavefront map for primary spherical aberration correction shown in Figure 44(lower) validates this assumption.

Imaging 1μm holes in an aluminum coating on a glass substrate. In our previous studies [5], we have demonstrated that both our woofer and tweeter can support intra-scan correction at scan rates up to about 1kHz. The goal is to control both focus and aberrations on an arbitrary focal plane to deliver diffraction-limited imaging throughout the accessible 3-D object space.

To evaluate the focus control and dynamic aberration correction, a negative beads target on glass has been made on the microfabrication facility here at MSU (Thanks to Tianbo Liu for making this target). To make the negative target, a sparse layer of 1 μm polystyrene beads was deposited on the slide using spin-casting. Then the slide was coated with a thin layer of aluminum using thermal evaporation. After the aluminum coating was applied, the beads were lifted off with Piranha etch (sulfuric acid mixed with hydrogen peroxide), leaving physical 1μm holes in the aluminum film. Comparing to the target shown in Figure 39, there are features throughout the field of view. All these

features are possible targets for sensorless wavefront optimization. It will be a much preferable target to demonstrate that dynamic aberration correction can improve contrast everywhere in the field of view.

As shown in the uncorrected image (Figure 45, upper), only the holes in the aluminum target in the right-hand side of the image are in focus. Since there is a heavy tilt away from the natural focus of the objective, the 1μm holes on the left-hand side of the target are nowhere to be seen.

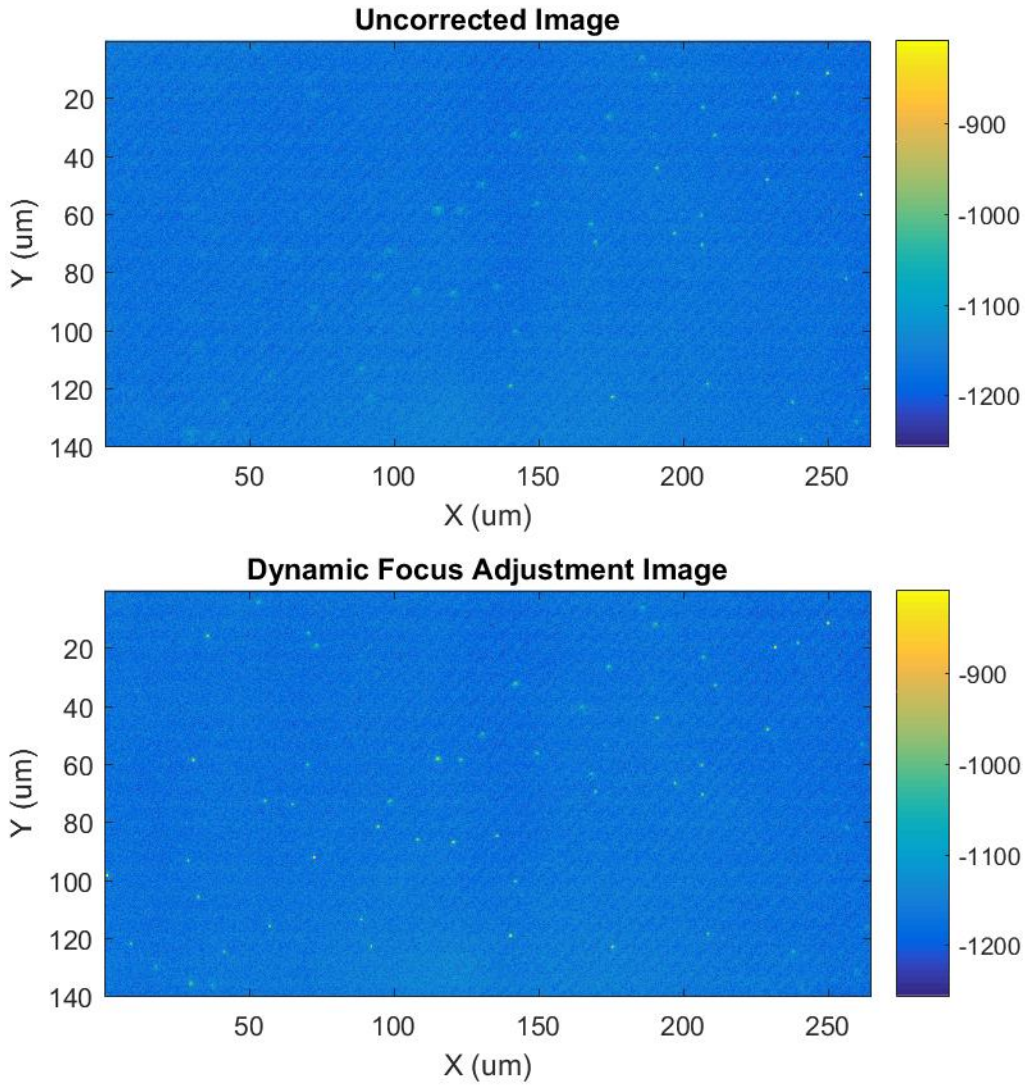

Figure 45. Active focusing on a tilted negative resolution target. (Upper) Static focusing only shows one side of the resolution target. (Lower) Active focusing tracks the tilted image plane and brings all features in focus.

The first step is to bring all the features on the imaging target in focus. Optimizing defocus is performed for the 25 sub-regions. The 25 optimized defocus values are linearly curve-fitted to create a smooth transition to track the tilted surface. A maximum difference of 1μm in defocus ($\tilde{a}_{2,0}$) is shown in the scale bar, which corresponds to a

10µm focus adjustment in the image sample. It shows that the surface fitted defocus map for the active focusing matches well with tilt of the target.

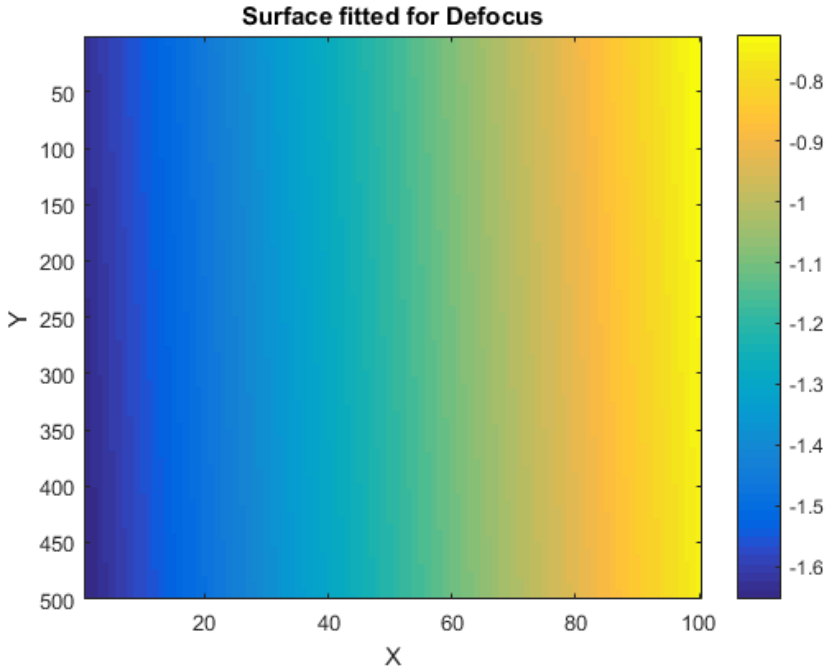

Figure 46. The fitted 100 by 500 points of defocus to track the tilted target.

The result of active surface tracking is shown in Figure 45 (lower). In the entire 150µm by 300µm field of view, all 1µm holes can be clearly seen despite some blurring due to the remaining spherical aberrations and off-axis aberrations. The next step is to correct the residue aberrations during the active scanning.

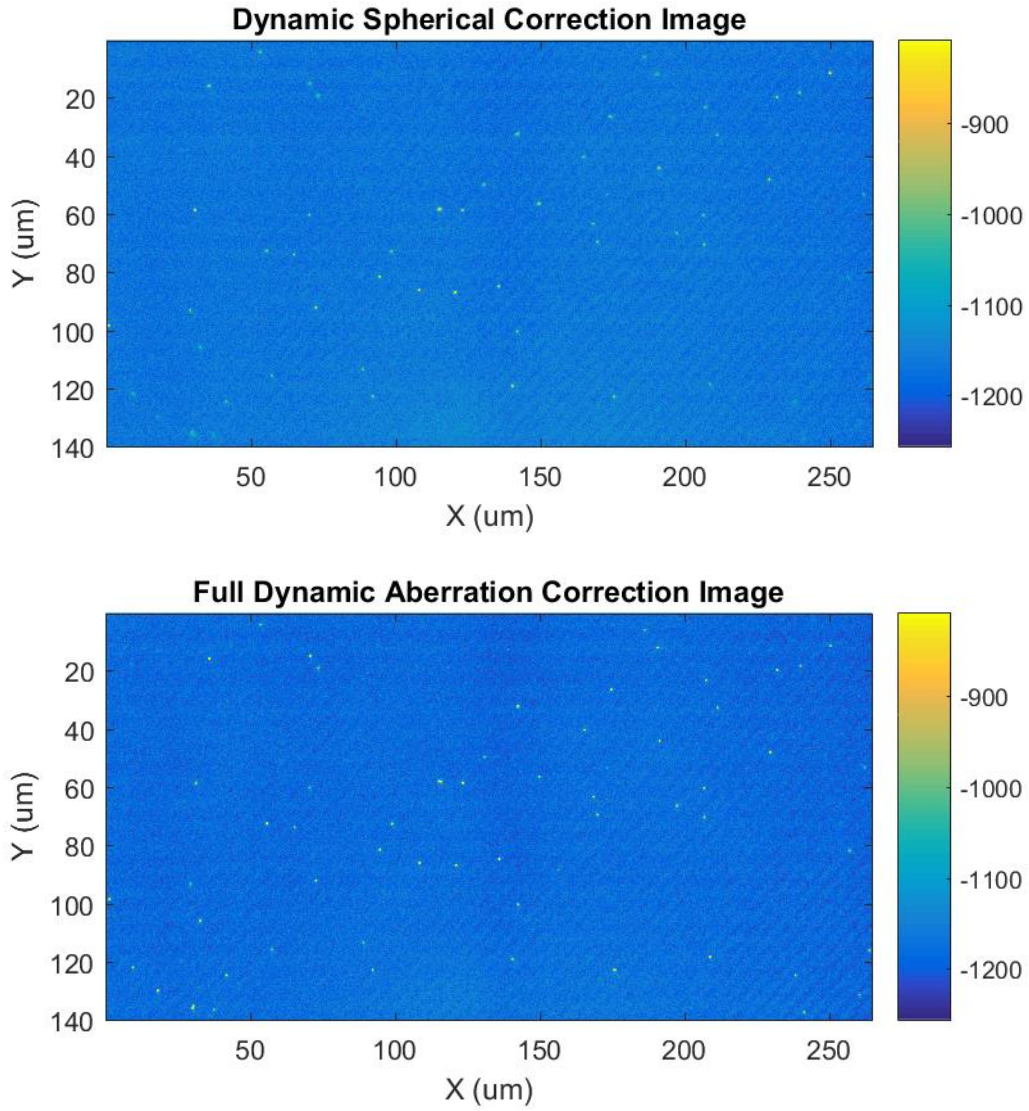

Figure 47. The dynamic aberration correction throughout the entire field of view. (upper) Active surface tracking with spherical aberration corrected; (lower) Active surface tracking with all aberration corrected.

The primary source of spherical aberration derived from the fact that a converging beam illuminates the objective at the left-hand side of the image. Spherical aberration can profoundly reduce the contrast, as well as the signal strength. As shown in Figure 47 (upper), the 1μm holes near the center become tighter after spherical aberrations are

corrected. To further improve the contrast near the four edges of the image, off-axis aberrations are corrected as shown in Figure 47(lower). To quantify the sharpening of the image, PSFs of the 1μm holes at different locations in the image are obtained from fitting the line profile.

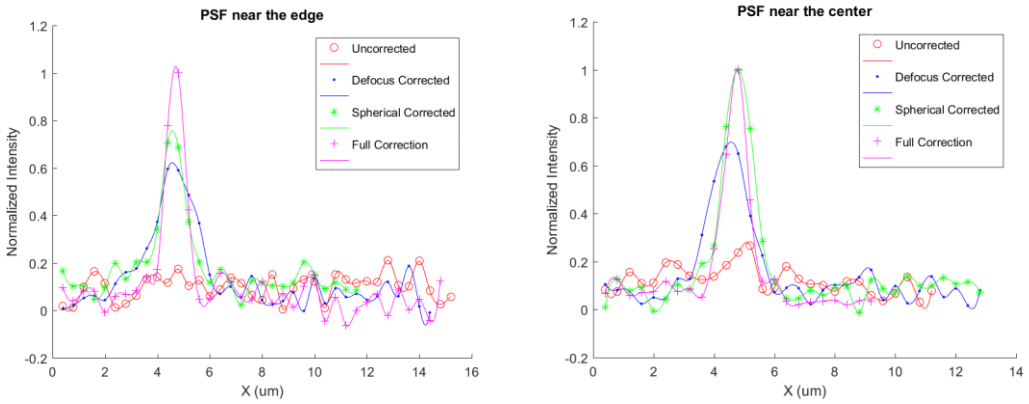

Figure 48. Improvement in PSFs for the 1μm holes near the edge (left) and near the image center (right).

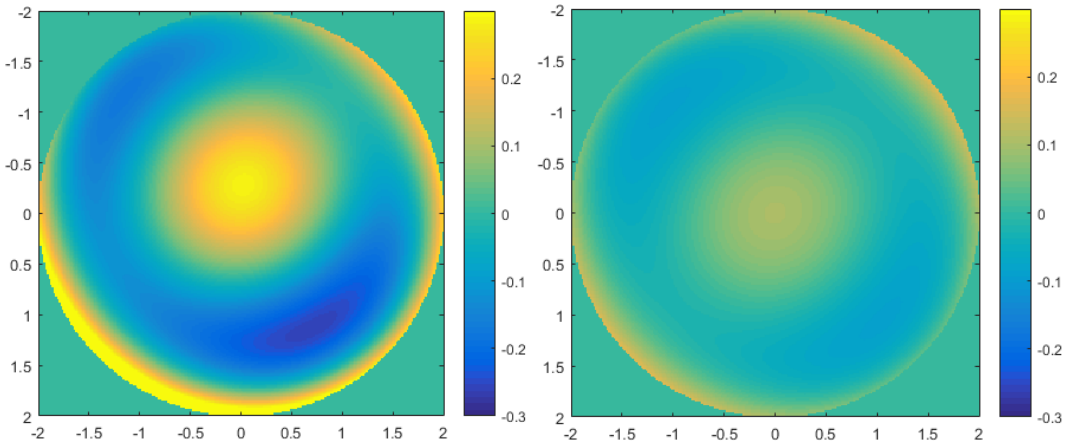

Figure 49. The wavefront maps for aberration compensation (left) near the edge and (right) at image center.

As shown in Figure 49, there is a very noticeable difference for the two wavefront maps used to recover the Strehl for the PSFs near the edge and in the center FOV. It

justifies our hypothesis that there is a significant spatial variance in the aberration present throughout the field of view, even for systematic aberrations without any sample structure. It is not hard to imagine that some form of an ‘averaged’ wavefront map of the two shown in Figure 49 may improve some areas of the image while making other worse. This is the limitation of static aberration correction. Comparing to biological samples, this tilted negative imaging target does not show as much variation as might be expected from a biological specimen. We expect even higher spatial variance of sample induced aberration in biological specimens.

Poland et al have shown that a point-by-point correction as the microscope scanned through brain tissue could lead to higher image quality in principle. However, the bandwidth of the available adaptive elements was the concern [67]. In the review of current technology in adaptive optical microscopy done by Booth, it is also stated that simulations have shown that better image quality can be achieved by employing multiple correction devices placed in planes conjugate to different depths in the specimen and applying different wavefront corrections depth by depth and region by region in each depth in the specimen [15]. Our adaptive/active microscope offers a simpler approach by using two fast MEMS DMs in a ‘woofer-tweeter’ configuration, demonstrating the true potential of aberration corrections depth by depth and region by region with dynamic focus control and aberration correction. So far, we were able to compensate all the spatially varied aberrations in a $300\times150\times20\mu m^3$ 3D volume and produce a diffraction-limited image throughout the entire field of view.

Imaging with Biological Samples

Rabbit Testis. The imaging target is a stained slice of a rabbit testis on a microscope slide (AMSCOPE, USA). A cover glass of approximately 0.3mm in thickness was used to seal the biological sample. Unlike imaging into thick tissue, this biological specimen has a minimum thickness and we are simply imaging the surface. The correction collar of the objective lens was purposely set to 0 to introduce additional spherical aberration. The imaging sample is mounted heavily tilted on an x-y-z motorized sample stage. There is a maximum tilt of 20 microns (in the sample space) from the leftupper corner of the image to the right lower corner of the image. As a result, only the left-hand side of the image is in reasonably good focus, while the rest of the image is heavily blurred and features are not recognizable as shown in Figure 50.

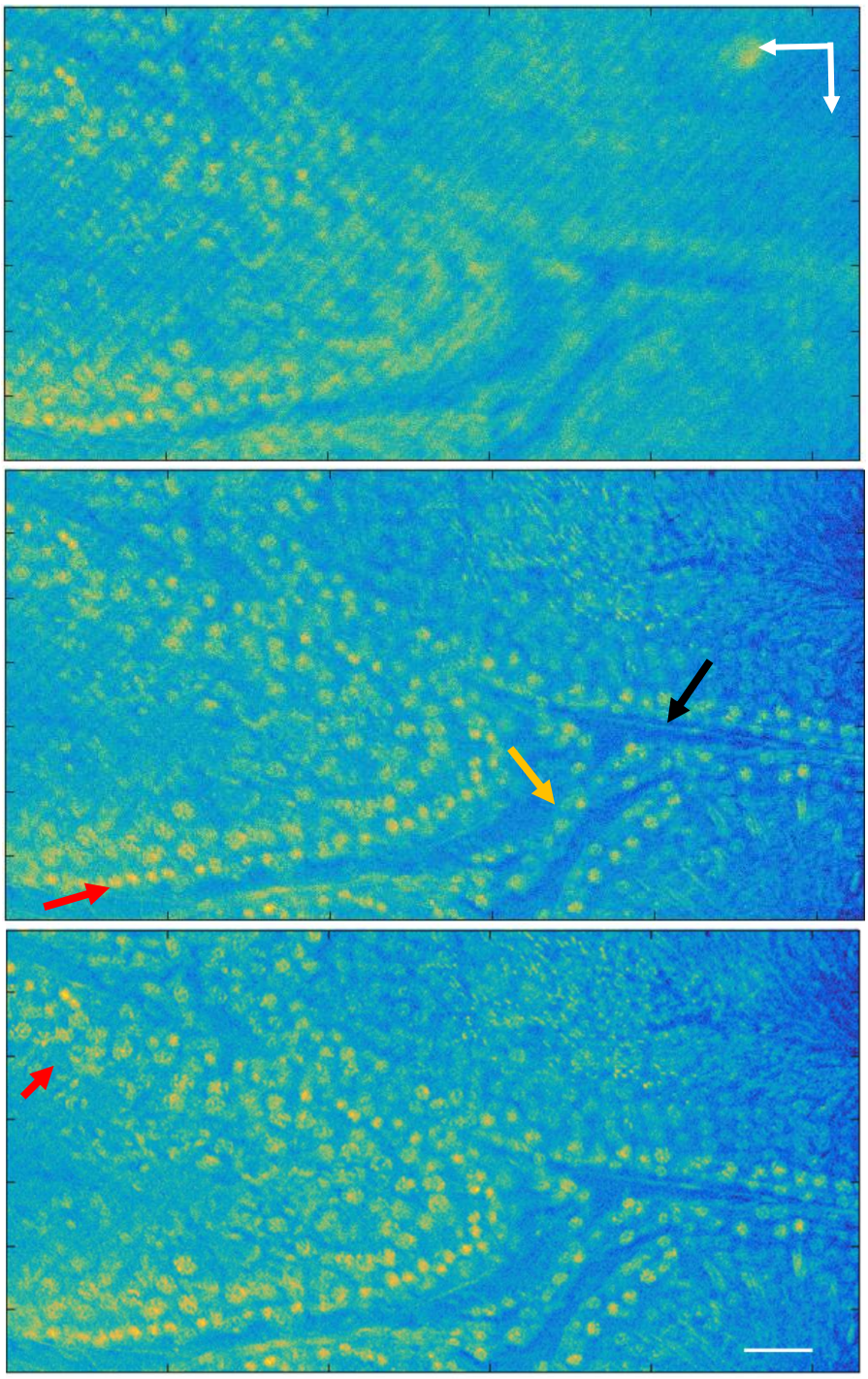

Figure 50. Dynamic focus control and aberration correction on a rabbit testis in vitro. (upper) Uncorrected image, the horizontal axis shows the x direction while the vertical axis shows the y direction; (mid) After dynamic focus control and spherical aberration correction. The red arrow points at the Sertoli nuclei. The black arrow points at the lamina propri. The yellow arrow points at the Leydig cells; (lower) Both spherical and

off-axis aberrations are corrected during dynamic focus control. The red arrow points at the Spermatocytes. The white scalebar is 20μm.

To enhance the image quality, the first step is to track the tilted surface and correct the spherical aberration. Although the imaging sample in vitro may not have a large amount of sample induced aberrations, there are two main sources of the aberrations, 1) coverslip induced spherical aberration and 2) the aberrations arise from the focus control. The objective lens and the relay lenses are optimized only for a collimated incident beam. The dynamic focus control with MEMS DM introduces a converging and diverging beam into the optical system during surface tracking of this heavily tilted biological sample. Consequently, both spherical aberration and off-axis aberration arise.

Nonetheless, the difference in refractive index between spermatocytes, seminiferous tubules, Sertoli cells and muscular cells are good for image-based optimization for contrast. A combination of dynamic focus control and spherical aberration correction immediately brings all features throughout the field of view in focus with high contrast. The Sertoli nuclei shows a much higher contrast and became much sharper. The seminiferous tubules become much better defined. The Leydig cells were not recognizable before the correction but now it is shown with high clarity. Lastly, the off-axis aberration correction further improves image quality near the edges of the image. The spermatocytes locate near the left edge of the image are much higher in clarity after off-axis aberrations are compensated. Here we demonstrated a fully corrected image with a biological sample within the $300\times150\times20\mu m^3$ 3D volume.

Rabbit Spinal Cord.

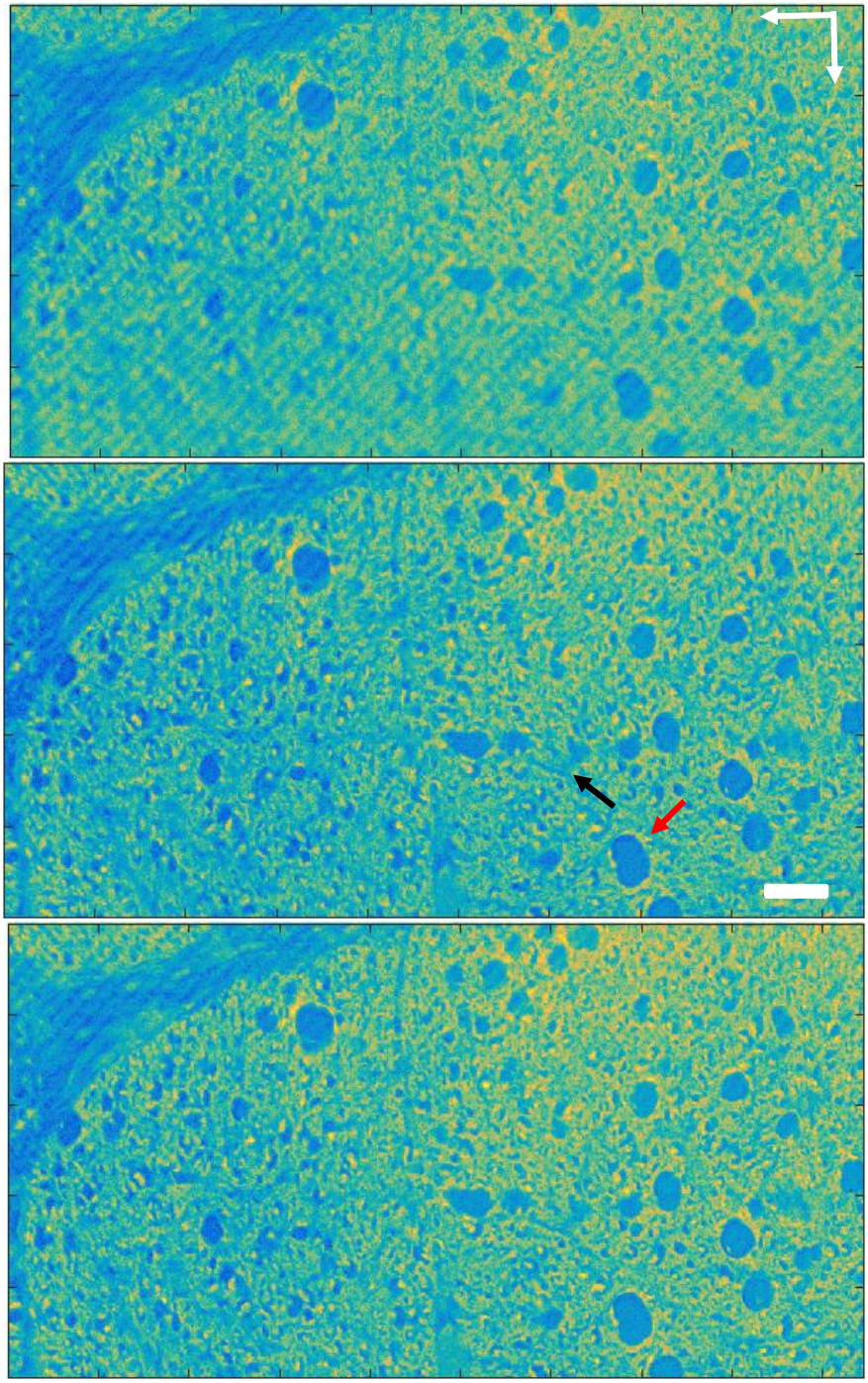

Figure 51. Active focus adjustment and dynamic aberration correction on an image of Rabbit spinal cord. (Upper) Uncorrected image, the horizontal and vertical axis show the direction of x and y; (Mid) Active focus adjustment and dynamic spherical aberration correction. (Red arrow) Neuron cell body, (Black arrow) small vessel with fibrin-like thrombi, the scale bar is 20μm; (Lower) Dynamic correction for off-axis aberrations.

The imaging target shown in Figure 51 is a cross section of a stained rabbit's spinal cord on a microscope slide (AMSCOPE, USA). A 25x water immersion objective lens with coupling gel is used for imaging. A cover-glass of 0.3mm is used to seal the biological sample, but the correction collar is set to zero to intentionally introduce spherical aberration. Therefore, the uncorrected image in Figure 51 (Upper) shows blurring across the entire image. As the biological sample is mounted on an x-y-z motorized sample stage with a significant amount of tilt in the y direction, the lower half of the image is out of focus. The merit for sensorless wavefront optimization is contrast. The active focus adjustment with the woofer DM tracks the tilt of the image surface and corrects the spherical aberration throughout the field of view (Figure 51 (mid)). Finally, the off-axis aberration correction brings out the even finer features in the grey matter of the rabbit spinal cord.

DISCUSSION AND CONCLUSION

Summary of this Research

In this thesis I reported a new imaging platform to track irregular surfaces with complex topography while correcting aberrations on the fly to produce diffraction limited images throughout the 3D field of view of $300\times300\times30\mu m^3$. A total focus adjustment of ~80 μm in aqueous samples has been achieved with partial aberration correction.

Traditional AO microscopy employs one single wavefront correction map applied to the entire image of a flat surface, hoping for an improvement in overall image brightness or contrast. Our novel imaging platform can perform dynamic focusing during scanning to produce images of more convoluted surfaces, turning a conventional 2D imaging tool into a real-time 3D image acquisition platform. More importantly, it is capable of delivering a diffraction-limited image throughout the entire (3D) field of view by applying different wavefront maps for different image locations dynamically while keeping up with the active scanning. We call this as an active/adaptive microscope.

The core technology of this imaging platform is an active/adaptive optical module. It consists of two MEMS DMs, a ‘woofer’ for focus control and spherical aberration correction and a ‘tweeter’ for non-axially-symmetric aberration correction. The fast response of these MEMS DMs leads to an aberration-corrected beam scanning throughout a 3D volume. We performed the first reported dynamic measurements of candidate deformable mirrors, examining the sinusoidal steady state and step response associated with specific Zernike modes on the mirrors and the settling time for the

residual wavefront errors, verifying the suitability of these new optical elements for dynamic aberration and focus control.

Following numerical modeling, Zemax simulations, shape training and dynamic testing, we implemented the AO module using a Revibro DM with 4 annular actuators and a BMC Multi-DM with 140 active actuators as the 'woofer-tweeter' configuration. Both BMC Multi-DM and Revibro DM have demonstrated that they can maintain rms error less than 20nm, while keeping up with active scanning at low kHz scan rates during dynamic testing. Placed in conjugate planes to the back focal plane of the objective lens, the two MEMS DMs demonstrated capability of producing a fully corrected 3D volume of $400\times400\times30\mu m^3$. Although the maximum deflection of the Revibro DM can introduce over 80μm of focus adjustment in image space, the spherical aberration from the focus adjustment requires the differential voltages among the four electrodes to exceed the maximum voltage the membrane can handle.

We implemented sensorless wavefront aberration correction and produced images of different targets with our active/adaptive microscope. The sub-micron resolution targets verified that our optical system is truly diffraction limited after both on-axis and off-axis aberrations are being corrected. A tilted target with negative one-micron features (1 um holes in an aluminum film) demonstrated that we can track a tilted surface with 20μm focal depth shift across a $300\times300\ \mu m^2$ field of view. Nearly all the one-micron features show a 1μm FWHM throughout the entire field of view, as predicted by simulation for a diffraction limited beam shape. Finally, the images of rabbit testis and spinal cord illustrated how active/adaptive microscopy can open a new frontier for real-

time imaging of biological samples over irregular surfaces with complex topography with high clarity.

Limitations Encountered

Stabilization of the Revibro DM. The SU-8 based MEMS DM is very sensitive to change in humidity and temperature. The deflection of the membrane can change as it absorbs water molecules in the air or as it warms. As the deflection of the membrane changes, the voltage maps trained for different amplitude of defocus, primary spherical and secondary spherical aberrations vary. Consequently, we developed a single point calibration technique to allow us to predict the new voltage map quickly by simply finding the new bias voltage that will give the same deflection as previously trained. Additionally, a humidity control chamber with 5% dry air intake is installed on the Revibro DM to locally set the humidity around the Revibro DM to be around 5% constantly. Although it is far from perfect, the humidity chamber reduced the large fluctuation in deformation of the membrane. As a result, some extreme cases such as snap down of the Revibro DM could be avoided.

Influence of humidity on behavior of the Revibro DM. Due to the fact SU-8 materials absorb water molecules present in the air, the voltages used for focus control and spherical aberrations are substantially affected by the humidity. We set up a direct wavefront measurement to evaluate the how humidity affects the behavior of the Revibro DM (shown in Figure 52). With a 4f relay, the Revibro DM is imaged onto the wavefront sensor. A fold mirror is inserted into the 4f relay to steer the beam off the imaging path

onto the WFS. It enables temporary solution to install the WFS into the system without alternating the optics in the microscope.

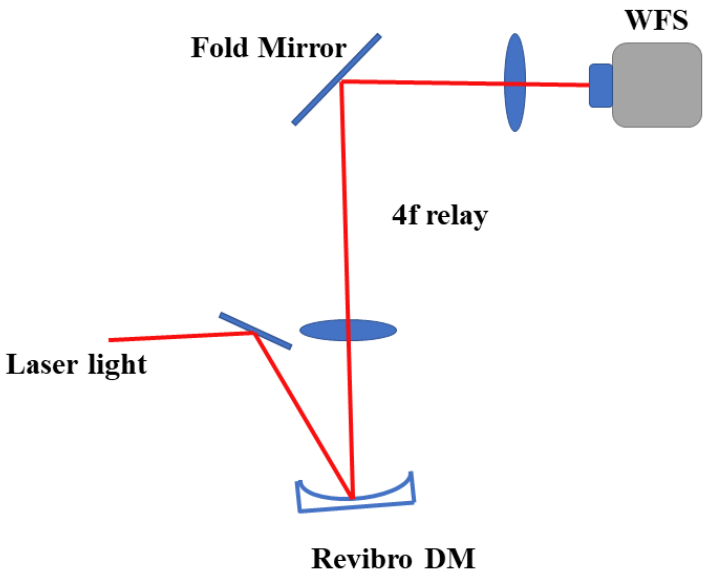

Figure 52. The system setup for direct wavefront measurement under the influence of different humidity.

During each wavefront measurement, an equipotential voltage sweep from 160 to 280V is applied on the 4 electrodes of the Revibro DM. The illumination beam is a diverging beam onto the Revibro DM. As the Revibro DM deflects, it gradually adds defocus ($\tilde{Z}_{2,0}$) to the wavefront of the illumination beam and produce a collimated beam near the half way of its maximum deflection. As the Revibro DM continues to increase the amplitude of the defocus ($\tilde{Z}_{2,0}$), the illumination beam becomes a converging beam. This change in defocus ($\tilde{Z}_{2,0}$) is recorded by the WFS.

Before each wavefront measurement, the humidity near the Revibro DM is recorded. We have performed the wavefront measurement on days with different ambient humidityand here are some results from the measurements. As shown in Figure 53, 9% of humidity change can result in a difference of over 25 volts for the equipotential electrode voltage required to produce the same defocus ($\tilde{Z}_{2,0}$) on the Revibro DM. At 14% humidity, the same defocus to create a collimated beam requires an equipotential of V_1 = 220V on the electrodes. The required voltage increases to V_2 = 247V after the humidity decreases to 5%. This high sensitivity to humidity makes it extremely difficult to control or predict the shape of the Revibro DM. It is possible to get around this problem by performing a new calibration each time there is a change in humidity, but recalibration is very time consuming. More importantly, a new calibration requires a WFS that does not exist during sensorless wavefront optimization.

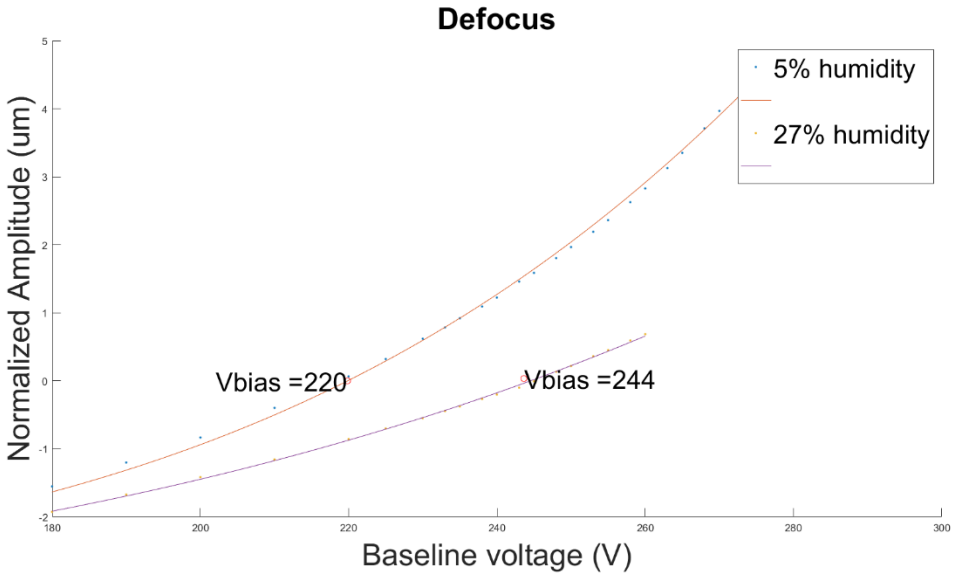

Figure 53. Voltages applied vs Defocus ($\tilde{Z}_{2,0}$) produced on the Revibro DM under the influence of different humidity

Nonetheless, the calibration curves shown in Figure 53 provide useful information that enables a way to update a table of control voltages based on V_1 and V_2. This is a method called single point calibration.

Single Point Calibration

Here I would like to give special thanks to Ryan Downy for his input in this topic.

The focus control mirror may be modeled as a suspended membrane under tension *T* with deflection *s*, subject to an applied pressure *p*, which is governed by the differential equation (for static displacement)

Equation 26. $\nabla^2 s(r) + \frac{p(r)}{T} = 0$

where the electrostatic pressure $p(r) \propto V^2(r)$. We assume thatchange in humidity (or temperature) leads tochange in the tension *T*. For a membrane under tension T_1 with squared voltage profile $V_1^2(r)$, or the same membrane under tension T_2 with squared voltage profile $V_2^2(r)$, the displacement $s(r)$ will be identical provided

Equation 27. $\frac{V_1^2(r)}{T_1} = \frac{V_2^2(r)}{T_2}$.

In other words, if the tension in the membrane changes, then for static displacements, it is only necessary to scale the voltage profile appropriately to maintain a desired shape.

Equation 28. $V_1(r) = \sqrt{\frac{T_1}{T_2}} V_2$

To collimate the same diverging beam, the defocus ($\tilde{Z}_{2,0}$) is the same throughout different dates with different humidity (two different operating points). Thus, the deflection of the membrane s must also be the same for two different operating points ($s_1 = s_2$). Therefore, we require

Equation 29. $V_1(r) = \sqrt{\frac{T_1}{T_2}} V_2$

From the equation above, it indicates that new voltage (for each zone) can be obtained by multiplying the old voltage by a linear scaling factor. Although the intrinsic stress cannot be directly measured, the ratio of intrinsic stress at two different operating points can be replaced by the ratio of the two calibration points V_1 and V_2. This yields the equation for updating the voltage profile with single point calibration:

$$\text{Equation 30. } V_{new} = \frac{V_2}{V_1} \times V_{old}$$

Equation 30 can be applied to any calibration that has been performed previously. As long as the old bias voltage V_1 (voltage required to collimate the incident beam) is recorded, a new voltage versus defocus curve can be created by finding the new bias voltage V_2.

For example, if we would like to use the voltage versus deflection curve trained at 5% humidity on the day when the humidity is at 14%, we only have to measure the new bias voltage. As shown in Figure 53, the bias voltages at 5% humidity and 14% humidity are V_1 = 247V and V_2 = 220V respectively. Hence the updated mirror voltage can be calculated as below:

$$\text{Equation 31. } V_{new} = \frac{V_2}{V_1} \times V_{old} = \frac{220}{247} V_{old}$$

Image based single point calibration. With a WFS installed in the system, it is very convenient to measure the new bias voltage. However, the extra time and space required to keep the WFS working during imaging makes itimpractical. We develop an image based single point calibration making use of the eye piece of the microscope stand.

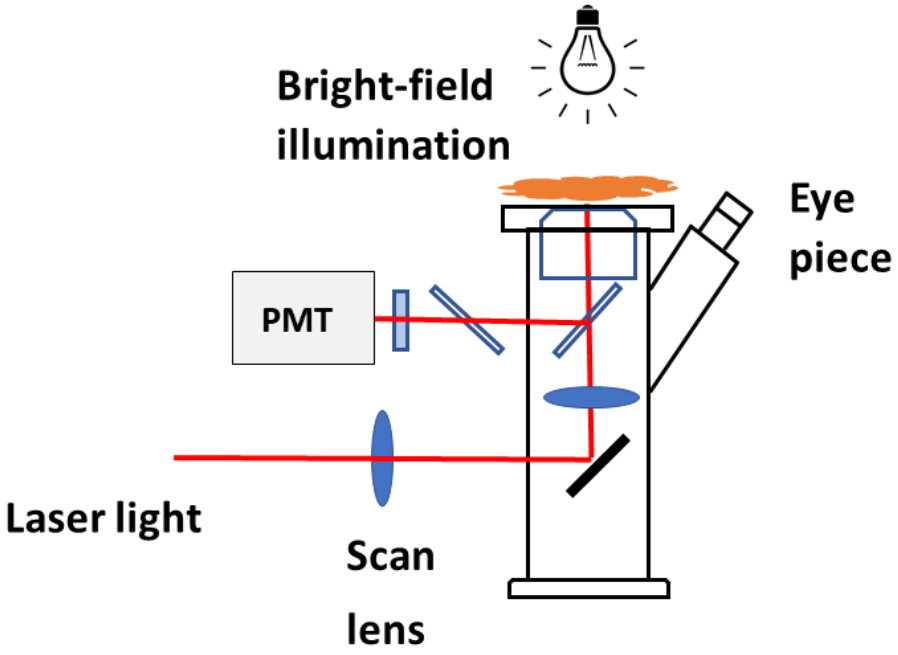

Figure 54. Setup for the image base single point calibration.

As shown in Figure 54, a LED is used as bright–field illumination through the imaging target mounted on an x-y-z sample stage. This white light will be collected by the objective lens. Through an eye piece, we can adjust the imaging target to the best focus. After turning off the LED light and switching to the laser light from the side port, we start collecting real time images with the PMT. By searching for thesame image target seen in the eye piece, we can bring the features in focus in the real time image collected with the PMT by active focus adjustment on the Revibro DM. (worked with Aleesha) Once the image is in focus, we can record the voltage applied on the Revibro DM and this is the new bias voltage V_2. Now all of the updated mirror voltages can be scaled properly using the previously trained mirror voltages, for any combination of Zernike modes.

As an example, a previous training for defocus and spherical aberration was carried out in the environment of 5% humidity and room temperature at 25°C. The bias voltage was found to be 253V. The same training data is used to create a target shape consisting of 1.8μm of defocus ($\tilde{Z}_{2,0}$) and 200nm of primary spherical ($\tilde{Z}_{4,0}$) under two different levels of humidity. The results are summarized in Table 9.

Table 9. The measured Zernike spectrum for the target shape produced under different levels of humidity using single point calibration. All units for the Zernike polynomials are in micron.

HUM (%)	Temp (°C)	$\tilde{Z}_{2,0}$	$\tilde{Z}_{4,0}$	$\tilde{Z}_{6,0}$	$\tilde{Z}_{2,-2}$	$\tilde{Z}_{2,2}$	$\tilde{Z}_{3,-3}$	$\tilde{Z}_{3,1}$
34	21	1.74	0.224	0.01	-0.096	0.013	0.054	0.072
12	21	1.74	0.23	0.02	-0.09	0	0.057	0.085

As shown in Table 9, the new bias voltages are found to be 190V for 34% of humidity and 238V for 12% of humidity. The Zernike spectrum shows that the wavefront produced with the Revibro DM is very close to the target shape, although there is a significant amount of astigmatism ($\tilde{Z}_{2,-2}$) and coma ($\tilde{Z}_{3,1}$) inherent to the Revibro DM.

Suggestions for Future Work

Future development of the Revibro DM. More advanced techniques are under development to further stabilize the performance of the Revibro DM. For instance, closed-loop capacitive sensing will constantly monitor the air gap between the membrane and substrate to produce a feedback on deflection of the membrane. In this case, the wavefront shape produced by the Revibro DM can be directly monitored to ensure accuracy. On the other hand, a hermetically sealed packaging could keep the MEMS DM

in a dry nitrogen environment. These techniques should make the optical performance of the Revibro DM more consistent. We anticipate these improvements will be incorporated into future versions of the Revibro mirror, making calibration of the active/adaptive microscope more straightforward.

Installation of the Ti:Sapphire Tunable Laser and Imaging with 2PM. To truly demonstrate the power of active/adaptive microscopy, we wish to implement it on a multi-photon platform. All our design is based on a two-photon microscope platform. So far, we have been imaging with a 10mW diode laser at wavelength of 635nm. To perform proper two-photon excitation fluorescence microscopy, we will need a higher power laser with a shorter pulse at the wavelength around 1μm to match with the excitation wavelength of two photon dyes. The microscope will be installed next to a Ti:Sapphire tunable femtosecond laser located in Cooley lab in the next stage of this research project.

A few modifications will be required before the 2PM can be fully functional. It begins with the femtosecond pulsed laser source. First, thebeam divergence and waist location of the laser source need to be carefully adjusted to match the current optical design.

Secondly, due to the low efficiency of two-photon excitation, the peak power is important for a femtosecond laser source. As the peak power is inversely proportional to the pulse width, it is beneficial to have the shortest pulse width so as to achieve the best possible fluorescence emission. However, the pulse width is temporally broadened as it travels through optical materials, which includes both the optical elements in the microscope and the imaging sample. This is the effect of dispersion. . Pre-compensation

is required to counteract the effect of dispersion. A prism pair are usually used to introduce a negative dispersion to keep the short pulse at the focal point.

Thirdly, depth-dependent power control is another important feature for beam management. As we are actively changing the focus location in the imaging sample, it is highly desirable to dim the beam while imaging at the surface and increase the intensity at depth. In this way, we will be able to ensure sufficient signal strength and prevent photo-bleaching. Moreover, this depth-dependent power control needs to be dynamically synchronized with the Revibro DM. An electro-optic linear polarizer with bandwidth of 1 kHz and over will be needed for this application.

Fourth, the pulsed femtosecond laser has a wavelength around 1μm while the current optics are aligned for a laser source of 635nm. A fine adjustment will be needed to accommodate the new laser source. New filters will be installed into the PMT block to collect the fluorescence emission while rejecting the scattered photons from excitation light.

Last but not the least, more tasks are lying ahead for software development. We would like to collect images based on two separate PMT detectors for 2PM as well as reflected light imaging. We will need to expand new image channels and gain control for additional PMTs.

REFERENCES

[1] A. P. Alivisatos, M. Chun, G. M.Church, R. J.Greenspan, M. L.Roukes and R. Yuste, "The Brain Activity Map Project and the Challenge of Functional Connectomics," *Neuron,* vol. 74, no. 61, pp. 970-974, 2012.

[2] A. Vogt, Y. Guo, S. P. Tsunoda, S. Kateriya, M. Elstner and P. Hegemann, "Conversion of a light-driven proton pump into a light-gated ion channel," *Scientific Reports,* vol. 5, p. 16450, 2015.

[3] K. Svoboda, F. Helmchen, W. Denk and D. W. Tank, "Spread of dendritic excitation in layer 2/3 pyramidal neurons in rat barrel cortex in vivo," *Nat. Neuroscience,* vol. 2, no. 1, pp. 65-73, 1999.

[4] D. Kobat, N. G. Horton and C. Xu, "In vivo two-photon microscopy to 1.6-mm depth in mouse cortex," *J. Biomed. Opt.,* vol. 16, no. 10, 2011.

[5] C. C. Archer-Zhang, W. B. Foster, R. D. Downey, C. L. Arrasmith and D. L. Dickensheets, "Dynamic performance of microelectromechanical systems deformable mirrors for use in an active/adaptive two-photon microscope," *Journal of Biomedical Optics,* vol. 21, no. 12, p. 121507, 2016.

[6] D. Kobat, M. E. Durst, N. Nishimura, A. W. Wong, C. B. Schaffer and C. Xu, "Deep tissue multiphoton microscopy using longer wavelength," *Opt. Express,* vol. 17, no. 16, pp. 13354-13364, 2009.

[7] M. J. Booth, M. A. A. Neil, R. Juskaitis and T. Wilson, "Adaptive aberration correction in a confocal microscope," *Journal of Biomedical Optics,* vol. 99, no. 9, pp. 5788-5792, 2002.

[8] P. N. Marsh, D. Burns and J. M. Girkin, "Practical implementation of adaptive optics in multiphoton microscopy," *Optical Express,* vol. 11, no. 10, pp. 1123-1130, 2003.

[9] P. Tsai, B. Migliori, K. Campbell, T. Kim, Z. Kam, A. Groisman and D. Kleinfeld, "Spherical aberration correction in nonlinear microscopy and optical ablation using a transparent deformable membrane," *Applied Physics Letter,* vol. 91, 2007.

[10] A. Mertz and J. Leray, "Rejection of two-photon fluorescence background in thick tissue by differential aberration imaging," *Optics Express,* vol. 14, pp. 10565-10573, 2006.

[11] D. Debarre, E. J. Botcherby, T. Watanabe, S. Srinivas, M. J. Booth and T. Wilson, "Image-based adaptive optics for two-photon microscopy," *Optics Letters,* vol. 34, no. 16, pp. 2495-2497, 2009.

[12] Y. Zhou, T. Bifano and C. Lin, "Adaptive optics two-photon fluorescence microscopy," *Proc. SPIE,* 2007.

[13] N. Ji, D. E. Milkie and E. Betzig, "Adaptive optics via pupil segmentation for high-resolution imaging in biological tissues," *Nature Methods,* vol. 7, pp. 141-147, 2009.

[14] L. Kong and M. Cui, "In vivo fluorescence microscopy via iterative multi-photon adaptive compensation technique," *Optics Express,* vol. 22, no. 20, p. 23786, 2014.

[15] M. J. Booth, "Adaptive optical microscopy: the ongoing quest for a perfect image," *Light:Science & Applications,* vol. 3, no. e165, 2014.

[16] M. Moghimi, K. Chattergoon, C. Wilson and D. Dickensheets, "High speed focus control MEMS mirror with controlled air damping for vital microscopy," *Microelectromechanical Systems,* vol. 22, no. 4, pp. 938-948, 2013.

[17] M. Moghimi, B. Lutzenberger, B. Kaylor and D. Dickensheets, "MOEMS deformable mirrors for focus control in vital microscopy," *Journal of Micro/Nanolithography , MEMS, and MOEMS,* vol. 10, no. 2, pp. 023005-023005-8, 2011.

[18] S. J. Lukes and D. L. Dickensheets, "Agile scanning using a MEMS focus control mirror in a commercial confocal microscope," in *Proc. SPIE 8949*, San Francisco, 2014.

[19] W. Denk, J. H. Strickler and W. W. Webb, "Two-Photon Laser Scanning Fluorescence Microscopy," *Science,* vol. 248, no. 4951, pp. 73-76, 1990.

[20] T. Corle and G. Kino, Confocal Scanning Optical Microscopy and Related Imaging Systems, San Diego: Academic Press, 1996.

[21] P. So, C. Dong, B. Masters and K. Berland, "Two-photon excitation fluorescence microscopy," *Annual review of biomedical engineering,* vol. 2, no. 1, pp. 399-429, 2000.

[22] P. So, C. Dong, B. Masters and K. Berland, "Two-Photon Excitation Fluorescence Microscopy," *Annual Review of Biomedical Engineering,* vol. 2, pp. 399-429, 2000.

[23] F. Bestvater, E. Spiess, G. Stobrawa, M. Hacker, T. Feurer, T. Porwol, U. Berchner-Pfannschmidt, C. Wotzlaw and H. Acker, "Two-photon fluorescence absorption and emission spectra of dyes relevant for cell imaging," *Journal of Microscopy,* vol. 208, no. 2, pp. 108-115, 2002.

[24] C.-Y. Dong, K. Koenig and P. So, "Characterizing point spread functions of two-photon fluorescence microscopy in turbid medium," *Journal of Biomedical Optics,* vol. 8, no. 3, pp. 450-459, 2003.

[25] A. K. Dunn, V. P. Wallace, M. Coleno, M. W. Berns and B. J. Tromberg, "Influence of optical properties on two-photon fluorescence imaging in turbid samples," *Applied Optics,* vol. 39, no. 7, pp. 1194-1201, 2000.

[26] D. A. Dombeck, C. D. Harvey, L. Tian, L. L. Looger and a. D. W.Tank, "Functional imaging of hippocampal place cells at cellular resolution during virtual navigation," *Nature Neuroscience,* vol. 13, no. 11, pp. 1433-1440, 2010.

[27] C. Dunsby and P. French, "Techniques for depth-resolved imaging through turbid media including coherence-gated imaging," *Journal of Physics D: Applied Physics,* vol. 36, no. 14, pp. 207-227, 2003.

[28] T. D. Wang, C. H. Contag, M. J. Mandella, N. Y. Chan and G. S. Kino, "Confocal fluorescence microscope with dual-axis architecture and biaxial postobjective scanning," *Journal of Biomedical Optics,* vol. 9, no. 4, pp. 735-742, 2004.

[29] M. Kempe and W. Rudolph, "Scanning microscopy through thick layers based on linear correlation," *Optics Letters,* vol. 19, no. 23, pp. 1919-1921, 1994.

[30] M. Booth, "Adaptive optics in microscopy," *Philosophical Transactions: Mathematical, Physical and Engineering Sciences,* vol. 365, no. 1861, pp. 2929-2843, 2007.

[31] J. Girkin, S. Poland, A. Wright, C. Freudiger, C. Evans, X. Xie, A. (. Periasamy and P. (. So, "Adaptive optics applied to coherent anti-Stokes Raman scattering microscopy," in *Proceedings of SPIE: Multiphoton Microscopy in the Biomedical Sciences VIII*, San Francisco, 2008.

[32] J. W. Cha, J. Ballesta and P. T. C. So, "Shack-Hartmann wavefront-sensor-based adaptive optics system for multiphoton microscopy," *Journal of Biomedical Optics,* vol. 15, no. 4, p. 046022, 2010.

[33] M. Feierabend, M. Rückel and a. W. Denk, "Coherence-gated wave-front sensing in strongly scattering samples," *Optics Letters,* vol. 29, no. 19, pp. 2255-2257, 2004.

[34] B. M. Corporation, "492-DM," Boston Micromachines Corporation, 2015. [Online]. Available: http://www.bmc.bostonmicromachines.com/492dm.htm. [Accessed 18 3 2017].

[35] B. Berge and J. Peseux, "Variable focal lens controlled by an external voltage: An application of electrowetting," *The European Physical Journal E,* vol. 3, no. 2, pp. 159-163, 2000.

[36] M. Ye and S. Sato, "Optical properties of liquid crystal lens of any size," *Jpn. J. Appl. Phys.*, vol. 41, no. 5, pp. 571-573, 2002.

[37] A. F. Naumov, G. D. Love, M. Y. Loktev and F. L. Vladimirov, "Control optimization of spherical modal liquid crystal lenses," *Optics Express,* vol. 4, no. 9, pp. 344-352, 1999.

[38] W. Zhang, H. Zappe and A. Seifert, "Wafer-scale fabricated thermo-pneumatically tunable microlenses," *Light: Science & Applications,* vol. 3, p. e145, 2014.

[39] N. S. a. S. Morita, "Variable-focus liquid-filled optical lens," *Applied Optics,* vol. 32, no. 22, pp. 4181-4186, 1993.

[40] G. Sshibuya, H. Yoshida and M. Ozaki, "High-speed driving of liquid crystal lens with weakly conductive thin films and voltage booster," *Applied Optics,* vol. 54, no. 27, p. 8145, 2015.

[41] B. H. W. HENDRIKS, S. KUIPER, M. A. J. V. AS and C. A. R. a. T. W. TUKKER, "Electrowetting-Based Variable-Focus Lens for Miniature Systems," *Optical Review,* vol. 23, no. 3, pp. 255-259, 2005.

[42] D. L. Dickensheets, "Requirements of MEMS membrane mirrors for focus adjustment and aberration correction in endoscopic confocal and optical coherence tomography imaging instruments," *Journal of Micro/Nanolithography, MEMS, and MOEMS,* vol. 7, no. 2, p. 021008, 2008.

[43] M. J. Moghimi, B. J. Lutzenberger, B. M. Kaylor and D. L. Dickensheets, "MOEMS deformable mirrors for focus control in vital microscopy," *Journal of Micro/Nanolithography, MEMS, and MOEMS,* vol. 10, no. 2, p. 023005, 2011.

[44] W. Zou, X. Qi and S. A. Burns, "Woofer-tweeter adaptive optics scanning laser ophthalmoscopic imaging based on Lagrange-multiplier damped least-squares algorithm," *Biomedical Optics Express,* vol. 2, no. 7, pp. 1986-2004, 2011.

[45] O. Keskin, P. Hampton, R. Conan, C. Bradley, A. Hilton and C. Blain, "Woofer-Tweeter Adaptive Optics Test Bench," in *NASA/ESA Conference on Adaptive Hardware and Systems,* Istanbul, 2006.

[46] A. J. Wright, D. Burns, B. A. Patterson, S. P. Poland, G. J. Valentine and J. M. Girkin, "Exploration of the Optimisation Algorithms used in the implementation of Adaptive Optics in Confocal and Multiphoton Microscopy," *Microscopy Research and Technique,* vol. 67, no. 1, pp. 36-44, 2005.

[47] X. Tao, B. Fernandez, O. Azucena, M. Fu, D. Garcia, Y. Zuo, D. C. Chen and a. J. Kubby, "Adaptive optics confocal microscopy using direct wavefront sensing," *Optics Letters,* vol. 36, no. 7, pp. 1062-1064, 2011.

[48] X. Tao, A. Norton, M. Kissel, O. Azucena and a. J. Kubby, "Adaptive optical two-photon microscopy using autofluorescent guide stars," *Optics Letters*, vol. 38, no. 23, pp. 5075-5078, 2013.

[49] L. .. Sherman, J. Y. .. Ye, O. .. Albert and T. B. .. Norris, "Adaptive correction of depth-induced aberrations in multiphoton scanning microscopy using a deformable mirror," *Journal of Microscopy*, vol. 206, no. 1, pp. 65-71, 2002.

[50] R. Fiolka, K. Si and M. Cui, "Complex wavefront corrections for deep tissue focusing using low coherence backscattered light," *Optics Express*, vol. 20, no. 15, pp. 16532-16543, 2012.

[51] C. A. Boccara, S. Gigan, M. Roth and J. Binding, "Optical Coherence Microscopy (OCM) and Full Field OCT (FFOCT) for Wavefront Correction in Dense Tissue," in *Biomedical Optics*, Miami, 2010.

[52] M. Pircher and R. Zawadzki, "Review of adaptive optics OCT (AO-OCT): principles and applications for retinal imaging," *Biomedical Optics Express* , vol. 8, no. 5, pp. 2536-2562, 2017.

[53] M. Saito, E. Yokoi and K. Kusaka, "Laser Scanning Microscope System". USA Patent US8576482, 5 December 2013.

[54] R. J. Noll, "Zernike polynomials and atmospheric turbulence," *Journal of the Optical Society of America*, vol. 66, no. 3, pp. 207-211, 1976.

[55] D. Ghiglia and M. Pritt, "Two-Dimensional Phase Unwrapping: Theory, Algorithms and Software," in *Phase Data, Quality Maps, Masks, and Filters*, New York, John Wiley & Sons, 1998, pp. 59-90.

[56] J. Tang, R. N. Germain and M. Cui, "Superpenetration optical microscopy by iterative multiphoton adaptive compensation technique," *Proceedings of the National Academy of Sciences (PNAS)*, vol. 109, no. 22, pp. 8434-8439, 2012.

[57] X. Tao, B. Fernadez, O. Azucena, M. Fu, D. Garcia, Y. Zuo, D. Chen and J. Kubby, "Adaptive optics confocal microscopy using direct wavefront sensing," *Optics Letter*, vol. 36, no. 7, pp. 1062-1064, 2011.

[58] P. Vermeulen, E. Muro, T. Pons, V. Loriette and A. Fragola, "Adaptive optics for fluorescence wide-field microscopy using spectrally independent guide star and markers," *Journal of Biomedical Optics*, vol. 16, no. 7, p. 076019, 2011.

[59] S. Rahman and M. Booth, "Direct wavefront sensing in adaptive optical microscopy using backscattered light," *Applied Optics*, vol. 52, no. 22, pp. 5523-5532, 2013.

[60] P. Artal, S. Navarro and D. Williams, "Odd Aberrations and double-pass measurements of retinal image quality," *J. Opt. Soc.AM.A,* vol. 12, no. 2, pp. 195-201, 1995.

[61] S. A. Rahman and M. J. Booth, "Direct wavefront sensing in adaptive optical microscopy using backscattered light," *Appl Opt,* vol. 52, no. 22, pp. 5523-5532, 2013.

[62] D. Debarre, E. Botcherby, T. Watanabe, S. Srinivas, M. Booth and T. Wilson, "Image-based adaptive optics for two-photon microscopy," *Opt Lett,* vol. 34, no. 16, pp. 2495-2497, 2009.

[63] J. Bueno, M. Skorsets, S. Bonora and P. Artal, "Wavefront correction in two-photon microscopy with a multi-actuator adaptive lens," *Opt Exp,* vol. 26, no. 11, pp. 14278-14287, 2018.

[64] M. Booth, "Wavefront Sensorless Adaptive Optics for Large Aberrations," *OPtics Letters,* vol. 32, no. 1, pp. 5-7, 2007.

[65] X. Zhu, P. Bedggood, B. Bui, C. Nguyen, Z. He and A. Metha, "Contrast-based sensorless adaptive optics for retinal imaging," *Optics Express,* vol. 6, no. 9, pp. 3577-3595, 2015.

[66] Y. Zhou, K. K. H. Chan, T. Lai and S. Tang, "Characterizing refractive index and thickness of biological tissues using combined multiphoton microscopy and optical coherence tomography," *Biomed Opt Express,* vol. 4, no. 1, pp. 38-50, 2013.

[67] S. P. Poland, A. J. Wright, S. Cobb, J. C. Vijverberg and J. M. Girkin, "A demonstration of the effectiveness of a single aberration correction per optical slice in beam scanned optically sectioning microscopes," *Micron,* vol. 42, no. 4, pp. 318-323, 2011.

APPENDICES

APPENDIX A

DETAILED DESIGN NOTES ON THE OPTICAL SYSTEM

Here I would like to thank Chris Arrasmith for his design work on the optical system, which I adopted and modified to this current version.

BMC DM to Revibro DM

Adoublet lens (f = 150mm) is used here to image the BMC DM onto the Revibro DM. The doublet lens is used as a 4f relay that the BMC DM is placed 2f in front of. And the Revibro DM locates at 2f behind the lens. As the active areas of BMC DMand Revibro DM are both 4mm in diameter, the single lens relay needs to produce a 1:1 magnification. Moreover, as the illumination is a collimated beam, this single lens relay will change it into a diverging beam onto the Revibro DM. As the membrane of the Revibro DM deflects, it will introduce wavefront curvature to collimate the diverging beam and further turn it into a converging beam. Zemax is used to set up the simulation and it is plotted in Figure 55.

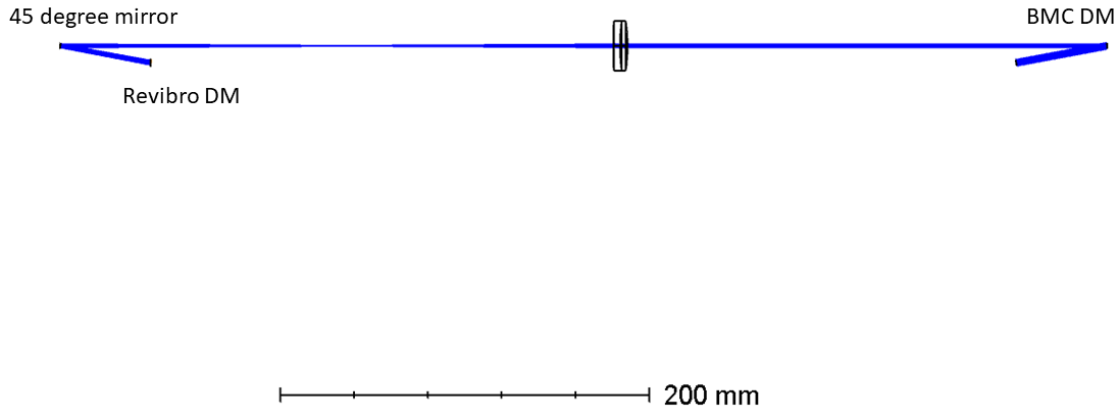

Figure 55. Zemax model for the optical path from BMC DM to Revibro DM.

With the “making conjugate” function , the actual optimized spacing is found to be 300mm from BMC DM to lens and 300mm from lens to Revibro DM. To make the

beam go through the mirrors with an angle as close to perpendicular to the Revibro, a 45 degree mirror is inserted 50mm before the Revibro DM. The lens data is listed as below.

Table 10. BMC DM to Revibro DM

Surface	Name	Radius	Thickness (mm)	Semi-diameter (mm)
0.00		Infinity	Infinity	0.00
1.00		Infinity	50.00	1.50
2.00	Coordinate break	Infinity	0.00	0.00
3.00	BMC	Infinity	0.00	1.50
4.00	Coordinate break	Infinity	-300.00	0.00
5.00	AC254-150-B-ML	-83.60	-4.00	12.70
6.00		89.33	-3.50	12.70
7.00		1330.50	0.00	12.70
8.00		Infinity	-250.00	1.45
9.00	Coordinate break	Infinity	0.00	0.00
10.00	45 degree mirror	Infinity	0.00	1.57
11.00	Coordinate break	Infinity	49.75	0.00
12.00	Coordinate break	Infinity	0.00	0.00
13.00	Revibro	Infinity	0.00	2.00
14.00	Coordinate break	Infinity	0.00	0.00
15.00		Infinity	0.00	2.06

The spot diagram indicates a diffraction limited performance as shown in Figure 56.

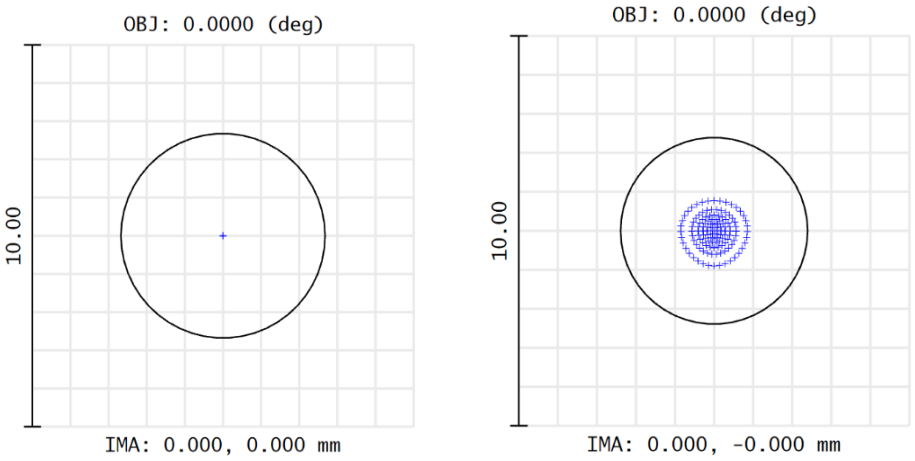

Figure 56. The Spot diagram for the relay. The full scale is 10 mrad. The focus spot is within the aberration free Airy disk for both case in which the Revibro DM is (left) flat and (right) at maximum deflection of 15µm. At maximum deflection, -120nm of astigmatism ($Z_{2,2}$) is introduced into the optical system.

Revibro DM to Y Galvo

A 4f relay that consists of two identical doublets (f = 100mm) is used to image the Revibro DM onto the Y Galvo.

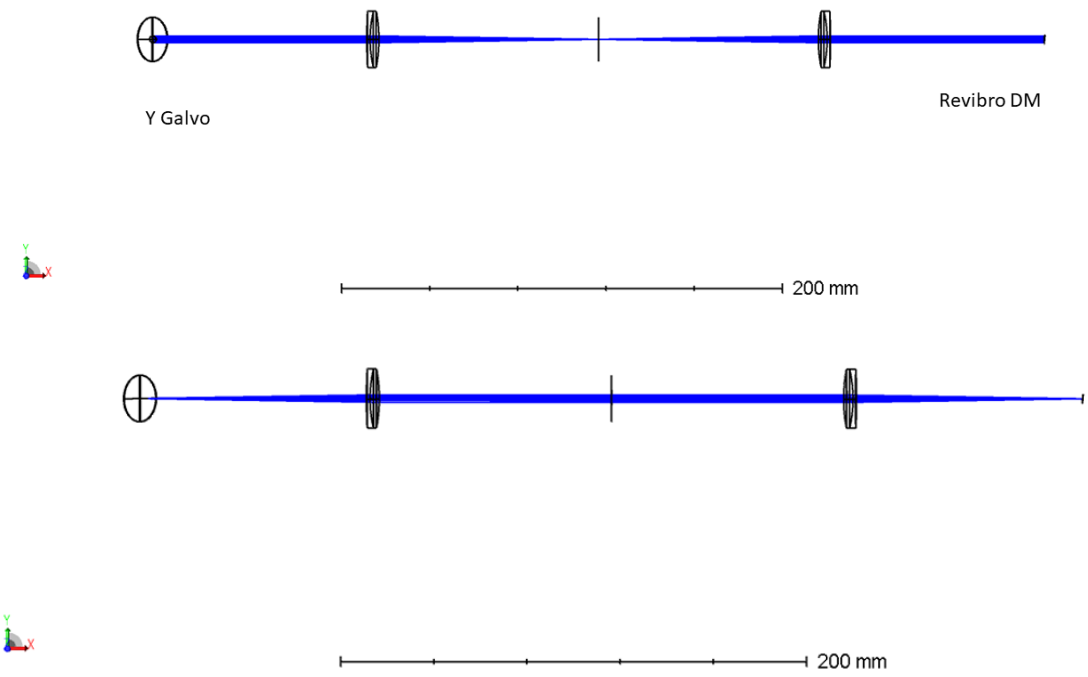

Figure 57. Zemax model for the 4f relay between the Revibro DM and the Y galvo scanner. (upper) Beam collimation. (lower) Imaging.

The 4f relay not only needs to be a good imager for the Revibro DM onto Y galvo but also should have good performance of collimating the beam. The simulation result is as shown in Figure 58.

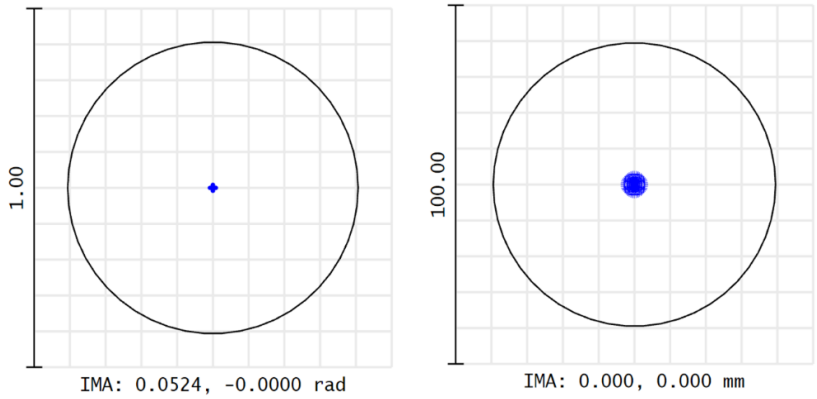

Figure 58. Spot diagram for the 4f relay between Revibro DM to Y galvo. (left) Performance as a beam collimator; (right) Performance as an imaging relay. The focus spot for both cases are much smaller than the size of the perfect Airy disk.

The lens data for the relay can be found in Table 11.

Table 11. Lens data for imaging Revibro DM onto Y galvo scanner

Surface	Name	Radius	Thickenss (mm)	Semi-diameter (mm)
0.00		Infinity	Infinity	0.00
1		Infinity	0.00	0.00
2	Revibro	Infinity	0.00	2.00
3		Infinity	0.00	0.00
4		Infinity	-97.09	1.50
5	AC254-100-B-ML	-259.41	-1.50	12.70
6	AC254-100-B-ML	-53.70	-4.00	12.70
7	AC254-100-B-ML	66.68	0.00	12.70
8		Infinity	-99.72	1.49
9		Infinity	-99.72	10.00
10	AC254-100-B-ML	-66.68	-4.00	12.70

11	AC254-100-B-ML	53.70	-1.50	12.70
12	AC254-100-B-ML	259.41	0.00	12.70
13		Infinity	-97.09	1.50
14		Infinity	0.00	0.00
15	Element Tilt	Infinity	0.00	0.00
16	Galvo 1	Infinity	0.00	10.00
17	Element Tilt:return	Infinity	0.00	0.00
18		Infinity	0.00	0.00
19		Infinity	0.00	0.00

Y galvo to X galvo

The two galvo scanners are the same in size. The magnification of the relay is set to 1:1. Moreover, the relay needs to accommodate a 9-degree optical field while maintaining diffraction limited performance. Therefore, we have chosen 2” lenses. The layout is plotted in Figure 59.

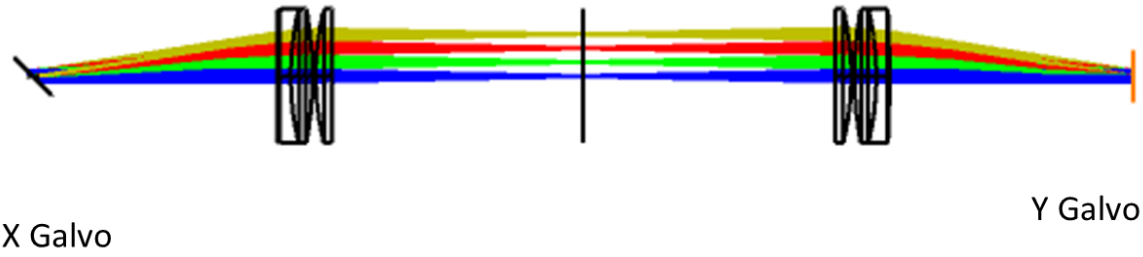

Figure 59. Zemax model for the 4f relay that images the Y galvo scanner onto the X galvo scanner

Each of the lens groups shown in Figure 59 consists of a 200mm achromat and a 200mm plano-convex lens. The combination yields aneffective focal length of 100mm.

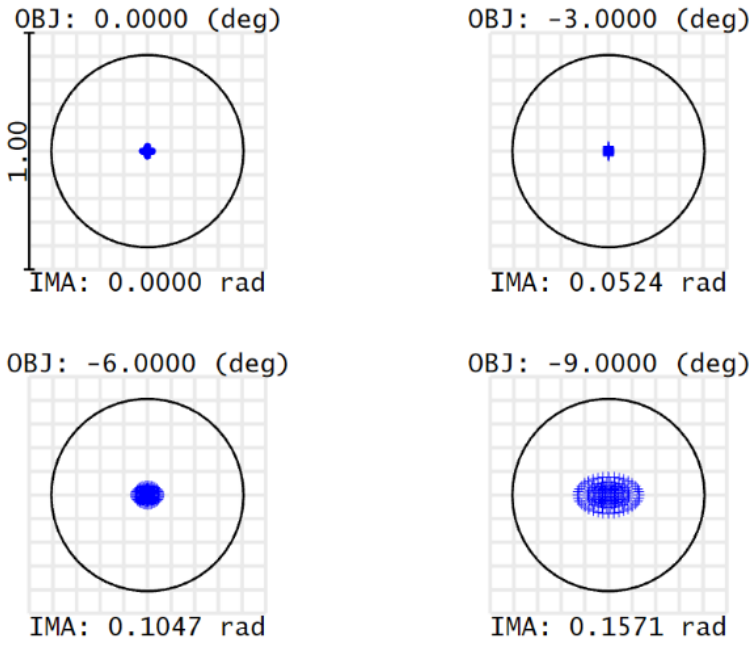

Figure 60. The spot diagram for the 4f relay between x and y galvo scanners at different scan angles.

The spot diagram shows a diffraction limited performance throughout the entire field of view. The lens data for the relay can be found in Table 12.

Table 12. Lens data for imaging Y galvo onto X galvo

Surface	Name	Radius	Thickenss (mm)	Semi-diameter (mm)
0.00		Infinity	Infinity	0.00
1.00		Infinity	92.45	10.00
2.00		515.20	5.00	25.40
3.00		109.20	8.20	25.40
4.00	AC508-200-B	-134.00	1.25	25.40
5.00	LA1979-B	103.01	6.18	25.40
6.00		Infinity	0.00	25.40
7.00		Infinity	96	25.40
8.00		Infinity	96	25.40

9.00		Infinity	6.18	25.40
10.00	LA1979-B	-103.01	1.25	25.40
11.00	AC508-200-B	134.00	8.20	25.40
12.00		-109.20	5.00	25.40
13.00		-515.20	0.00	25.40
14.00		Infinity	92.45	25.40
15.00		Infinity	0.00	0.00
16.00	Element Tilt	Infinity	0.00	0.00
17.00	Galvo 2	Infinity	0.00	10.00
18.00	Element Tilt:return	Infinity	0.00	0.00
19.00		Infinity	0.00	0.00
20.00		Infinity	0.00	1.79

X galvo to objective lens

The incident beam is 4mm in diameter on the x galvo scanner. The back aperture of the objective is 18mm in diameter. Therefore, we need to design a relay with a magnification of 4.5x. The Nikon tube lens has a focal length of 200mm, which indicates that a 200/4.5 = 44mm scan lens is needed. For the simulation, we used a Thorlabs achromat lens with a 200mm focal length as a representation of the Nikon tube lens. Moreover, the scan should be large enough to accommodate the 9-degree maximum optical angle. We have found the combination of a 2” 80mm achromat and a 2” 100mm plano-convex lens will provide the necessary focal length and accommodate the large scan angle.

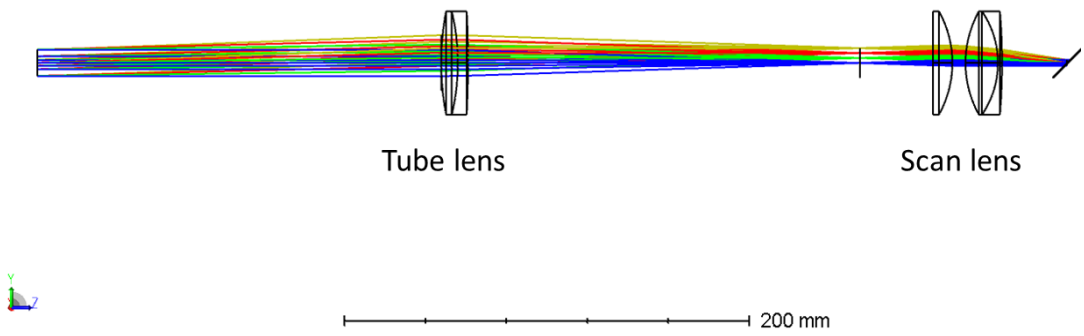

Figure 61. The relay consists of a scan lens and the tube lens in the Nikon microscope stand for imaging x galvo scanner onto the back focal plane of the objective lens.

The spot diagram shows that diffraction limited performance is achieved at all scan angles.

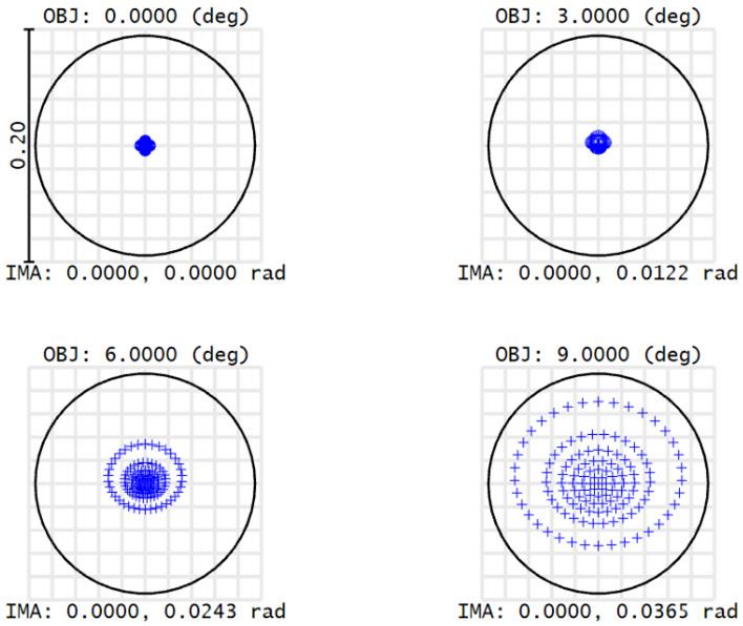

Figure 62. Spot diagram for the Scan lens and tube lens at different scan angles.

The lens data can be found in Table 13.Table 13. Lens data for the combination of scan lens and Nikon tube lens

Surface	Name	Radius	Thickenss (mm)	Semi-diameter (mm)
0		Infinity	Infinity	0.00
1		Infinity	0.00	0.00
2	Element Tilt	Infinity	0.00	0.00
3	Galvo 2	Infinity	0.00	10.00
4	Element Tilt:return	Infinity	0.00	0.00
5		Infinity	0.00	0.00
6		Infinity	-36.59	1.50
7		-312.60	-2.00	25.40
8		-44.60	-16.00	25.40
9	AC508-080-B	51.80	-6.51	25.40
10	LA1050-B	-51.50	-9.69	25.40
11		Infinity	-35.88	15.00
12	side port micro	Infinity	-193.78	7.31
13		-515.20	-5.00	25.40
14		-109.20	-8.20	25.40
15	AC508-200-B	134.00	0.00	25.40
16		Infinity	-199.55	10.61
17	Back surface of Objective	Infinity	0.00	9.51

Overall, the relay has a very desirable optical performance. The Strehl is plotted against the scan angle in Figure 63. The Strehl at maximum scan angle of 9-degree is 0.85, which indicates that the relay can maintain diffraction limited performance throughout the field of view.

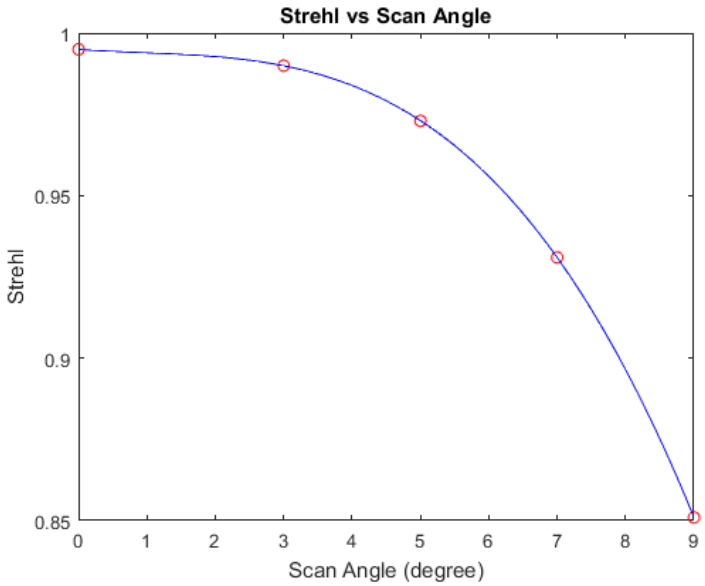

Figure 63. Strehl of the relay at different scan angle in x direction

APPENDIX B

THE CONSTRUCTED ACTIVE/ADATPIVE MICROSCOPE IN DETAIL

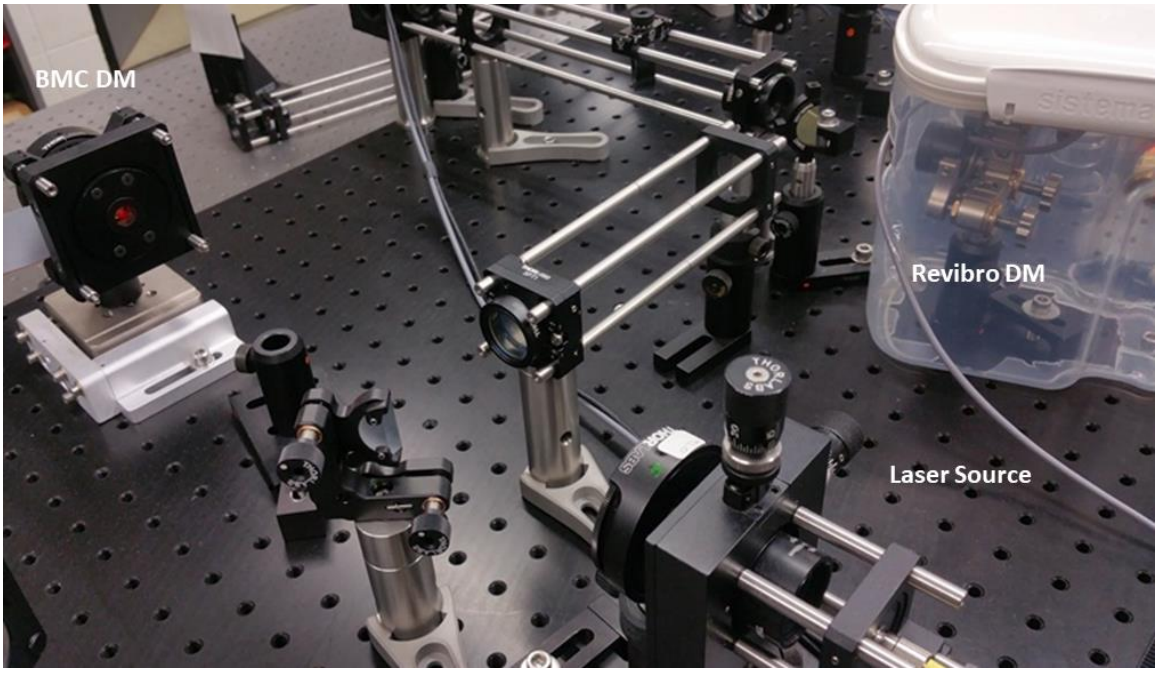

Figure 64. The laser source illuminates the BMC DM and imaged onto the Revibro DM through a single lens relay.

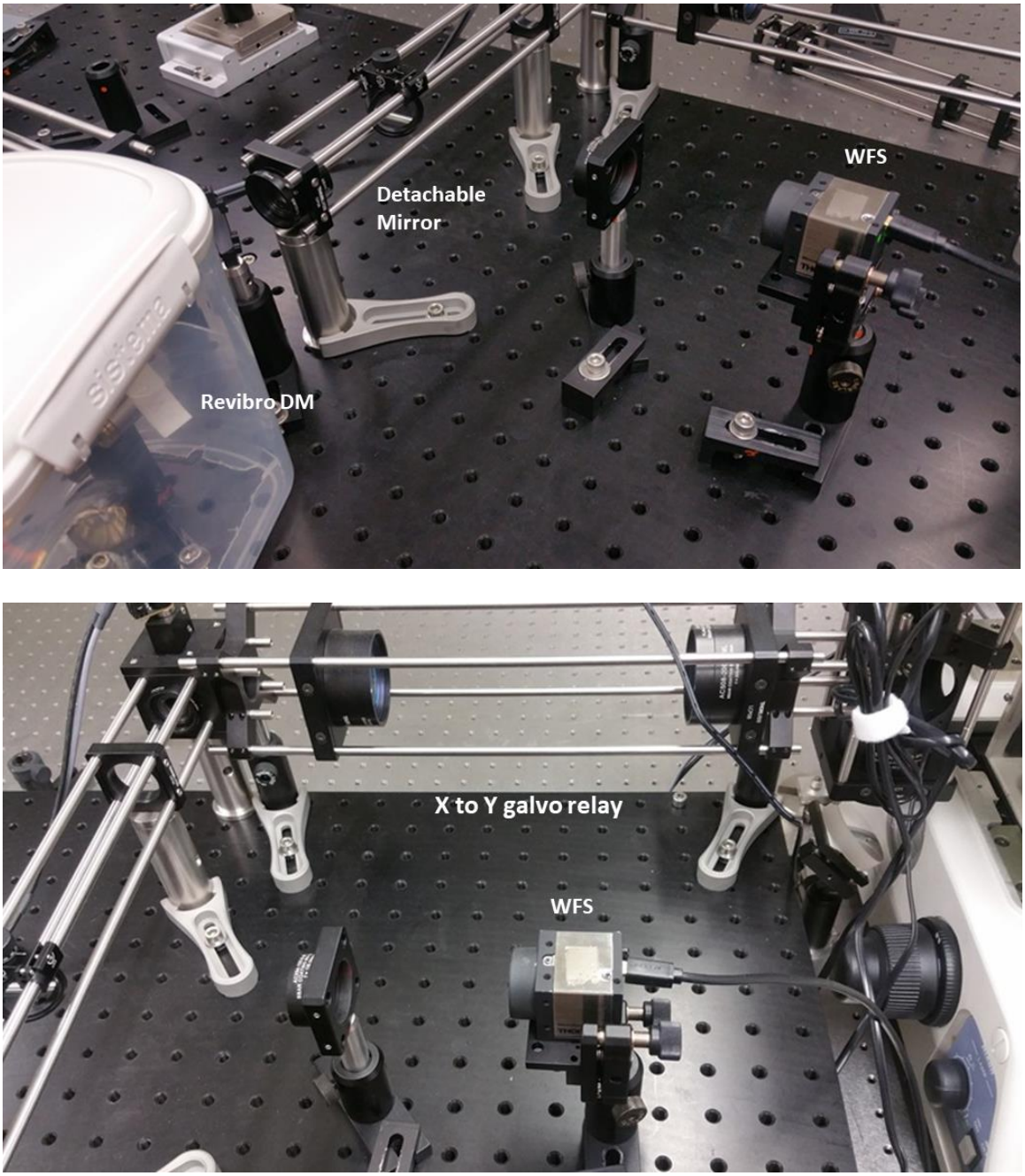

Figure 65. (Upper) Both Revibro DM and BMC DM are imaged onto the WFS through a 4f relay. A detachable mirror to steer to beam away from the imaging path onto the wavefront sensor during direct wavefront sensing. (Lower) X galvo scanner is imaged onto the Y galvo through a 2” 4f relay.

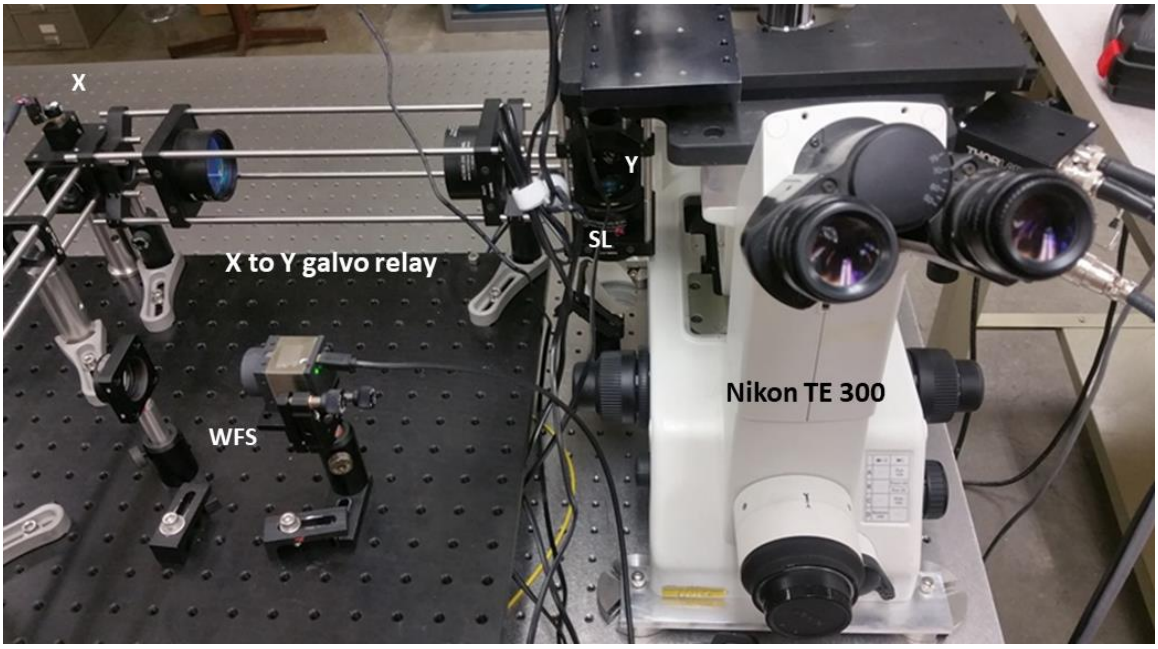

Figure 66. The Y gavlo is imaged onto the back focal plane of the objective through a relay that consists of the scan lens (SL) and a Nikon tube lens inside the Nikon TE 300 microscope stand. A 45-degree mirror is used to steer the incident beam into the side port of the microscope stand.

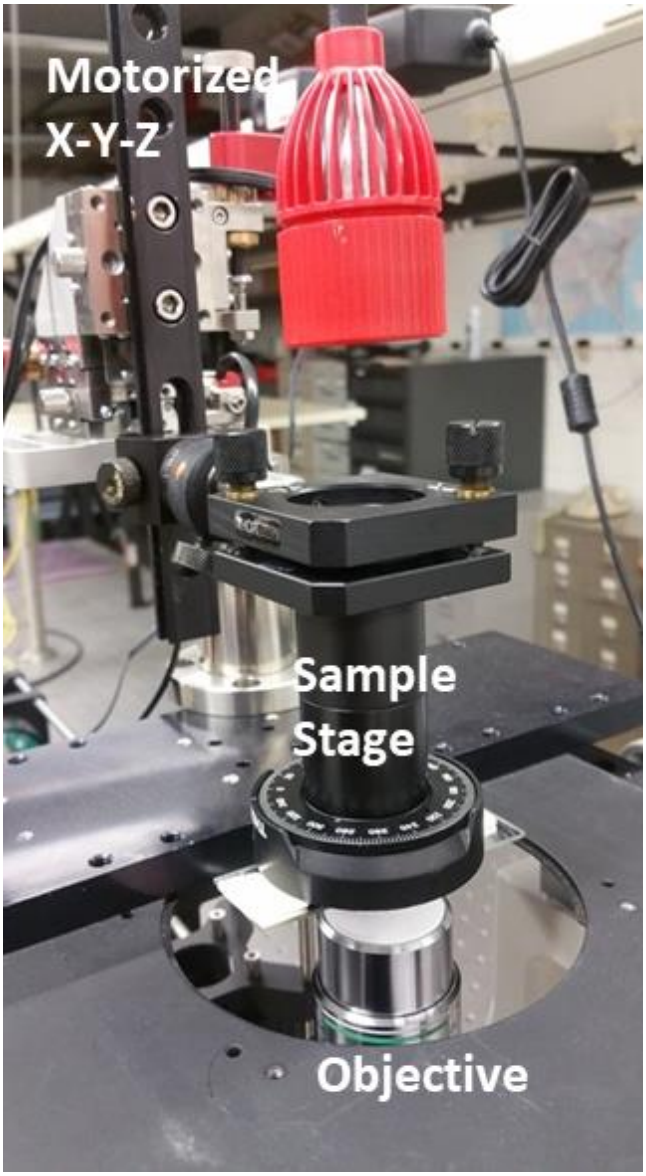

Figure 67. The sample stage mounted on a motorized x-y-z translation stage